TIME-DEPENDENT STUDIES OF FUNDAMENTAL

ATOMIC PROCESSES IN RYDBERG ATOMS

Except where reference is made to the work of others, the work described in this dissertation is my own or was done in collaboration with my advisory committee. This dissertation does not include proprietary or classified information.

_____

Türker Topçu

Certificate of Approval:

_____	_____
Michael S. Pindzola Professor Physics	Francis Robicheaux, Chair Professor Physics
_____	_____
Eugene Oks Professor Physics	Allen Landers Assoc. Professor Physics

_____

Joe F. Pittman
Interim Dean
Graduate School

TIME-DEPENDENT STUDIES OF FUNDAMENTAL ATOMIC PROCESSES IN RYDBERG ATOMS

Türker Topçu

A Dissertation

Submitted to

the Graduate Faculty of

Auburn University

in Partial Fulfillment of the

Requirements for the

Degree of

Doctor of Philosophy

Auburn, Alabama
4 August 2007

TIME-DEPENDENT STUDIES OF FUNDAMENTAL

ATOMIC PROCESSES IN RYDBERG ATOMS

Türker Topçu

_____

Signature of Author

_____

Date of Graduation

DISSERTATION ABSTRACT

TIME-DEPENDENT STUDIES OF FUNDAMENTAL ATOMIC PROCESSES IN RYDBERG ATOMS

Türker Topçu

Doctor of Philosophy, 4 August 2007
(M.Sc., Auburn University, 2005)

185 Typed Pages

Directed by Francis Robicheaux

This dissertation consists of four time-dependent studies of various fundamental atomic processes involving highly excited atoms and ions. We use time-dependent close-coupling theory besides other perturbative and and non-perturbative techniques, which has become standard in studying time-dependent atomic dynamics, to investigate these processes.

The atomic processes studied in the following chapters include photo-double ionization of He from ground and the first excites states, electron-impact ionization of highly excited hydrogen and hydrogen-like ions, radiative cascade from highly excited states of hydrogen in the presence of strong external magnetic fields, and chaotic ionization of a hydrogenic Rydberg wave packet in parallel electric and magnetic fields. Besides their obvious fundamental importance for advancing our understanding of the physics of highly excited atomic systems, all these problems have applications which are of practical and fundamental importance.

Throughout this work, we make an effort to carry out calculations that are inherently different from our quantum mechanical non-perturbative time-dependent calculations to benchmark and contrast our results with those that are either perturbative or classical. We make special effort to carry out classical calculations, where possible, to compare our quantum mechanical treatments with their classical counterparts for studying the classical-quantum correspondence for various different highly excited systems.

ACKNOWLEDGMENTS

I feel very much indebted and privileged to have worked with my Ph.D. advisor Prof. Francis Robicheaux, who has carefully guided my research. I would to thank my advisor for his sincere attention and help in guiding and supporting me through my research as a graduate student, while greatly enhancing my understanding of atomic physics, as well as physics in general. I must also acknowledge my gratitude to Prof. Francis Robicheaux for providing the data for the classical calculations presented in Chap. 4 and for providing the CTMC code that was used to generate classical results of Chap. 6.

I also would like to thank to rest of the members in my Ph.D. committee, namely, Prof. Michael S. Pindzola, Prof. Eugene Oks, and Assoc. Prof. Allen Landers for their time and suggestions during the preparation of this work. I must further thank Prof. Michael S. Pindzola for many elucidating and stimulating comments and discussions that helped me extend my understanding of atomic physics.

I am grateful to Assoc. Prof. Stuart D. Loch for helping me with various data visualization software and for conversations that have constituted the core of my understanding of the role of atomic processes in fusion plasmas.

I would like thank my family, who despite being abroad, kept their emotional support constant during my years away from home.

At last, I must thank the Office of Basic Energy Sciences and the Office of Fusion Energy Sciences, U.S. Department of Energy for their continued support for the research presented in this dissertation.

Style manual or journal used Transactions of the American Mathematical Society (together with the style known as "auphd"). Bibliograpy follows the style used by the American Physical Society.

Computer software used The document preparation package TEX (specifically LATEX) together with the departmental style-file `auphd.sty`.

TABLE OF CONTENTS

LIST OF FIGURES

CHAPTER 1

INTRODUCTION

In the last decade, the efforts made in studying highly excited atomic systems from both experimental and theoretical point of view has substantially escalated. Advancements made in cooling atoms down to only a few Kelvins made it possible to study atoms almost individually without having to suffer from the effects of collisions and thermalization. This has opened the possibility of studying highly excited atomic systems very efficiently from the experimental point of view, which otherwise has proven impossible due to the large dipole moments of these atomic systems.

Besides many immediate practical applications of Rydberg systems which we discuss below, study of highly excited systems is also very important from the standpoint of advancing our understanding of classical-quantum correspondence. Due to their large quantum numbers and high energies, Rydberg electrons in many cases can be treated classically in accordance with the Bohr correspondence principle. According to the most commonly adopted definition of the Bohr correspondence principle, any given quantum mechanical system in a bound state should converge to its classical counterpart in the case of large quantum numbers. Even though the Bohr correspondence principle is one of the cornerstones of the early quantum physics, systems have been found that violates it [1]. Therefore, study of fundamental atomic processes in Rydberg systems provides a very suitable arena for investigating and understanding the classical-quantum correspondence.

Apart from its obvious fundamental importance, atomic processes involving highly excited states also have important applications from modeling the plasma flow inside the fusion tokamaks to finding efficient ways to get the highly excited anti-hydrogen atoms to their ground states to study CPT violation in the universe. Below, we briefly discuss the importance and applications of the problems that are included in this dissertation.

1.1 Photo-double ionization of two electron atoms

One of the most fundamental problems in atomic physics is the three-body Coulomb breakup, which has long attracted the attention of both theorists and experimentalists. The importance of this problem arises mainly because of our inability in describing analytically the two escaping electrons resulting from absorption of a photon in the presence of a Coulombic core. The presence of the electron-electron interaction is vital for this process to take place, which also makes this problem fundamentally important in understanding the role of the electron correlations in the escape process. In this study, we particularly pay attention to the double ionization near threshold where both electrons move slowly and therefore can be approximately treated classically. Classical treatment of this problem resulted in threshold laws describing the energy dependence of the ionization cross section near threshold. We perform non-perturbative time-dependent calculations to investigate the threshold behaviors predicted by these classical threshold laws.

1.2 Electron-impact ionization from excited states

Electron-impact scattering from hydrogen-like ions is an important atomic process for modeling of tokamak plasmas and performing plasma diagnostics. Therefore, it is important to have ionization data accurate enough to satisfactorily model and diagnose laboratory plasmas. Usually, the cross sections for electron-impact ionization are obtained from fully quantal calculations for ionization from the lowest states and from classical calculations for ionization from highly excited states [2]. It has been shown [3] that for denser plasmas the effective ionization rate changes substantially when contributions through higher n levels are included in addition to the ground and metastable states. The sensitivity of the plasma models to the atomic data illustrates the need for the investigation of the extent to which the classical cross sections are accurate.

1.3 Radiative cascade in strong magnetic fields

Formation of highly excited anti-hydrogen atoms have been reported by two experimental groups where cold anti-protons are merged with a cold trapped positron plasma at roughly [4] 16 K and [5, 6] 4 K in magnetic fields of about 3 T and 5.4 T respectively. The goal is to perform Lorentz and CPT violation checks in the hyperfine spectrum of the $2s \rightarrow 1s$ transition [7] for which the transition frequency is accurately known to about 1 part in 10^{14} for atomic beam of hydrogen [8] and to about 1 part in 10^{12} for trapped hydrogen [9]. The dominant process in the formation of the anti-hydrogen atoms is believed to be three body recombination [10] which yields a small fraction of anti-hydrogen atoms

that are suitable for being laser stimulated down to the low-n states [11]. It has also been noted that the anti-hydrogen atoms formed through three body recombination are likely to be in highly excited m states [12]. Since Lorentz and CPT violation experiments require ground state anti-hydrogen atoms, the highly excited anti-hydrogen atoms need to decay down to the ground state in order to serve this purpose. The knowledge of the decay rates and the time it takes to cascade down to the ground state from initial distributions of Rydberg states with $|m| \sim n$ and from completely random ℓ, m distributions of Rydberg states in strong magnetic fields are therefore necessary.

1.4 Chaotic ionization of a highly excited hydrogen atom in external electric and magnetic fields

Rydberg atoms and wave packets have been particularly useful in studying how classically chaotic dynamics is manifested in their quantum mechanical counterparts. This is because Rydberg atoms provide a real non-separable physical system with just a few degrees of freedom whose classical counterpart exhibits chaos in external magnetic and combinations of magnetic and electric fields. Rydberg atoms in various combinations of static [13, 14, 15] fields have also been studied and several useful theoretical and computational tools have been developed during this process [16, 17]. In Chap. 6, we study ionization of a hydrogen atom excited to a Rydberg wave packet in external parallel electric and magnetic fields, whose classical counterpart have been shown to display chaos in the time domain. We investigate various time dependent properties of this system and successfully reproduce the classical results within a fully quantum mechanical framework.

The outline of this works is as follows. In Chap.2 we develop the general fundamental properties of the time-dependent methods we use throughout this work. We then turn our attention to the photo-double ionization of He from ground and singlet first excited state in Chap.3 to investigate the threshold law for double ionization. In Chap.4, we study electron-impact ionization of highly excited hydrogen and hydrogen-like ions as function of their principle quantum number and ion stage, and compare our non-perturbative results with those from classical trajectory Monte Carlo calculations to investigate the extent of which the Bohr correspondence principle holds. In Chap.5, we study radiative cascade of a highly excited hydrogen atom in a strong external uniform magnetic field and calculate the decay rates and lifetimes of its states in a fully quantum mechanical framework. Finally, in Chap.6, we delve into the chaotic dynamics of a hydrogenic Rydberg electron whose classical counterpart in time domain displays classical chaos. We calculate the ionization current from a hydrogenic Rydberg wave packet excited by a short laser pulse as a function of time in external uniform parallel electric and magnetic fields. We study the angular distributions of the electrons on a spherical detector through which we calculate the ionization current and investigate the angular momentum distribution of the ionizing electrons as a function of time. We further, study the onset of chaos as function of the scaled energy for different magnetic field strengths.

CHAPTER 2

NUMERICAL GRID METHODS FOR SOLVING THE TIME-DEPENDENT AND THE TIME-INDEPENDENT SCHRÖDINGER EQUATIONS FOR ATOMIC SYSTEMS

2.1 Introduction

In this chapter, I describe the general characteristics of the numerical methods that will be used in the following chapters. The numerical methods that are used in this dissertation mainly employs time-dependent grid techniques which require discretizing the space and time coordinates relevant to a given physical problem. Therefore, I will begin by describing the methodology used in discretizing space which enables us to study atomic systems on spatial lattices. Then, I will describe general characteristics of the time-dependent methods that are used in the following chapters for time propagating the time-dependent Schrödinger equation in one and two spatial dimensions. Finally, I will conclude by discussing the numerical methods used to generate the one- and two-electron orbitals by solving the time-independent Schrödinger equation. The discussions of this chapter are general in nature and the specifics of the theoretical and numerical methods that are employed for each of the problems in the following chapters are discussed in detail within each chapter. I will use atomic units in all of the following discussions where the mass and charge of an electron is taken to be unity and the unit of distance is a Bohr radius.

2.2 Grid techniques for the study of time-dependent atomic dynamics

Due to our inability to carry out exact analytical solutions to most of the problems we encounter in physics, many numerical methods have been invented for the study of complicated physical systems. With the advent of powerful computers that can carry out numerical simulations, this vast amount of numerical techniques gave rise to the birth of computational physics. Today's powerful computers open up the road to studying and understanding many physical systems which would otherwise be impossible to cope with. For our purposes, simulating an atomic system on a computer means storing and manipulating actual wave functions and orbitals that are defined in the continuous space-time. Since we cannot represent a continuous function on a computer, representing these functions requires discretization of space and time. Discretization of space leads to the concept of grid, or lattice, which is a set of points in space on which the wave functions and orbitals are calculated, stored and manipulated.

Since the orbitals and wave functions we represent on a lattice are actually continuous functions, it is important to define the lattice such that all the lattice spacings are smaller than the smallest distance scales involved in the problem in order to have a good representation of the physical system at hand. As an example, consider the momentum of a plane wave calculated on a uniform grid of points. Whereas the momentum of a one-dimensional

plane wave $e^{\mathrm{i}kr}$ is k, representing this plane wave on a grid gives,

$$\begin{aligned} pe^{\mathrm{i}kr} &= -\mathrm{i}\frac{e^{ik(r+\delta r)} - e^{ik(r-\delta r)}}{2\delta r} \\ &= -\frac{\mathrm{i}}{2\delta r}(e^{ik\delta r} - e^{-ik\delta r})e^{\mathrm{i}kr} \\ &= \frac{\sin(k\delta r)}{\delta r}e^{\mathrm{i}kr}. \end{aligned} \tag{2.1}$$

Note that as δr goes to zero, all the terms in the Taylor expansion of $\sin(k\delta r)/\delta r$ vanishes except the first, and $\sin(k\delta r)/\delta r$ converges to k as expected. As a result, the kinetic energy of the outgoing plane wave $e^{\mathrm{i}kr}$ on a uniform grid is

$$\begin{aligned} \frac{1}{2}p^2e^{\mathrm{i}kr} &= -\frac{1}{2}\frac{e^{ik(r+\delta r)} - 2e^{\mathrm{i}kr} + e^{ik(r-\delta r)}}{(\delta r)^2} \\ &= -\frac{1}{2(\delta r)^2}(e^{ik\delta r} - 2 + e^{-ik\delta r})e^{\mathrm{i}kr} \\ &= \frac{1-\cos(k\delta r)}{(\delta r)^2}e^{\mathrm{i}kr}. \end{aligned} \tag{2.2}$$

This means the plane wave $e^{\mathrm{i}kr}$ with momentum k becomes a *plane wave* with kinetic energy $(1-\cos(k\delta r))/(\delta r)^2$ on a uniform grid of points. Again, note that as $\delta r \to 0$, eigenvalue of the kinetic energy operator in Eq. 2.2 converges to $k^2/2$ as expected.

To make sure that we have accurate lattice representations of the atomic systems we are studying in the following chapters, we take special care for performing convergence checks to make sure that the lattices we use are fine enough such that our results have numerical errors of only a few percent due to the discrete nature of our spatial lattices.

When using grid techniques, another important issue arises due to the finite nature of the space enclosed within the boundaries of the grid, which we refer to as a *box*. The problem of defining a large enough box with minimum number of points is important since fewer points means less computational burden, which in turn translates into the ability to study a wider array of problems. Although the uniform meshes are the most natural choices, most of the time they are not the most optimum ones, meaning that they do not provide the largest box for a given number of grid points. Specifically, in problems involving Rydberg atoms, large boxes are required since the size of the atom in a high-n state scales as $\sim 2n^2$. For such problems, we have found that using a non-linear mesh, particularly a square-root mesh, is more suitable for the lattice representations of Rydberg systems.

2.2.1 Square-root Mesh

To be able to study atomic problems involving excited states, many types of non-linear lattices have been employed in time-dependent studies of atomic systems [46]. Particularly, square-root lattices have proved especially fruitful for the study of Rydberg systems due to the fact that at large distances, a square-root mesh puts roughly the same number of points in nodes of the highly excited atomic orbitals. Here, I will first describe the general idea behind the institution of a one-dimensional non-linear lattice for the description of a wave packet $\psi(r)$, which then I will specify for a square-root mesh.

Expectation value of the kinetic energy operator T on a one-dimensional non-uniform mesh can be given by,

$$\begin{aligned}
\langle T \rangle &= \frac{1}{2} \int \psi^* \left(-\mathrm{i} \frac{d}{dr} \right) \left(-\mathrm{i} \frac{d}{dr} \right) \psi \, dr \\
&= \frac{1}{2} \int \left(\frac{d\psi^*}{dr} \right) \left(\frac{d\psi}{dr} \right) dr \\
&\simeq \frac{1}{2} \sum_{j=0}^{N} (\psi'_{j+1/2})^* (\psi'_{j+1/2}) (r_{j+1} - r_j) \\
&\simeq \frac{1}{2} \sum_{j=0}^{N} \frac{(\psi_{j+1} - \psi_j)^* (\psi_{j+1} - \psi_j)}{(r_{j+1} - r_j)} \\
&\simeq \frac{1}{2} \sum_{j=0}^{N} \frac{|\psi_{j+1} - \psi_j|^2}{(r_{j+1} - r_j)}
\end{aligned} \tag{2.3}$$

where prime denotes derivative with respect to r, and we have employed the midpoint rule for the derivative. The time-dependent Schrödinger equation in terms of the kinetic energy and the potential energy operators can be written as,

$$\mathrm{i} \dot{\psi} = T\psi + V\psi \tag{2.4}$$

where dot denotes the derivative with respect to time, and T and V are the kinetic and the potential energy operators, respectively. Multiplying this equation with ψ^* from left and integrating over r on the lattice yields,

$$\frac{\mathrm{i}}{2} \sum_{j}^{N} \psi_j^* \dot{\psi}_j (r_{j+1} - r_{j-1}) = \langle T \rangle + \frac{1}{2} \sum_{j}^{N} \psi_j^* V_j \psi_j (r_{j+1} - r_{j-1}). \tag{2.5}$$

Taking the derivative of both sides of Eq. 2.5 with respect to ψ_j^* and multiplying through by two, the Schrödinger equation on the lattice becomes,

$$\mathrm{i}\dot{\psi}_j(r_{j+1} - r_{j-1}) = 2\frac{\partial\langle T\rangle}{\partial\psi_j^*} + V_j\psi_j(r_{j+1} - r_{j-1}) \tag{2.6}$$

where we have dropped the summation over the grid points to reduce the equation to a particular lattice site j. From the kinetic energy expression in Eq. 2.3, we can evaluate the derivative of $\langle T\rangle$ with respect to ψ^* as

$$\frac{\partial\langle T\rangle}{\partial\psi_j^*} = -\frac{1}{2}\left[\frac{\psi_{j+1} - \psi_j}{r_{j+1} - r_j} - \frac{\psi_j - \psi_{j-1}}{r_j - r_{j-1}}\right] \tag{2.7}$$

and with the use of this expression, the time-dependent Schrödinger equation in 2.6 at lattice site j becomes,

$$\mathrm{i}(r_{j+1} - r_{j-1})\dot{\psi}_j = -\left[\frac{\psi_{j+1} - \psi_j}{r_{j+1} - r_j} - \frac{\psi_j - \psi_{j-1}}{r_j - r_{j-1}}\right] + V_j(r_{j+1} - r_{j-1})\psi_j. \tag{2.8}$$

With the change of variables $\psi_j = z_j/\sqrt{(r_{j+1} - r_{j-1})/2}$, this equation can be further written as,

$$\begin{aligned}\mathrm{i}\dot{z}_j = &- \frac{z_{j-1}}{\sqrt{(r_{j+1} - r_{j-1})(r_j - r_{j-2})}(r_j - r_{j-1})} \\ &+ \left[\frac{1}{(r_{j+1} - r_j)(r_j - r_{j-1})} + V_j\right] z_j \\ &- \frac{z_{j+1}}{\sqrt{(r_{j+2} - r_j)(r_{j+1} - r_{j-1})}(r_{j+1} - r_j)}.\end{aligned} \tag{2.9}$$

In terms of the new variable z, the normalization integral reduces to a simple sum,

$$\sum_j |\psi_j|^2 (r_{j+1} - r_{j-1}) = \sum_j |z_j|^2 = 1 \tag{2.10}$$

Eq. 2.9 can now be written in the matrix form,

$$\mathrm{i}\dot{\vec{z}} = \mathbb{T}\vec{z} + \mathbb{V}\vec{z} \tag{2.11}$$

where the kinetic energy matrix $\mathbb{T}$ is tridiagonal and the potential energy matrix $\mathbb{V}$ is diagonal in r.

Note that this derivation holds for any non-linear spatial lattice and gives a squre-root mesh when $r_j = r_{\mathrm{f}}\, j^2/N^2$.

2.3 Methods for time-propagation of the time-dependent Schrödinger Equation

In this section, we describe the methods used to simulate the time evolution of the radial part of a wave function according to the time-dependent Schrödinger equation. First we discuss the simpler explicit time-propagation scheme and then describe the implicit propagator for one-dimensional atomic systems. For higher dimensional systems, we discuss the split-operator scheme which in combination with one of the one-dimensional propagation schemes yields a propagator for radial part of the wave function involving two or more electrons.

2.3.1 Explicit Scheme

Since the time-dependent Schrödinger equation is a partial differential equation involving both time and space variables, obtaining a particular solution requires an initial condition, i.e. the initial wave function, which we take to be $\psi(-\delta t)$ where δt is the time step taken during the propagation and we assume a uniform mesh in time. Using the Taylor expansion of the exact quantum mechanical time evolution operator $e^{-\mathrm{i}H\delta t}$, propagating $\psi(0)$ one time step backward in time gives,

$$\psi(-\delta t) = \left(1 + \mathrm{i}H\delta t - \frac{1}{2}H^2\delta t^2 + \mathcal{O}[\delta t^3]\right)\psi(0) \tag{2.12}$$

where we have expanded the exact quantum mechanical time evolution operator $e^{-\mathrm{i}H\delta t}$ up to terms of the order δt^2. Applying the time evolution operator a second time to $\psi(0)$ gives the wave function at $t = \delta t$,

$$\psi(\delta t) = \left(1 - \mathrm{i}H\delta t - \frac{1}{2}H^2\delta t^2 + \mathcal{O}[\delta t^3]\right)\psi(0). \tag{2.13}$$

Subtracting Eq. 2.12 from Eq. 2.13, and keeping terms up to order δt^2, yields the lowest order leap-frog scheme,

$$\psi(\delta t) = \psi(-\delta t) - 2\mathrm{i}\delta t H\psi(0) \tag{2.14}$$

The terms of the order δt^3 and up being ignored, the error in this method scales as δt^3. Due to omitted terms in the Taylor expansion of the time evolution operator and the discretization of the space, two main types of errors emerge: the phase and the amplitude errors.

To estimate the phase error, it is useful to decompose $\psi(t)$ as

$$\psi(t) = \sum_j A_j \exp(-\mathrm{i}\bar{\epsilon}_j t)\phi_j \tag{2.15}$$

where ϕ_j are the eigenstates of the time-independent Hamiltonian H with eigenvalues $\bar{\epsilon}_j$ on the grid. Note that the eigenvalues $\bar{\epsilon}_j$ are just the actual eigenvalues ϵ_j of the Hamiltonian H with the phase accumulation. Substituting Eq. 2.15 into Eq. 2.14 and recalling that $e^{-i\alpha} = \cos(\alpha) - \mathrm{i}\sin(\alpha)$, we get

$$\sum_j A_j \exp(-\mathrm{i}\bar{\epsilon}_j \delta t)\phi_j = \sum_j A_j \exp(\mathrm{i}\bar{\epsilon}_j \delta t)\phi_j - 2\mathrm{i}\delta t H \sum_j A_j \phi_j \tag{2.16}$$

$$-2\mathrm{i}\sum_j A_j \sin(\bar{\epsilon}_j \delta t)\phi_j = -2\mathrm{i}\delta t \sum_j A_j \bar{\epsilon}_j \phi_j. \tag{2.17}$$

Multiplying both sides of this equation with ϕ_k and integrating over all coordinates, and recalling the orthonormality of the eigenstates, i.e.,

$$\langle \phi_j | \phi_k \rangle = \delta_{j,k}, \tag{2.18}$$

one can realize that

$$\epsilon_j \delta t = \sin(\bar{\epsilon}_j \delta t). \tag{2.19}$$

Provided that $\max(|\epsilon_j|)\delta t \leq 1$ this relation between ϵ_j and $\bar{\epsilon}_j$ can be inverted to give

$$\bar{\epsilon}_j = \frac{1}{\delta t} \arcsin(\epsilon_j \delta t). \tag{2.20}$$

From Eq. 2.20 it is clear that the explicit scheme is not necessarily unitary unlike the actual time evolution operator. If $\epsilon_j \delta t > 1$, then the right hand side of Eq. 2.20 would be complex, which would give a time dependent norm. Using Eq. 2.15 and Eq. 2.20, we can show that the lowest order leap-frog propagator is exactly unitary when $\max(|\epsilon_j|)\delta t \leq 1$. To see this, we need to evaluate $|\psi(\delta t)|^2$ and show that it has the same norm as $\psi(-\delta t)$.

$$\begin{aligned} |\psi(\delta t)|^2 &= |\psi(-\delta t)|^2 - 2\mathrm{i}H\delta t\psi^*(0)\psi(-\delta t) + 2\mathrm{i}H\delta t\psi^*(-\delta t)\psi(0) \\ &\quad -(2\mathrm{i}H\delta t)^2|\psi(0)|^2 \end{aligned} \tag{2.21}$$

Decomposing ψ as in Eq. 2.15

$$\begin{aligned} |\psi(\delta t)|^2 &= |\psi(-\delta t)|^2 - 2\mathrm{i}H\delta t\psi^*(0)\psi(-\delta t) + 2\mathrm{i}H\delta t\psi^*(-\delta t)\psi(0) \\ &\quad -(2\mathrm{i}H\delta t)^2\psi^*(0)\psi(0) \\ &= |\psi(-\delta t)|^2 - 2\mathrm{i}\delta t \sum_{j,k} A_j^* A_k \epsilon_j \exp(\mathrm{i}\bar{\epsilon}_k \delta t)\phi_j^*\phi_k \\ &\quad +2\mathrm{i}\delta t \sum_{k,j} A_k^* A_j \epsilon_k \exp(-\mathrm{i}\bar{\epsilon}_k \delta t)\phi_k^*\phi_j - (2\mathrm{i}\delta t)^2 \sum_{j,k} \epsilon_j^2 A_j^* \phi_j^* A_k \phi_k. \end{aligned} \tag{2.22}$$

To evaluate the norm of $\psi(t)$, we integrate both sides of Eq. 2.22 over all coordinates

$$\begin{aligned}
\int |\psi(\delta t)|^2 d^3\vec{r} &= 1 - 2\mathrm{i}\delta t \sum_{j,k} A_j^* A_k \epsilon_j \exp(\mathrm{i}\bar{\epsilon}_k \delta t) \int \phi_j^* \phi_k d^3\vec{r} \\
&\quad + 2\mathrm{i}\delta t \sum_{k,j} A_k^* A_j \epsilon_k \exp(-\mathrm{i}\bar{\epsilon}_k \delta t) \int \phi_k^* \phi_j d^3\vec{r} \\
&\quad - (2\mathrm{i}\delta t)^2 \sum_{j,k} \epsilon_j^2 A_j^* A_k \int \phi_j^* \phi_k d^3\vec{r} \\
&= 1 - 2\mathrm{i}\delta t \sum_j |A_j|^2 \epsilon_j \exp(\mathrm{i}\bar{\epsilon}_j \delta t) \\
&\quad + 2\mathrm{i}\delta t \sum_j |A_j|^2 \epsilon_j \exp(-\mathrm{i}\bar{\epsilon}_j \delta t) \\
&\quad - (2\mathrm{i}\delta t)^2 \sum_j \epsilon_j^2 |A_j|^2. \qquad (2.23)
\end{aligned}$$

where we have used the orthonormality condition 2.18 of the eigenstates ϕ_j, and taken $\psi(-\delta t)$ to be normalized to unity. Combining second and third terms in Eq. 2.23

$$\begin{aligned}
\int |\psi(\delta t)|^2 d^3\vec{r} &= 1 - 2\mathrm{i}\delta t \sum_j |A_j|^2 \epsilon_j [\exp(\mathrm{i}\bar{\epsilon}_j \delta t) - \exp(-\mathrm{i}\bar{\epsilon}_j \delta t)] \\
&\quad - (2\mathrm{i}\delta t)^2 \sum_j \epsilon_j^2 |A_j|^2 \\
&= 1 - 2\mathrm{i}\delta t \sum_j |A_j|^2 \epsilon_j 2\mathrm{i} \sin(\bar{\epsilon}_j \delta t) - (2\mathrm{i}\delta t)^2 \sum_j \epsilon_j^2 |A_j|^2. \qquad (2.24)
\end{aligned}$$

Recalling Eq. 2.19, this results in

$$\begin{aligned}
\int |\psi(\delta t)|^2 d^3\vec{r} &= 1 - (2\mathrm{i}\delta t)^2 \sum_j |A_j|^2 \epsilon_j^2 - (2\mathrm{i}\delta t)^2 \sum_j |A_j|^2 \epsilon_j^2 \\
&= 1. \qquad (2.25)
\end{aligned}$$

Note that the step taken in getting from Eq. 2.24 to Eq. 2.25 requires that the condition $\max(|\epsilon_j|)\delta t \leq 1$ is satisfied. This imposes the condition $\max(|\epsilon_j|)\delta t \leq 1$ for unitarity of the explicit scheme.

Keeping terms up to order δt^5 in the Taylor expansions of the exponential time evolution operator in Eqs. 2.12 and 2.13, we obtain the next order leap-frog scheme,

$$\psi(\delta t) = \psi(-\delta t) - 2\left(\mathrm{i}H\delta t - \frac{iH^3\delta t^3}{3!}\right)\psi(0) \tag{2.26}$$

where now the error scales like δt^5. Repeating the same procedure as we have carried out above to estimate the phase errors, one obtains,

$$\sin(\bar{\epsilon}_j\delta t) = \epsilon_j\delta t - \frac{\epsilon_j^3\delta t^3}{3!} \tag{2.27}$$

which can be inverted to give

$$\bar{\epsilon}_j = \frac{1}{\delta t}\arcsin\left(\epsilon_j\delta t - \frac{\epsilon_j^3\delta t^3}{3!}\right) \tag{2.28}$$

provided that

$$\left|\epsilon_j\delta t - \frac{\epsilon_j^3\delta t^3}{3!}\right| \leq 1. \tag{2.29}$$

This inequality can be solved for $\epsilon_j\delta t$ to yield the condition for unitarity to be $\max(|\epsilon_j|)\delta t \lesssim 2.8$.

2.3.2 Implicit Scheme

Instead of using the Taylor expansion of the exponential time evolution operator as we did in deriving the explicit scheme, we can simply integrate the time-dependent Schrödinger equation

$$\mathrm{i}\dot{\psi} = H\ \psi \tag{2.30}$$

over one time step δt,

$$\mathrm{i}\int_0^{\delta t} \dot{\psi} dt = \int_0^{\delta t} H\ \psi dt. \tag{2.31}$$

Using the trapezoidal rule for the right hand side, this can be approximated as

$$\mathrm{i}[\psi(\delta t) - \psi(0)] \simeq H\frac{\delta t}{2}[\psi(\delta t) + \psi(0)]. \tag{2.32}$$

Rearranging and solving for $\psi(\delta t)$ yields,

$$\psi(\delta t) \simeq \left(\frac{1 - \mathrm{i}H\delta t/2}{1 + \mathrm{i}H\delta t/2}\right)\psi(0). \tag{2.33}$$

The operator in front of $\psi(0)$ is the lowest order Padé approximation for the exact time evolution operator to order δt^3.

$$e^{-\mathrm{i}H\delta t} = \left(\frac{1 - \mathrm{i}H\delta t/2}{1 + \mathrm{i}H\delta t/2}\right) + \mathcal{O}[\delta t^3] \tag{2.34}$$

We refer this approximation to the exact time evolution operator as the implicit propagator. In contrast to the explicit operator, the Padé approximation to the quantum mechanical

time-evolution operator is exactly unitary regardless of the size of the time step δt. This can easily be seen by checking the usual unitarity condition as follows,

$$\begin{aligned}\left(\frac{1-\mathrm{i}H\delta t/2}{1+\mathrm{i}H\delta t/2}\right)^{\dagger}\left(\frac{1-\mathrm{i}H\delta t/2}{1+\mathrm{i}H\delta t/2}\right) &= \left(\frac{1+\mathrm{i}H^{\dagger}\delta t/2}{1-\mathrm{i}H^{\dagger}\delta t/2}\right)\left(\frac{1-\mathrm{i}H\delta t/2}{1+\mathrm{i}H\delta t/2}\right) \\ &= \left(\frac{1+\mathrm{i}H\delta t/2}{1-\mathrm{i}H\delta t/2}\right)\left(\frac{1-\mathrm{i}H\delta t/2}{1+\mathrm{i}H\delta t/2}\right) \\ &= 1. \end{aligned} \tag{2.35}$$

Here we have used the fact that the Hamiltonian is hermitian, i.e. $H^{\dagger} = H$.

Even though it is unconditionally unitary, due to the discretization of the space on the lattice, the implicit propagator still suffers from the phase errors. To estimate the phase errors over a time step, we will substitute the decomposed wave function 2.15 into the implicit propagator,

$$\begin{aligned}\psi(t+\delta t) &= \left(\frac{1-\mathrm{i}H\delta t/2}{1+\mathrm{i}H\delta t/2}\right)\sum_j A_j e^{-\mathrm{i}\bar{\epsilon}_j t}\phi_j \\ \psi(t+\delta t) &= \sum_j A_j e^{-\mathrm{i}\bar{\epsilon}_j t}\left(\frac{1-\mathrm{i}\epsilon_j\delta t/2}{1+\mathrm{i}\epsilon_j\delta t/2}\right)\phi_j \\ \psi(t+\delta t) &= \sum_j A_j e^{-\mathrm{i}\bar{\epsilon}_j t}e^{-\mathrm{i}(\epsilon_j t+\varphi)}\phi_j \end{aligned} \tag{2.36}$$

where we have noted that $H\psi_j = \epsilon_j\psi_j$ and φ is the phase error, and we have used

$$\frac{1-\mathrm{i}\epsilon_j\delta t/2}{1+\mathrm{i}\epsilon_j\delta t/2} = e^{-\mathrm{i}(\epsilon_j\delta t+\varphi)}. \tag{2.37}$$

This can be manipulated to give

$$\left(\frac{2}{1+(\epsilon_j\delta t/2)^2}-1\right)-\mathrm{i}\frac{\epsilon_j\delta t}{1+(\epsilon_j\delta t/2)^2}=\cos(\epsilon_j\delta t+\varphi)-\mathrm{i}\sin(\epsilon_j\delta t+\varphi). \tag{2.38}$$

which implies

$$\begin{aligned}\cos(\epsilon_j\delta t+\varphi) &= \frac{2}{1+(\epsilon_j\delta t/2)^2}-1\\ \sin(\epsilon_j\delta t+\varphi) &= \frac{\epsilon_j\delta t}{1+(\epsilon_j\delta t/2)^2}.\end{aligned} \tag{2.39}$$

From Eq. 2.39 the phase error φ can be deduced to be

$$\varphi=\arccos\left(\frac{2}{1+(\epsilon_j\delta t/2)^2}-1\right)-\epsilon_j\delta t \tag{2.40}$$

or, equivalently,

$$\varphi=\arcsin\left(\frac{\epsilon_j\delta t}{1+(\epsilon_j\delta t/2)^2}\right)-\epsilon_j\delta t \tag{2.41}$$

2.3.3 Split-Operator Technique

In our discussions of the explicit and implicit methods above, we have assumed a one-dimensional Hamiltonian. In cases where there is more than one electron or dimension involved, we can split the total Hamiltonian into pieces where at least one piece involves only a single dimension. For example, in the case of the two-electron model Hamiltonian

of Chapter 4, we have divided the Hamiltonian as

$$H(r_1, r_2) = H_1(r_1) + H_2(r_2) + H_3(r_1, r_2) \tag{2.42}$$

where

$$\begin{aligned} H_1(r_1) &= -\frac{1}{2}\frac{\partial^2}{\partial r_1^2} - \frac{Z}{r_1} \\ H_2(r_2) &= -\frac{1}{2}\frac{\partial^2}{\partial r_2^2} - \frac{Z}{r_2} \\ H_3(r_1, r_2) &= \frac{1}{r_1 + r_2} \end{aligned} \tag{2.43}$$

for which the split operator looks like,

$$e^{-\mathrm{i}H\delta t} \simeq e^{-\mathrm{i}H_3\delta t/2} e^{-\mathrm{i}H_1\delta t} e^{-\mathrm{i}H_2\delta t} e^{-\mathrm{i}H_3\delta t/2}. \tag{2.44}$$

For brevity, we will discuss the case where the total Hamiltonian is split into two pieces, i.e. $H = H_1 + H_2$, for which the split operator technique is the lowest order split operator technique,

$$\psi(t + \delta t) \simeq e^{-\mathrm{i}H_1\delta t/2} e^{-\mathrm{i}H_2\delta t} e^{-\mathrm{i}H_1\delta t/2} \psi(t). \tag{2.45}$$

Note that the expression 2.45 is exactly unitary when H_1 and H_2 commute. When the commutator $[H_1, H_2]$ does not vanish, the error can be shown to be $(\mathrm{i}/24)[H_1 + 2H_2, [H_1, H_2]]\delta t^3$

by Taylor expanding both sides of

$$e^{-\mathrm{i}H\delta t} \simeq e^{-\mathrm{i}H_1\delta t/2} e^{-\mathrm{i}H_2\delta t} e^{-\mathrm{i}H_1\delta t/2}. \tag{2.46}$$

It can be shown that the propagator 2.45 is exactly unitary for hermitian H_1 and H_2. To show this, we need to calculate

$$\bar{\psi}(t) = [e^{-\mathrm{i}H_1\delta t/2} e^{-\mathrm{i}H_2\delta t} e^{-\mathrm{i}H_1\delta t/2}]^\dagger [e^{-\mathrm{i}H_1\delta t/2} e^{-\mathrm{i}H_2\delta t} e^{-\mathrm{i}H_1\delta t/2}]\psi(t) \tag{2.47}$$

and show that $\bar{\psi}(t)$ identically yields $\psi(t)$, i.e. the operator in front of $\psi(t)$ is identity. Noting that $[e^{-\mathrm{i}H\delta t}]^\dagger = [e^{\mathrm{i}H^\dagger\delta t}]$ and $(AB)^\dagger = B^\dagger A^\dagger$, we can rewrite this expression as

$$\begin{aligned} \bar{\psi}(t) &= [e^{\mathrm{i}H_1^\dagger\delta t/2}(e^{-\mathrm{i}H_1\delta t/2} e^{-\mathrm{i}H_2\delta t})^\dagger][e^{-\mathrm{i}H_1\delta t/2} e^{-\mathrm{i}H_2\delta t} e^{-\mathrm{i}H_1\delta t/2}]\psi(t) \\ &= [e^{\mathrm{i}H_1^\dagger\delta t/2} e^{\mathrm{i}H_2^\dagger\delta t} e^{\mathrm{i}H_1^\dagger\delta t/2}][e^{-\mathrm{i}H_1\delta t/2} e^{-\mathrm{i}H_2\delta t} e^{-\mathrm{i}H_1\delta t/2}]\psi(t). \end{aligned} \tag{2.48}$$

For hermitian H_1 and H_2, $H_1^\dagger = H_1$ and $H_2^\dagger = H_2$, and therefore we can regroup as follows,

$$\begin{aligned} \bar{\psi}(t) &= e^{\mathrm{i}H_1\delta t/2} e^{\mathrm{i}H_2\delta t} \underbrace{e^{\mathrm{i}H_1\delta t/2} e^{-\mathrm{i}H_1\delta t/2}}_{\mathbb{I}} e^{-\mathrm{i}H_2\delta t} e^{-\mathrm{i}H_1\delta t/2}\psi(t) \\ &= e^{\mathrm{i}H_1\delta t/2} \underbrace{e^{\mathrm{i}H_2\delta t} e^{-\mathrm{i}H_2\delta t}}_{\mathbb{I}} e^{-\mathrm{i}H_1\delta t/2}\psi(t) \\ &= \underbrace{e^{\mathrm{i}H_1\delta t/2} e^{-\mathrm{i}H_1\delta t/2}}_{\mathbb{I}}\psi(t) \\ &= \psi(t) \end{aligned} \tag{2.49}$$

which is what we wanted to show.

2.4 Time-dependent perturbation theory

When the interaction term in the total Hamiltonian is small such that the atom stays mostly in the initial state it started out with, the time-dependent perturbation theory can be used and directly incorporated into the time-dependent Schrödinger equation:

$$\left(\mathrm{i}\frac{\partial}{\partial t} - H\right)\Psi(\vec{r},t) = 0. \tag{2.50}$$

Splitting the total Hamiltonian into the perturbed and unperturbed parts, i.e. $H = H_0 + H'(t)$, Eq. 2.50 can be rewritten as

$$\left(\mathrm{i}\frac{\partial}{\partial t} - H_0\right)\Psi(\vec{r},t) = H'(t)\Psi(\vec{r},t). \tag{2.51}$$

Since the Schrödinger equation is linear, we seek the solution to Eq. 2.51 as,

$$\Psi(\vec{r},t) = \psi^{(0)}(\vec{r})e^{-\mathrm{i}E_0 t} + \psi^{(1)}(\vec{r},t) \tag{2.52}$$

where $\psi^{(0)}$ is the eigenstate of the unperturbed Hamiltonian H_0 with the energy E_0. Note that the entire time-dependence of the unperturbed solution in the first term on the right hand side of Eq. 2.51 is in the complex exponential form and the effect of the perturbation term in the equation is *linearly* reflected to the solution through $\psi^{(1)}$. Substituting this

solution into Eq. 2.51,

$$\left(\mathrm{i}\frac{\partial}{\partial t} - H_0\right)\psi^{(1)}(\vec{r},t) = H'(t)\psi^{(0)}(\vec{r})e^{-\mathrm{i}E_0 t} + H'(t)\psi^{(1)}(\vec{r},t). \tag{2.53}$$

Ignoring the second term on the right hand side gives the time-dependent Schrödinger equation consistent with the first order time-dependent perturbation theory. Feeding the solution of this equation back into itself gives higher order perturbation theory.

$$\begin{aligned}
\left(\mathrm{i}\frac{\partial}{\partial t} - H_0\right)\psi^{(1)}(\vec{r},t) &= H'(t)\psi^{(0)}(\vec{r})e^{-\mathrm{i}E_0 t} && \text{1st order} \\
\left(\mathrm{i}\frac{\partial}{\partial t} - H_0\right)\psi^{(2)}(\vec{r},t) &= H'(t)\psi^{(1)}(\vec{r},t) && \text{2nd order} \\
\left(\mathrm{i}\frac{\partial}{\partial t} - H_0\right)\psi^{(3)}(\vec{r},t) &= H'(t)\psi^{(2)}(\vec{r},t) && \text{3rd order} \\
&\vdots
\end{aligned} \tag{2.54}$$

The total solution Ψ would be

$$\Psi(\vec{r},t) = \psi^{(0)}(\vec{r})e^{-\mathrm{i}E_0 t} + \psi^{(1)}(\vec{r},t) + \psi^{(2)}(\vec{r},t) + \psi^{(3)}(\vec{r},t) + \ldots. \tag{2.55}$$

2.5 Green's Function Method

Note that all of the equations in Eq. 2.54 are of the form

$$\left(\mathrm{i}\frac{\partial}{\partial t} - H_0\right)\psi^{(1)}(\vec{r},t) = S(\vec{r},t) \tag{2.56}$$

which is an inhomogeniuous partial differential equation. There are mainly two reasons for using this method to solve for $\psi^{(1)}$ directly, instead of solving for the total wave function. First, in the cases where perturbation theory is applicable, $\psi^{(1)}$ is usually much smaller than $\psi^{(0)}$, making it hard to extract the information carried in $\psi^{(1)}$ from the total wave function. The second advantage has to do with the time scales involved in the Schrödinger equation. Even though H' and $\psi^{(0)}e^{-\mathrm{i}E_0 t}$ may vary rapidly with time, their product usually varies much slower with time, which enables us to use larger time steps for the time propagation of the Schrödinger equation.

Integrating Eq. 2.56 equation through one time step δt, we get

$$\mathrm{i}\int_t^{t+\delta t}\frac{\partial\psi^{(1)}(\vec{r},t')}{\delta t'} = H_0\int_t^{t+\delta t}\psi^{(1)}(\vec{r},t')\delta t' + \int_t^{t+\delta t}S(\vec{r},t')\delta t'. \tag{2.57}$$

If we use the trapezoidal rule to evaluate this integral, we obtain

$$\psi(\vec{r},t+\delta t) = \left(\frac{1-\mathrm{i}H_0\delta t/2}{1+\mathrm{i}H_0\delta t/2}\right)\psi^{(1)}(\vec{r},t) - \frac{\mathrm{i}\delta t}{1+\mathrm{i}H_0\delta t/2}S\left(\vec{r},t+\frac{\delta t}{2}\right) + \mathcal{O}[\delta t^3] \tag{2.58}$$

Note that at $t=0$ $\psi(\vec{r},t=0) = \psi^{(0)}(\vec{r},t=0)$ therefore initially $\psi^{(1)}=0$. The operator in the first term on the right hand side is the lowest order Padé approximation to the exponential time evolution operator,

$$e^{-\mathrm{i}H_0\delta t} = \left(\frac{1-\mathrm{i}H_0\delta t/2}{1+\mathrm{i}H_0\delta t/2}\right) + \mathcal{O}[\delta t^3]. \tag{2.59}$$

Therefore we can rewrite Eq. 2.58 as,

$$\psi^{(1)}(\vec{r}, t+\delta t) = e^{-\mathrm{i}H_0\delta t}\ \psi^{(1)}(\vec{r}, t) - \frac{\mathrm{i}\delta t}{1+\mathrm{i}H_0\delta t/2} S\left(\vec{r}, t+\frac{\delta t}{2}\right) + \mathcal{O}[\delta t^3]. \qquad (2.60)$$

For example, if we take the total Hamiltonian to be the two-electron Hamiltonian of Chapter 3 with the electron-electron interaction being $V(r_1, r_2) = 1/(r_1 + r_2)$, we can evaluate the effect of the exponential time evolution operator onto $\psi^{(1)}(\vec{r}, t)$ using lowest order split operator technique with implicit propagator,

$$\begin{aligned}\psi(\vec{r}, t+\delta t) &= e^{-\mathrm{i}V\delta t/2}\left(\frac{1-\mathrm{i}H_1\delta t/2}{1+\mathrm{i}H_1\delta t/2}\right)\left(\frac{1-\mathrm{i}H_2\delta t/2}{1+\mathrm{i}H_2\delta t/2}\right) e^{-\mathrm{i}V\delta t/2}\ \psi^{(1)}(\vec{r}, t) \\ &\quad - \left(\mathrm{i}\delta t + \frac{\delta t^2}{2}H_0\right) S\left(\vec{r}, t+\frac{\delta t}{2}\right) + \mathcal{O}[\delta t^3]. \qquad (2.61)\end{aligned}$$

where $H_0 = H_1 + H_2$ and $H_j = p_j^2/2 - Z/r_j$ with $(j = 1, 2)$. Instead of evaluating the integral 2.57 using the trapezoidal rule, if we change the integral limits to range from $t-\delta t$ to $t + \delta t$ and use the midpoint rule, we reach the lowest order leap frog scheme for solving Eq. 2.56.

$$\begin{aligned}\psi^{(1)}(\vec{r}, t+\delta t) = \psi^{(1)}(\vec{r}, t-\delta t) &- 2\mathrm{i}H_0\delta t\psi^{(1)}(\vec{r}, t+\delta t) \\ &-2\mathrm{i}\delta t S(\vec{r}, t) + \mathcal{O}[\delta t^3]. \qquad (2.62)\end{aligned}$$

2.6 Time-independent methods for generating the one- and two-electron orbitals

As the wave function of an atomic system is propagated through time, the atomic eigenstates are projected onto the total wave function to extract information about excitation and ionization from the atomic system. For the problems that we will discuss, this means generating and storing the one-electron orbitals beforehand to project them onto the time-dependent wave function as it evolves through time. In the next two subsections, we discuss two methods which we have found to be efficient in generating the atomic orbitals.

2.6.1 The Shooting Method

The Shooting method is simply integrating the Schrödinger equation from both ends of the box in which the orbitals need to be generated. To integrate the time-independent Schrödinger equation, we first discretize the Schrödinger equation, $H\psi = E\psi$,

$$-\frac{1}{2}\frac{\psi_{j-1} - 2\psi_j + \psi_{j+1}}{(\delta r)^2} + V_j\psi_j = E\psi_j. \tag{2.63}$$

where we used a uniform grid for brevity. To start the forward integration, we need two points on the grid, i.e. ψ_0 and ψ_1 which we take to be zero and δr respectively. Solving for ψ_{j+1} we get

$$\psi_{j+1} = 2(\delta r)^2(E - V_j)\psi_j + 2\psi_j - \psi_{j-1}. \tag{2.64}$$

When the classical turning point is reached, the time-dependent Schrödinger equation turns from parabolic to elliptic in nature and the numerical integration picks up the diverging solution. At this point, one stops the forward integration and start to integrate the Schrödinger equation backwards from the box edge. Taking $\psi_N = 0$ and $\psi_{N-1} = \delta r$, we can solve for ψ_{j-1},

$$\psi_{j-1} = 2(\delta r)^2(E - V_j)\psi_j + 2\psi_j - \psi_{j+1}. \tag{2.65}$$

One then stops at the point at which the forward integration was terminated and matches the results of the forward and backward integrations at this point to obtain a smooth orbital.

2.6.2 The Relaxation Methods

Another effective method for generating the atomic orbitals involves the iterative application of $(E_{\text{max}} - H)$ or $1/(E_g - H)$ operator onto a chosen trial function. Here E_{max} is the maximum energy that can be supported by the grid, i.e. $2/(\delta r)^2$, and E_g is a guess for ground state energy of the Hamiltonian H. The choice of the trial function is not vital for the success of the method, although it effects the number of iterations needed to converge to the desired eigenstate. The closer the trial function to the actual eigenstate less iterations it takes to converge.

The effect of the operators $(E_{\text{max}} - H)$ and $1/(E_g - H)$ onto a trial function can be understood if one considers the trial function a superposition of the actual eigenstates of the Hamiltonian H. When either of the operators $(E_{\text{max}} - H)$ or $1/(E_g - H)$ is applied to the trial function, its action is to rescale the mixing coefficients of the eigenstates of H in the expansion such that the coefficient of the lowest energy eigenstate gains a higher boost

relative to the coefficients of the higher energy eigenstates in the expansion. Repeating this process with the energy guess E updated at every iteration, one checks the convergence of the expectation values

$$\begin{aligned} \delta_E^{(\alpha)} &= \langle \phi_{n,\ell}^{(\alpha)} | (H - E_{n,\ell}) | \phi_{n,\ell}^{(\alpha)} \rangle \\ \delta_{E^2}^{(\alpha)} &= \langle \phi_{n,\ell}^{(\alpha)} | (H^2 - E_{n,\ell}^2) | \phi_{n,\ell}^{(\alpha)} \rangle \end{aligned} \tag{2.66}$$

every time step, where $\phi_{n,\ell}^{(\alpha)}$ is the initial trial function after α iterations. The iteration is stopped when δ_E and δ_{E^2} get below a chosen tolerance. Just as the trial function, the closer the initial guess $E^{(0)}$ to the actual energy of the ground state less iterations it takes to converge. Note that since neither of the operators $(E_{\text{max}} - H)$ or $1/(E_g - H)$ is unitary, the iterated function must be normalized after each time step.

Also note that the relaxation method cannot be used to generate an excited eigenstate without first generating all the eigenstates that energetically lie below it. Once the ground state is generated, the same trial function can then be used to generate the next eigenstate by the same iterative process with subtracting the ground state generated previously. Since the iteration always converges to the lowest energy component in the trial function, this would force the iteration to converge to the eigenstate with the second lowest eigenenergy. This process can be used to generate the spectrum of the Hamiltonian H one by one from ground state up to a desired excited state. This makes this method most useful when one needs all of the eigenstates and eigenenergies of the Hamiltonian from ground state up to an excited eigenstate.

CHAPTER 3

THE PHOTO-DOUBLE IONIZATION CROSS SECTION OF HELIUM NEAR THRESHOLD IN A COLLINEAR s-WAVE MODEL

3.1 Introduction

In this chapter, we investigate the threshold laws for double ionization by studying the photo-double ionization of a helium atom from its ground and the first excited state $1s2s(^1S)$. The photo-double ionization problem near the threshold region presents a formidable challenge from a theoretical point of view since both of the electrons move slowly in the threshold region, and interact for a long time before they escape into the continuum. Various theories developed for studying the two electron escape process near threshold to explain the energy sharing of the escaping electrons, energy dependence of the double ionization cross section, and the angular distributions of the outgoing electrons. Due to the fact that both electrons move slowly near the threshold, this problem has been treated on purely classical grounds and two conceptually different theories have been developed to describe the energy dependence of the photo-double ionization cross section near the threshold.

First of these models, the Wannier theory [44], assumes that both of the electrons travel along the Wannier ridge and have the same kinetic energy. They leave the atom along the opposite sides of the atom and have approximately the same distance from the nucleus. Wannier theory predicts the excess energy dependence of the photo-double ionization cross

section as $\sigma_{2e} \sim E_{exc}^{\alpha}$ where E_{exc} is the excess energy and α is the Wannier exponent which equals 1.056. Following this classical picture of the Wannier theory, both semiclassical [20] and quantum mechanical [21] treatments of the threshold law have been carried out and confirmed the Wannier law.

The second classical theory developed to describe the energy dependence of the double ionization cross section near the threshold is the Coulomb-dipole theory developed by Temkin and Hahn [53]. Contrary to the Wannier theory, Coulomb-dipole theory predicts the double ionization cross section to be monotonically increasing while modulated by oscillations. This model does not assume that the electrons leave the atom with equal kinetic energies, but rather one of the electrons leave the atom faster than the other. The faster electron experiences a dipole potential formed by the residual ion and the slower leaving electron.

To decide which of the models describe the actual double-ionization process near threshold better, several experiments have been performed to test these threshold laws. An experiment by Kossmann *et al* [23] has investigated the validity of the Wannier law for the photo-double ionization of He along with its range of validity. They have found very good agreement with the Wannier law and observed no oscillations modulating the threshold law. On the other hand, more recent experiments by Wehlitz *et al* [24] and Lukič *et al* [25] displayed oscillations beyond experimental uncertainty in the photo-double ionization cross sections of Li and Be, respectively.

In this chapter, we present results of our calculations for the photo-double ionization of He from the ground and the first excited states within 1.0 eV excess energy above the

threshold. We perform our calculations in a collinear s-wave model which assumes that both electrons are positioned on the opposite sides of the atom and that the electron-electron interaction potential is $1/(r_1+r_2)$ where r_1 and r_2 are the radial coordinates of the electrons. In the past, this model potential has been used to study two-electron dynamics and shown to include the essential physics of the electron-electron interaction in the Coulomb field [53, 41]. Using a model potential for the electron-electron interaction enabled us to extend our calculations up to the first excited state which has proven challenging for the full three-dimensional calculations. A full three-dimensional calculation investigating the Wannier threshold law for the ground state He within 1.0 eV above threshold has been performed by Kleiman *et al* [27] and agrees perfectly with our findings. Most of the work presented in this chapter has been published as part of a letter in the Journal of Physics B [27].

3.2 Theory

Because the three-dimensional calculation of the photoionization of helium near threshold is computationally difficult, we examined a simpler model with lower dimensionality. We calculated the photo-double ionization probability in the collinear model, where the interaction potential between the electrons is represented by $1/(r_1 + r_2)$. The choice of this potential stems from the fact that the collinear potential yields the correct threshold law for the two electron escape process, $\sigma \sim E^{1.056}$. On the other hand the the cross section obtained from the exact s-wave potential exhibits an exponential supression due to the cusp it has on the Wannier ridge $r_1 = r_2$ (Ref. [28]). On the other hand, this model potential has been used successfully in the past to study two-electron dynamics and shown

to include the essential physics in the electron-electron interaction [53, 41]. These facts combined with the computational burden of a three-dimensional calculation have incited us to use the collinear s-wave model as a good test case for investigating the oscillations in the photo-double ionization cross section.

With the choice of the collinear potential, the two electron Hamiltonian can be written as

$$\hat{H}_0 = \sum_{\alpha=1}^{2} \left(\frac{\hat{p}_\alpha^2}{2} - \frac{2}{r_\alpha} \right) + \frac{1}{r_1 + r_2}. \tag{3.1}$$

As described in Chap. 2.5, for the time dependent wave function of the two electron system we made the ansatz $\psi(r_1, r_2, t) = \psi^{(0)}(r_1, r_2, t) + \psi^{(1)}(r_1, r_2, t)$, where $\psi^{(0)}(r_1, r_2, t) = \varphi_0(r_1, r_2)e^{-\mathrm{i}E_0 t}$ and E_0 is the energy of the state φ_0 according to $\hat{H}_0\varphi_0 = E_0\varphi_0$. We investigated the threshold photo-double ionization of helium out of both $1s^2(^1S)$ and $1s2s(^1S)$ states which were generated on a radial box by relaxation of a trial function on the grid, as described in Chap. 2.6. Generation of the one-electron orbitals $\varphi_0^{1s^2}$ and φ_0^{1s2s} on the box introduces continuum character into the eigenstates which is crucial for the double ionization of the model atom.

The time-dependent Schrödinger equation that is first order in photon interaction can be written as

$$\begin{aligned} \left(i\frac{\partial}{\partial t} - \hat{H}_0 \right) \psi^{(1)}(r_1, r_2, t) &= F(t)e^{-i(\omega+E_0)t}(r_1 + r_2)\psi^{(0)}(r_1, r_2) \\ &= S(r_1, r_2, t) \end{aligned} \tag{3.2}$$

where ω is the energy of the incoming photon in atomic units, $F(t)$ is the time dependence of the laser pulse, and E_0 is the energy of the initial state $\psi^{(0)}(r_1, r_2)$. The right hand side of Eq. 3.2 is the source term $S(r_1, r_2, t)$ due to the laser field. Time dependence $F(t)$ of the electric field in the source term $S(r_1, r_2, t)$ was chosen to be

$$F(t) = \begin{cases} \frac{1}{2}\Big[1 - \cos\Big(\frac{2\pi}{t_{\text{cut}}}t\Big)\Big] & \text{for } 0 < t < t_{\text{cut}}, \\ 0 & \text{for } t > t_{\text{cut}} \end{cases} \tag{3.3}$$

where t_{cut} is the pulse duration, which we have taken to be half the total propagation time. We have solved Eq. 3.2 as outlined in Chap. 2.5 using the lowest order leap-frog scheme:

$$\begin{aligned} \psi^{(1)}(r_1, r_2, t + \delta t) &= \psi^{(1)}(r_1, r_2, t - \delta t) - 2i\hat{H}_0 \delta t \psi^{(1)}(r_1, r_2, t) \\ &\quad -2i\delta t S(r_1, r_2, t) + \mathcal{O}[\delta t^3]. \end{aligned} \tag{3.4}$$

Since there is no analytical expression for the helium atom wave functions, $\psi^{(1)}(r_1, r_2, t)$ is placed in a radial box that extends to a finite r_f. The finite size of the box imposes an upper limit on the total propagation time because the fast ionizing components of the wave function reflected at the end of the box would eventually rescatter from the remaining core. On the other hand, longer propagation time is desired because it means that we can leave the source term on for a longer period of time so that the photon is represented by a well defined sharp peak in the energy space. Therefore, to increase the total propagation time we put an absorption mask at the end of the box to absorb the fast, high energy components of the wave function.

Note that the Wannier law $E^{1.056}$ assumes an energy distribution with zero width and goes to zero as $E \rightarrow 0$. Since we have have an energy distribution with finite width in the energy space due to the fact that our pulse is on for a finite amount of time, we needed to compare our results with the threshold law convolved with our energy distribution. We convolved the Wannier law with the squared absolute value of the Fourier transformation of $F(t)$,

$$\langle E^{1.056} \rangle (E_{exc}) = \frac{\int |\mathcal{F}(E - E_{exc}^{1.056})|^2 E^{1.056} dE}{\int |\mathcal{F}(E - E_{exc}^{1.056})|^2 dE} \tag{3.5}$$

where we have denoted the Fourier transform of $F(t)$ by $\mathcal{F}$, and fit this convolved threshold law to our results for comparison. Note that $\langle E^{1.056} \rangle (E_{exc})$ is just the expectation value of $E_{exc}^{1.056}$ with respect to the energy distribution corresponding to our time-dependent pulse $F(t)$.

All the projections needed to obtain the photo-double ionization probabilities are done after the source term is turned off. The probability for finding both of the electrons in the continuum is calculated by

$$\begin{aligned} P_{2e}(t) &= \int\int |\psi^{(1)}(r_1, r_2, t)|^2 dr_1 dr_2 - 2 \sum_n \left| \int \psi^{(1)}(r_1, r_2, t) \phi_{ns}(r_1) dr_1 \right|^2 \\ &\quad + \sum_n \sum_m \left| \int\int \psi^{(1)}(r_1, r_2, t) \phi_{ns}(r_1) \phi_{ms}(r_2) dr_1 dr_2 \right|^2 . \end{aligned} \tag{3.6}$$

Here $\phi_{ns}(r)$s are the He^+ negative energy eigenstates, i.e. $(\hat{p}^2/2 - 2/r)\phi_{ns}(r) = \tilde{\epsilon}_{ns}\phi_{ns}(r)$. These eigenstates are computed in a radial box that extends out twice as far as the box used for the time propagation of $\psi^{(1)}(r_1, r_2, t)$ for increased accuracy in the projections. Also,

generation of He^+ states in a finite box yields a finite number of bound and continuum eigenstates. Therefore, to minimize the error due to the finite box size we carefully chose the box size so that the threshold is straddled between the highest energy bound state and the lowest energy continuum state on the box.

3.3 Calculations and Results

To check the convergence of our results we have performed a series of calculations where we have varied our box size, mesh spacing, time step and the total propagation time independently for each energy value of the incoming photon. We have scaled our double ionization probabilities with t_{peak} which is half of the pulse duration t_{cut}. Figs. 3.1 and 3.2 show the Wannier convolved scaled probabilities for photo-double ionization out of He($1s^2(^1S)$) and He($1s2s(^1S)$) as a function of the excess energy for three different lattice spacings and pulse durations. In all of these calculations, the box size r_{f} was kept fixed at 200 (a.u.) and the time steps taken for the time propagation were $\delta t = 0.01$ (a.u.). Note that for the lattice spacings of 0.1 (a.u.) and 0.07 (a.u.), i.e. for the 2000 and 3000 point lattices, the convolved scaled double ionization probabilities are in excellent agreement, whereas the double ionization probability calculated for $\delta r = 0.2$ (a.u.) is somewhat deviated from the other two. We have also performed other convergence checks where only the lattice spacing was varied with a much longer pulse duration than those presented in Figs. 3.1 and 3.2, and found that we could increase δr up to 0.3 and still get results that are converged within a few percent. Therefore, we conclude that the differences between the solid and the other curves in Figs. 3.1 and 3.2 are mainly due to the differences in the pulse durations

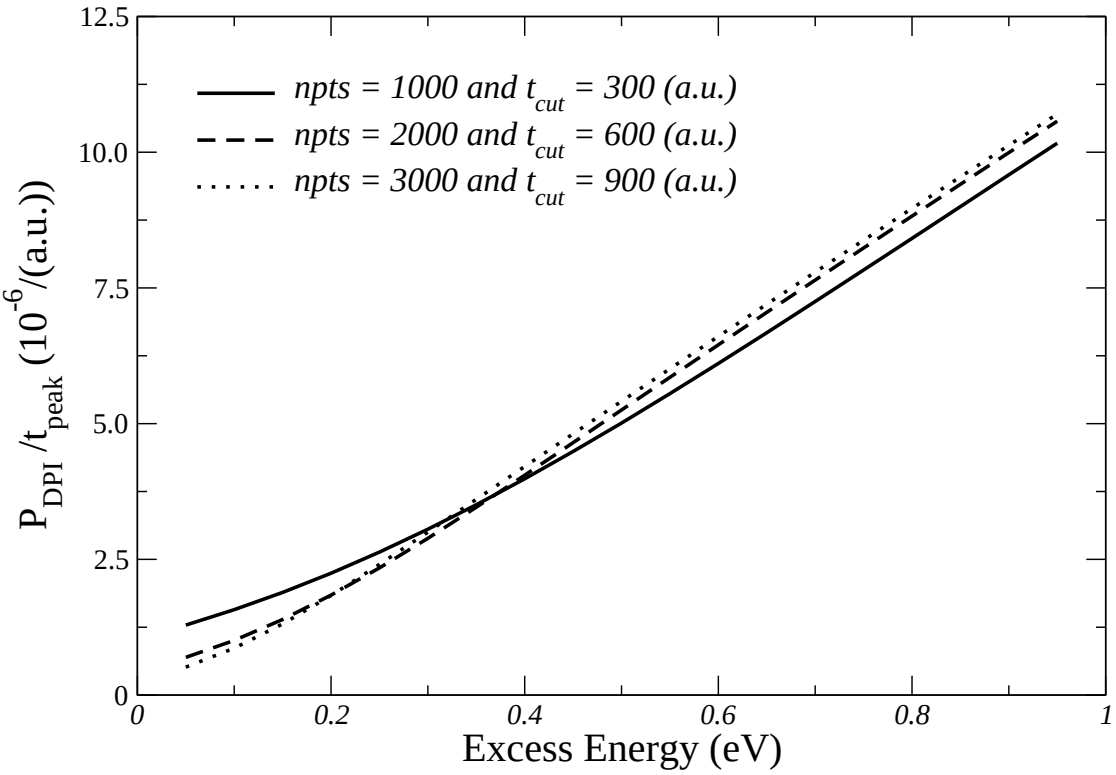

Figure 3.1: P_{DPI}/t_{peak} versus excess energy for photo-double ionization of $He(1s^2)$ for different boxes and pulse durations.

rather than the differences in δr. All the results we present in this chapter are converged within a few percent for all photon energies we consider.

Another problem we had to deal with was the slow convergence of the photo-double ionization probability as a function of time. Since we are studying threshold ionization, energy of the incoming photon in the energy space is centered close to the threshold with a width controlled by how long the source term is on. The longer the source term is kept on, sharper the energy distribution is and therefore smaller the contribution to the double ionization probability from other energies in our energy distribution. But the propagation

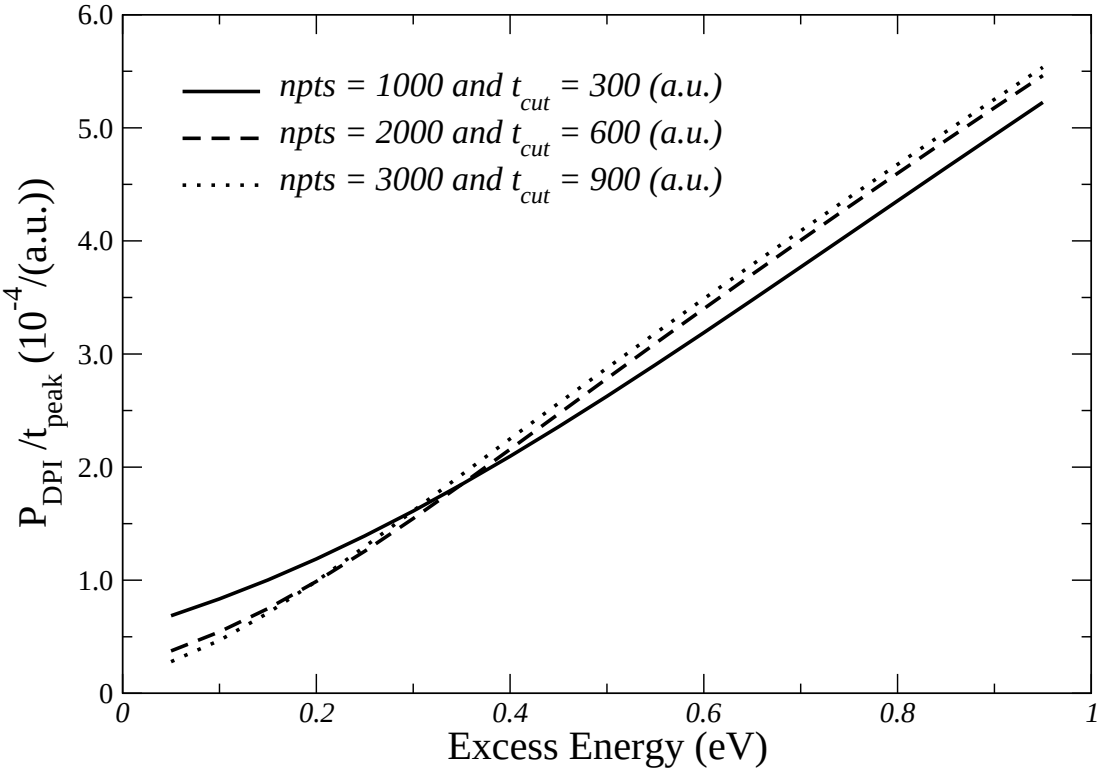

Figure 3.2: P_{DPI}/t_{peak} versus excess energy for photo-double ionization of $He(1s2s)$ for different boxes and pulse durations.

time $t_{\rm f}$ is also limited by the box size $r_{\rm f}$ due to the reflections from the box edge. Furthermore, the source term must be turned off and the wave function should have time to evolve before the the projections are done for the extracted double ionization probabilities to be meaningful. We have found that for a given box size r_f the most effective time we could keep the source term on was half the propagation time which was twice the box size in atomic units. Therefore $t_{\rm cut} = t_f/2$ and $t_{\rm peak} = t_{\rm cut}/2$ in Eq.(3.3). We then fit the double ionization probability to the form $A + B/(t - t_{\rm peak}) + C/(t - t_{\rm peak})^2$ for the last quarter of the propagation time. The coefficient A is then the $t \rightarrow \infty$ extrapolated double ionization probability. We examined the convergence of this extrapolated double ionization probability with respect to the box size.

Figs. 3.3 and 3.4 show the scaled photo-double ionization probabilities at various excess energies above the threshold for ionization out of the ground $1s^2(^1S)$ and the first excited $1s2s(^1S)$ states of He as a function of time. Notice the extremely slow convergence of the scaled probability at each excess energy for $t > 1000$ (a.u.), which forced us to extrapolate the scaled double ionization probabilities to $t \rightarrow \infty$ to estimate the actual ionization probability without having to propagate the wave function of the system too much longer.

The extrapolated photo-double ionization probabilities scaled by $t_{\rm peak}$ for the ground state $1s^2(^1S)$ Fig. 3.5 and the first excited state $1s2s(^1S)$ Fig. 3.6 of helium are plotted as a function of the excess energy within 1.0 eV above the double ionization threshold. These scaled probabilities were obtained inside a box that is defined on a uniform two-dimensional lattice of 3082×3082 points with a lattice spacing of $\delta r = 0.3$ (a.u.) in both

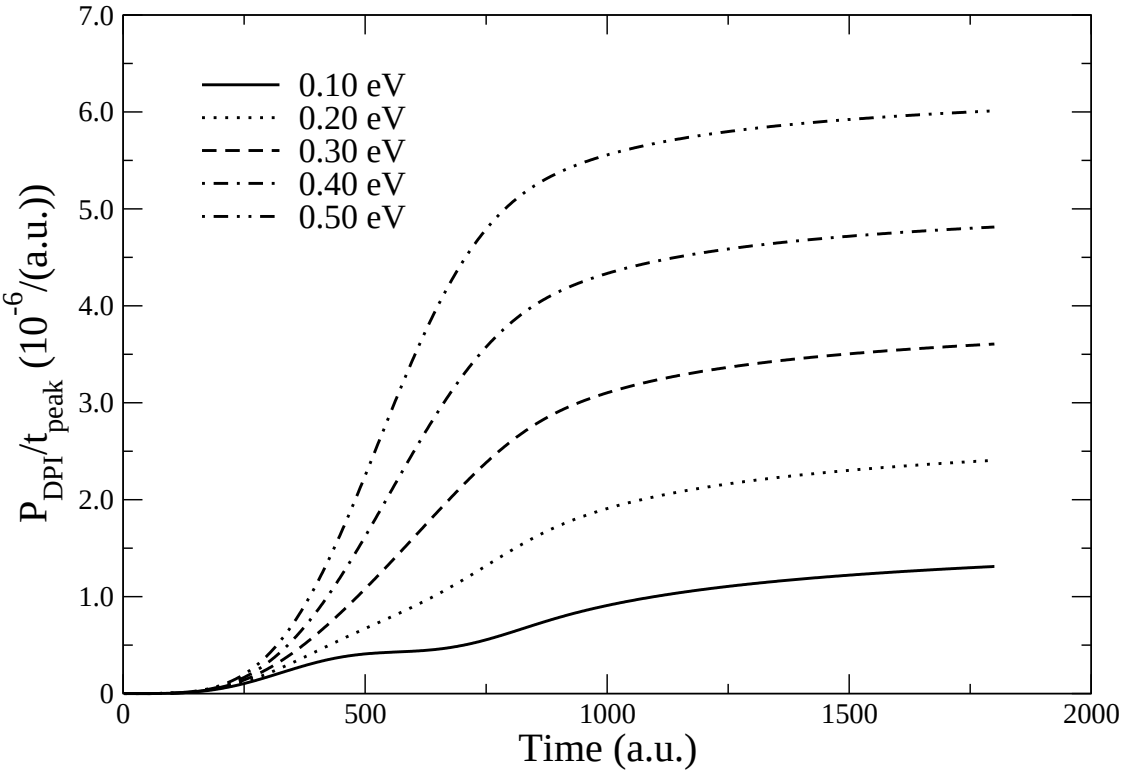

Figure 3.3: P_{DPI}/t_{peak} as a function of time for double ionization out of $He(1s^2)$.

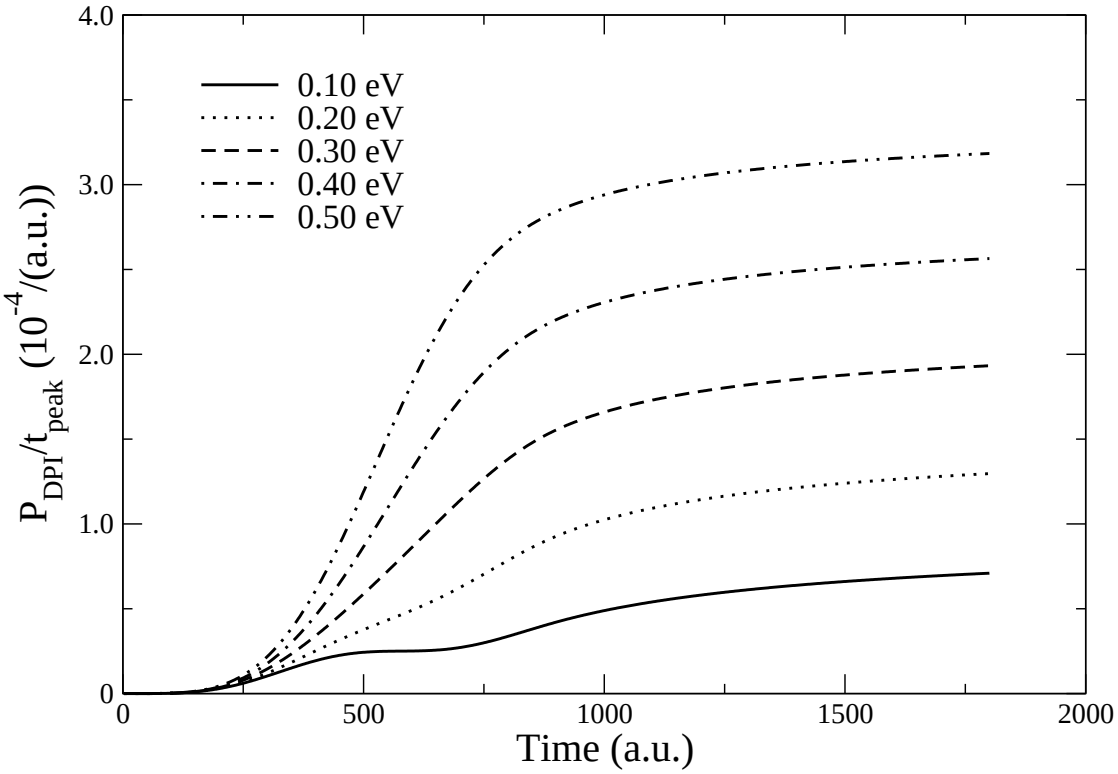

Figure 3.4: P_{DPI}/t_{peak} as a function of time for double ionization out of $He(1s2s)$.

directions. This extends the box out to 924.6 (a.u.) in both directions. On top of the scaled probabilities, we also plotted the Wannier power law, i.e. $aE_{exc}^{1.056}$ where $a = 3.8387 \times 10^{-4}$ for $1s^2(^1S)$ and $a = 5.4223 \times 10^{-3}$ for $1s2s(^1S)$, convolved to our spectral distribution for $t_{\rm f} = 1800$ (au.). As one can see, our results are in good agreement with the convolved Wannier law.

To see if there are any oscillations in the double ionization probability, we have also plotted the difference Δ between the calculated probabilities and the convolved Wannier law on top of each graph. As is evident from the upper panels in Figs. 3.5 and 3.6, the deviation of our results from the Wannier law is about two orders of magnitude smaller than the double ionization probability itself, whereas the experimentally observed oscillations reported in Refs. [24] and [25] are $\sim 10\%$ effect for Be [25] and $\sim 20\%$ effect for Li [24].

This implies that the oscillations in our residual plots are not physical but merely due to the fitting process and numerical uncertainties. Also note that the range of validity of the Wannier law shrinks as one starts the ionization from the excited state. This is expected since Wannier law assumes both electrons leave the atom back to back with equal energies which is better realized if the atoms start out from same n-shell.

3.4 Conclusions

In this chapter, we have presented results of our non-perturbative time-dependent calculations of photo-double ionization probabilities of He out of the ground and the first excited states $1s2s(^1S)$ in a collinear s-wave model near double ionization threshold. Using

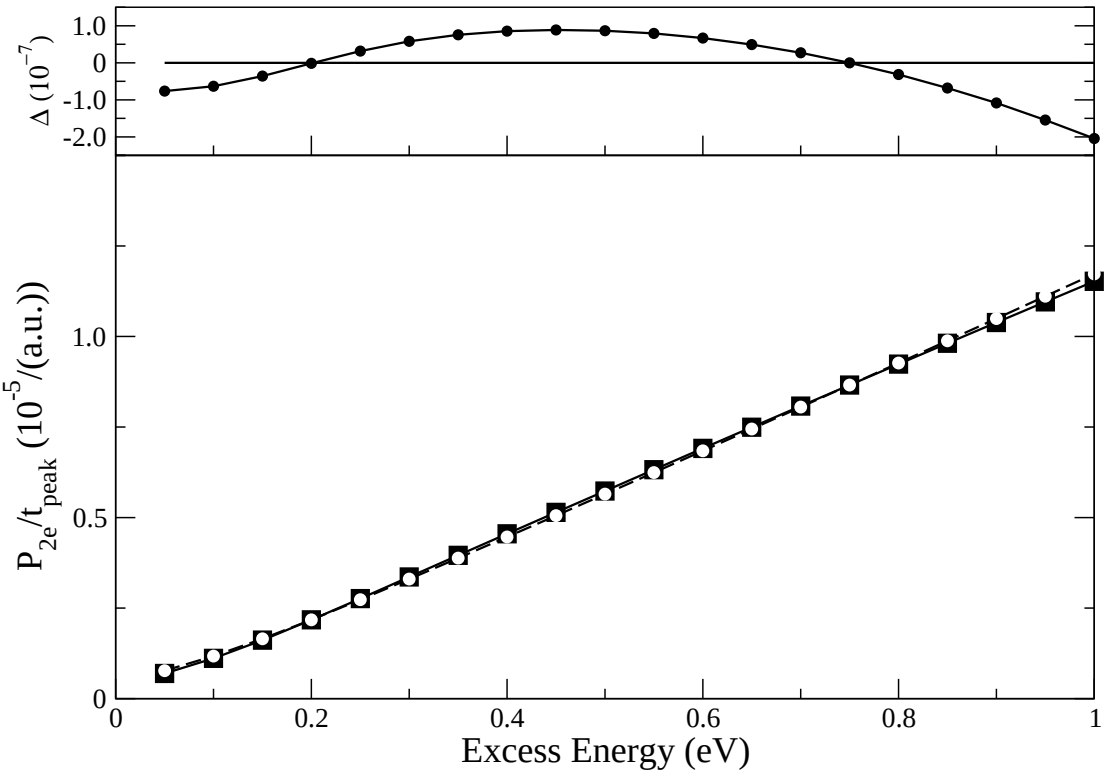

Figure 3.5: Calculated P_{DPI}/t_{peak} (■) and the fitted convolved Wannier power law (○) versus excess energy for photo-double ionization of $He(1s^2)$. The upper panel is showing the difference between the two.

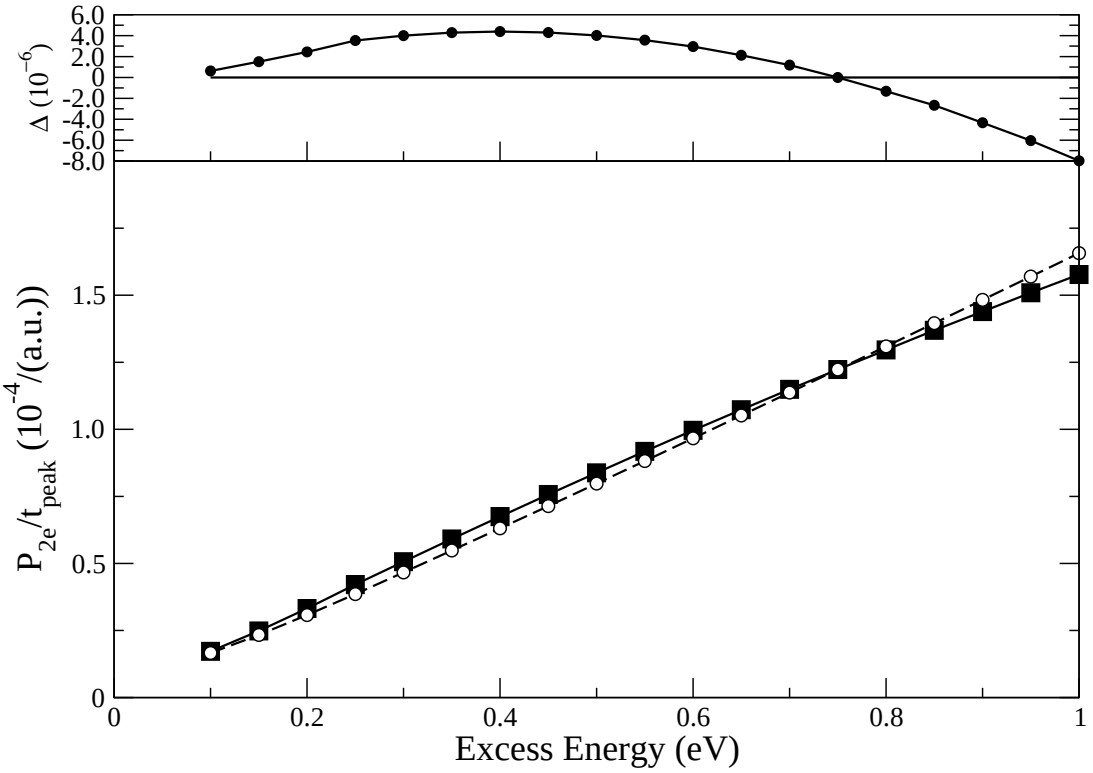

Figure 3.6: Calculated P_{DPI}/t_{peak} (■) and the convolved Wannier power law (○) versus excess energy for photo-double ionization of $He(1s2s)$. The upper panel is showing the difference between the two.

the collinear model instead of the actual full three-dimensional electron-electron interaction reduced the computational burden substantially, enabling us to perform many convergence checks with respect to the box size, lattice spacing, time step, and the pulse width, which let us reduce the size of the numerical uncertainties below a couple percent level. Due to the slow convergence of the double ionization probability as function of time, we have extrapolated the time-dependent ionization probabilities to $t \rightarrow \infty$ for each incident photon energy we considered, and taken the extrapolated values as the actual double ionization probabilities. We have also convolved our excess energy dependent ionization probabilities with the gaussian laser pulse we used to ionize the atom, to further account for the contributions from the energy components in the gaussian laser pulse other than the central energy component. This is important in getting the correct energy dependent behaviour near threshold because the classical Wannier power law assumes an energy distribution of zero width.

Our investigation of the ionization probability near threshold as a function of the excess energy confirmed the Wannier power law for the ionization out of both the ground and the singlet excited state. We have observed deviations from the Wannier Power law which are two orders of magnitude smaller than the ionization probabilities themselves in each case and have concluded that these oscillations are well within the numerical uncertainties of our calculations. We have found that the range of validity for the Wannier power law is shorter for the singlet excited state $1s2s(^1S)$ than it is for the ground state. This is expected since the assumption of the Wannier theory that the two electrons leaving the atom have approximately the same distance from the nucleus holds best for the ground state than

for the excited in which the electrons start out at different distances from the nucleus. We have observed that inclusion of the higher-order terms in the Wannier law in fitting our convolved results to the Wannier law gives better agreement between the Wannier law and our results at higher energies, extending the range of validity of the Wannier law.

CHAPTER 4

ELECTRON IMPACT IONIZATION OF HIGHLY EXCITED HYDROGEN-LIKE IONS IN A COLLINEAR s-WAVE MODEL

4.1 Introduction

According to the Bohr correspondence principle, the quantum mechanical description of a physical system should yield classical dynamics in the appropriate limit. Although there is no common agreement on how this limit should be defined, the most widely accepted definition is in terms of large quantum numbers. The classical-quantum correspondence in this context has been subject to many theoretical studies [29, 30, 31] as well as to experiments with Rydberg atoms [32]. There are systems which were found to violate the correspondence principle [30] as well as ones that fulfilled it exactly without taking any limits [31]. In a recent experiment by Nagesha and MacAdam [1], highly excited Na Rydberg atoms with principal quantum numbers of $n = 35 - 51$ revealed quite large electron-impact ionization cross sections compared to a formula designed to estimate the ionization cross sections out of excited states within an n-manifold, and a theory [33] based on low-n data. The discrepancy between the experiment and the theoretical models suggests that electron-impact ionization from Rydberg states may exhibit peculiar dynamics.

Ionization by electron-impact out of highly excited states would be expected to yield cross sections that are consistent with classical models at sufficiently high quantum numbers. However, the convergence to classical dynamics may very well depend on the properties of the atom, such as its ionic charge or the strength that the electron interacts with an external system or source. The question as to how well the atomic electron can be described classically as the principal quantum number increases is the focus of the present study. We investigate electron-impact ionization of H-like ions up to $Z = 6$ for various electron-impact energies. We performed calculations up to $n = 25$ in initial principal quantum number using a time-dependent close-coupling (TDCC) method in a collinear s-wave model. We contrast results of these calculations with those from collinear s-wave classical trajectory Monte Carlo (CTMC), distorted-wave (DW), and R-Matrix calculations.

Although electron-impact ionization has been covered extensively in the literature (e.g. see Ref. [34, 35, 36] and references therein), there has only been a few non-perturbative calculations for the electron-impact ionization from low excited states [37, 38, 39]. A recent paper by Griffin *et al.* [40] present results from a series of non-perturbative quantal calculations for electron-impact ionization from H, Li^{2+}, and B^{4+} up to $n = 4$ in comparison to fully three dimensional CTMC and perturbative distorted-wave calculations. Their non-perturbative calculations employed primarily the R-Matrix with pseudo states (RMPS) method whose results compared very well with those from their TDCC calculations for ionization from selected excited states. Using the non-perturbative results as benchmarks, their study indicated that the CTMC results were reasonably accurate for

hydrogen, but for the ions the CTMC results were too large and did not improve with the principal quantum number.

Since both the number of n, l terms and the size of the target increase rapidly with principal quantum number, the computational resources required to study ionization out of highly excited states become prohibitively large for a full three-dimensional model. Therefore, in this study, we restrict ourselves to the collinear s-wave model where both electrons move on a straight line. It has been shown that this model includes the essential physics of the ionization process close to the threshold [44, 41, 42] and yields the correct Wannier threshold law for single ionization, i.e. $\sigma \sim E^{1.128}$. The interaction potential between the electrons is $1/(r_1 + r_2)$ which we refer to as the collinear s-wave potential.

In the next section, we discuss the theoretical methods employed; in Sec. III, we present our results; and in Sec. IV, we discuss their signficance. We use atomic units throughout this chapter, unless mentioned otherwise. The work presented in this chapter has been published as a paper in Physical Review A [43].

4.2 Theory

We first describe the collinear s-wave TDCC model and discuss the various convergence checks performed. Next we discuss the collinear s-wave CTMC, DW, and RMPS methods that we employed. Since the accuracy of the results is important, we make special effort to discuss the methods we used to insure convergence.

4.2.1 The time-dependent wave packet method using collinear s-wave model

In the collinear s-wave model where both electrons move on a straight line, the Hamiltonian reads [28]

$$H = \sum_{\alpha=1}^{2} \left(\frac{p_\alpha^2}{2} - \frac{Z}{r_\alpha} \right) + \frac{1}{r_1 + r_2}. \tag{4.1}$$

If the H-like ion is initially in the ns state, the symmetrized initial wave function at $t = 0$ is

$$\psi(r_1, r_2, t = 0) = \frac{1}{\sqrt{2}} \Big[\varphi_{ns}(r_1) G_{ks}(r_2) + \varphi_{ns}(r_2) G_{ks}(r_1) \Big] \tag{4.2}$$

where φ_{ns} is an eigenstate of the H-like ion and G_{ks} is the Gaussian representing the incoming electron of energy $E = k^2/2$ and momentum k. It is given by:

$$G_{ks}(r) = e^{-i\phi(r)} e^{-\left(\frac{\Lambda}{r_f - r_0}\right)^2 \left(r - \frac{1}{2}(r_f + r_0)\right)^2}, \tag{4.3}$$

where $r_0 = 2n^2$ and the constant Λ is chosen such that $e^{-(\Lambda/2)^2} \ll 1$ and $G_{ks}(r)$ can be considered to be zero at $r = r_0$ and $r = r_f$. In our calculations, we have taken Λ to be 12. To reduce the energy spread of the packet due to the phase accumulations, the WKB phase $\phi(r)$ is evaluated as

$$\phi(r) = \int_0^r \sqrt{2(E + (Z-1)/r')} dr'. \tag{4.4}$$

The wave packet is discretized on a 2 dimensional square root mesh where $r_j = j^2 \delta r$ with $\delta r = r_f/N^2$. The maximum grid spacing on this mesh can be evaluated by $\delta r_{max} = (2N - 1)\delta r$ and is two times larger than that for a linear mesh.

Time propagation of the Schrödinger equation is carried out by means of lowest order split operator technique:

$$\begin{aligned}\psi(t+\delta t) &= \exp\left(-i\frac{\delta t}{2(r_1+r_2)}\right)\exp\left(-iH_2\delta t\right) \\ &\quad\times\exp\left(-iH_1\delta t\right)\exp\left(-i\frac{\delta t}{2(r_1+r_2)}\right)\psi(t),\end{aligned} \tag{4.5}$$

where $H_\alpha = p_\alpha^2/2 - Z/r_\alpha$ and $(\alpha = 1, 2)$. Using the lowest order Padè approximation for the exponential one particle operators $\exp\left(-iH_\alpha\delta t/2\right)$, the time propagation scheme given by Eq. (4.5) becomes

$$\begin{aligned}\psi(t+\delta t) &= \exp\left(-i\frac{\delta t}{2(r_1+r_2)}\right)\left[\frac{1-iH_2\delta t/2}{1+iH_2\delta t/2}\right] \\ &\quad\times\left[\frac{1-iH_1\delta t/2}{1+iH_1\delta t/2}\right]\exp\left(-i\frac{\delta t}{2(r_1+r_2)}\right)\psi(t).\end{aligned} \tag{4.6}$$

The numerical error for this lowest order Padè approximation scales like δt^3 and the approximated operator is exactly unitary. The probability of finding both electrons in the continuum at time t is calculated by making use of the *bound* states φ_{ns},

$$\begin{aligned}\mathcal{P}_{2e^-}(t) &= 1 - 2\sum_n \int \left|\int \psi(r_1,r_2,t)\varphi_{ns}(r_1)dr_1\right|^2 dr_2 \\ &\quad+\sum_n\sum_m \left|\int\int \psi(r_1,r_2,t)\varphi_{ns}(r_1)\varphi_{ms}(r_2)dr_1dr_2\right|^2,\end{aligned} \tag{4.7}$$

provided that the wave function is normalized to unity [45]. The ionization cross section σ_{2e^-} is calculated from the ionization probability using $\sigma_{2e^-} = (\pi/k^2)\mathcal{P}_{2e^-}$.

To increase the accuracy of the computed projections, we have calculated the eigenstates in a box two times larger than the box in which $\psi_{j,k}$ is discretized. This gives a finer spacing of states in energy and decreases the effect of a finite box. In discretization of the Hamiltonian on the square root mesh, we have used a three point differencing scheme for the second derivatives. The action of $p^2/2$ on the eigenstate φ_j is calculated as [46]:

$$\begin{aligned}\frac{1}{2}p^2\varphi_j &= -\frac{\varphi_{j-1}}{\sqrt{(r_j - r_{j-1})(r_{j-1} - r_{j-2})}(r_j - r_{j-1})} \\ &+\frac{\varphi_j}{(r_{j+1} - r_j)(r_j - r_{j-1})} \\ &-\frac{\varphi_{j+1}}{\sqrt{(r_{j+1} - r_j)(r_j - r_{j-1})}(r_{j+1} - r_j)}\end{aligned} \tag{4.8}$$

where $\varphi_j = R_j/\sqrt{\delta r_j}$ and R_j is the actual radial orbital. The advantage of using a square root mesh is that it enables us to employ much larger boxes than the uniform mesh does. To check the effect of using a square root mesh on our results, we have also performed a few trial calculations on a uniform mesh and compared the results with those from the square root mesh calculations. We did not see any significant differences in the projected probabilities.

We use scaled units to describe the electron-impact energy E in our calculations. Energies of the incoming electron are chosen in multiples of the binding energy of the initial state. The energy of the incoming electron is therefore defined by $E = [Z^2/(2n^2)]E_{sc}$ where we call E_{sc} the scaled electron-impact energy.

We have checked convergence of the TDCC results with respect to box size r_f, number of points N, and time step δt for the time propagation. For example, for an atom in an initial

state with $n = 12$ and an incoming electron with scaled energy $E_{sc} = 9.5$, the projected ionization probability for all Z in a 2250 (a.u.) box with 2500 points remains well within a percent if one increases the number points to 5000 while keeping r_f fixed. When the number of points is kept fixed at 2500 and the box size is doubled, the probability changes by $\sim 2\%$ for $Z = 1$. In cases of $Z = 3$ and $Z = 5$, the differences are within $\sim 1\%$. When both r_f and N are doubled to 4500 and 5000 respectively, the results were within $\sim 3\%$ of the $(r_f, N) = (2250, 5000)$ results for $Z = 1$. For $Z = 5$ the difference was $\lesssim 1\%$. We have found that for sufficiently high n, amplitudes for super-elastic scattering down to low-n states are very small, enabling us to employ large δr_{max} and r_f. We carried out similar analyses for all the initial states and several ion stages in our calculations and the results we present are converged within a few percent.

To be able to use the same converged box parameters and time steps for all Z, we scale the length and time according to $r_j = \zeta_j/Z$ and $t = \tau/Z^2$. The full time-dependent Shrödinger equation that needs to be solved is

$$i\frac{\partial}{\partial t}\psi = \left[\sum_{\alpha=1}^{2}\left(\frac{1}{2}\frac{\partial^2}{\partial r_\alpha^2} - \frac{Z}{r_\alpha}\right) + \frac{1}{r_1 + r_2}\right]\psi(r_1, r_2). \tag{4.9}$$

After scaling and dividing through by Z, Eq. (4.9) becomes

$$i\frac{\partial}{\partial \tau}\psi = \left[\sum_{\alpha=1}^{2}\left(\frac{1}{2}\frac{\partial^2}{\partial \zeta_\alpha^2} - \frac{1}{\zeta_\alpha}\right) + \frac{1}{Z(\zeta_1 + \zeta_2)}\right]\psi(\zeta_1, \zeta_2) \tag{4.10}$$

which is equivalent to the hydrogen problem in scaled coordinates and time, except the scaled electron-electron interaction potential is now $1/[Z(\zeta_1 + \zeta_2)]$. In the same manner,

scaling the time independent Schrödinger equation for the evaluation of the eigenenergies and the eigenstates, we solve the equation:

$$-\frac{1}{2}\frac{\partial^2\phi(\zeta)}{\partial\zeta^2} - \frac{\phi(\zeta)}{\zeta} = \tilde{\epsilon}\phi(\zeta) \tag{4.11}$$

with the Z-scaled energy $\tilde{\epsilon} = \epsilon/Z^2$. Note that with the use of the Z-scaled potential, the electron-impact energy becomes $E = [1/(2n^2)]E_{sc}$.

For B^{4+}, for an initial state with $n = 4$ and with a scaled impact energy of $E_{sc} = 9.5$, the difference in the ionization probability between the calculations using the collinear s-wave potential and the Z-scaled collinear s-wave potential is found to be within a percent.

4.2.2 Classical trajectory Monte Carlo method

In the CTMC method, we solved the classical equations of motion to compute the classical probability for ionization. The classical equations of motion scale. This means the ionization probability in the collinear s-wave model only depends on Z and on the ratio of the kinetic energy of the incident electron to the binding energy of the bound electron; we define this to be the scaled incident energy, E_{sc}. In addition to Z and E_{sc}, the quantum results depend on the binding energy of the target state.

The length and time scalings are

$$r = \rho\frac{Z}{E_b} \qquad t = \tau\frac{Z}{E_b^{3/2}} \tag{4.12}$$

where E_b is the binding energy of the attached electron. For this choice of scaling, the scaled energy of the bound electron is -1 and the incident energy is E_{sc}. A bound energy of -1 corresponds to $n = 1/\sqrt{2}$ and a classical period of $2\pi n^3 = \pi/\sqrt{2}$.

With this scaling the fully three dimensional equations of motion become

$$\frac{d\vec{\nu}_1}{d\tau} = -\frac{\vec{\rho}_1}{\rho_1^3} + \frac{1}{Z}\frac{\vec{\rho}_{12}}{\rho_{12}^3} \qquad \frac{d\vec{\rho_1}}{d\tau} = \vec{\nu}_1 \tag{4.13}$$

$$\frac{d\vec{\nu}_2}{d\tau} = -\frac{\vec{\rho}_2}{\rho_2^3} - \frac{1}{Z}\frac{\vec{\rho}_{12}}{\rho_{12}^3} \qquad \frac{d\vec{\rho_2}}{d\tau} = \vec{\nu}_2 \tag{4.14}$$

where $\vec{\rho}_{12} = \vec{\rho}_1 - \vec{\rho}_2$. For the collinear s-wave model, the scaled equations of motion are

$$\frac{d\nu_1}{d\tau} = -\frac{1}{\rho_1^2} + \frac{1}{Z}\frac{1}{(\rho_1+\rho_2)^2} \qquad \frac{d\rho_1}{d\tau} = \nu_1 \tag{4.15}$$

$$\frac{d\nu_2}{d\tau} = -\frac{1}{\rho_2^2} + \frac{1}{Z}\frac{1}{(\rho_1+\rho_2)^2} \qquad \frac{d\rho_2}{d\tau} = \nu_2 \tag{4.16}$$

with the additional condition of an infinitely hard wall at a small, positive value of ρ, after which the electron cannot move any closer to $\rho = 0$. The infinitely hard wall reverses the sign of the velocity and keeps both electrons at positive ρ. The position of the wall affects the ionization probability, but the effect decreases as the wall moves closer to $\rho = 0$. We chose a position, 5×10^{-5}, where the ionization probability was changed by much less than a percent. Note that the nuclear charge Z manifests itself in the scaled equations of motion by multiplying the electron-electron interaction by $1/Z$. From this it is clear that the ionization (which depends on the electron-electron interaction) decreases with increasing Z.

If there were no scattering, the bound electron would be limited to a region $0 < \rho \leq 1$. The initial conditions of the bound electron were chosen to give a micro-canonical ensemble. For the collinear case, this means the starting position and velocity can be specified by a single random parameter, η, in the range $0 \leq \eta \leq 1$; if η is chosen correctly the distribution is flat in η. The microcanonical ensemble is given where the parameter η is the fraction of a period of the bound motion and the position and velocity at $\eta = 0$ is taken to be the outer turning point, $\rho = 1$,$\nu = 0$. The initial conditions for the fully three dimensional case are somewhat more complicated but are well known (e.g. see Ref. [47]).

The incident electron is started at a distance $\rho_2 = 100$. In the collinear s-wave calculation, the initial velocity is $\nu_2 = -\sqrt{2(E_{sc} - V_0)}$ where $V_0 = -1/\rho_2(0) + (1/Z)(1/[\rho_1(0) + \rho_2(0)])$ is the initial potential energy for electron 2. With this definition, the total energy is exactly $E = -1 + E_{sc}$. We run the trajectories until at least one electron reaches the distance $\rho = 120$, at which point the energies of the electrons are computed. The η range for which the energies of both of the electrons are positive gives the ionization probability $\mathcal{P}_{2e^-}$, which is converted to cross section via $\sigma_{2e^-} = (\pi/k^2)\mathcal{P}_{2e^-}$. The initial conditions for the three dimensional calculation is similar but includes the impact parameter of the incident electron.

For the collinear s-wave model, the initial conditions only depend on one parameter, η. Therefore, it makes physical sense to examine the energies of the electrons versus η. In Fig. 4.1, we show the energies of the two electrons (solid and dashed curves) versus η for $Z = 1$ and $E_{sc} = 9.5$. It is clear that relatively little energy is transferred to the bound electron (solid curve) except in a region near $\eta = 0.25$ which is shown as an inset. The region

where both energies are positive corresponds to ionization. Because the microcanonical distribution is flat in η and the range of η is one, the fraction ionized simply corresponds to the range of η where both energies are positive. The energies versus η have similar types of shape for all Z. There is a small region where substantial energy exchange can occur; the width of the region decreases with increasing Z. The large energy transfer occurs when the incoming electron and the bound electron are moving in the same direction near the nucleus; for this type of motion, the incoming electron can do substantial work on the bound electron, giving it enough energy to ionize.

4.2.3 Collinear distorted-wave method

In the collinear s-wave distorted-wave theory, the ^1S cross section for single ionization of a hydrogenic ion is given by:

$$\sigma = \frac{32}{k_i^3} \int_0^{E/2} \frac{d(k_e^2/2)}{k_e k_f} \left[\mathfrak{R}(k_e s, k_f s; ns, k_i s) + \mathfrak{R}(k_f s, k_e s; ns, k_i s) \right]^2 \tag{4.17}$$

where the linear momenta (k_i, k_e, k_f) correspond to the incoming, ejected, and outgoing electron, respectively. The direct radial matrix element is:

$$\mathfrak{R}(k_e s, k_f s; ns, k_i s) = \int_0^\infty dr_1 \int_0^\infty dr_2 \, \frac{P_{k_e s}(r_1) P_{k_f s}(r_2) P_{ns}(r_1) P_{k_i s}(r_2)}{r_1 + r_2} \tag{4.18}$$

with a similar expression for the exchange term. The radial distorted waves needed to evaluate the radial matrix elements are all Coulomb waves [48].

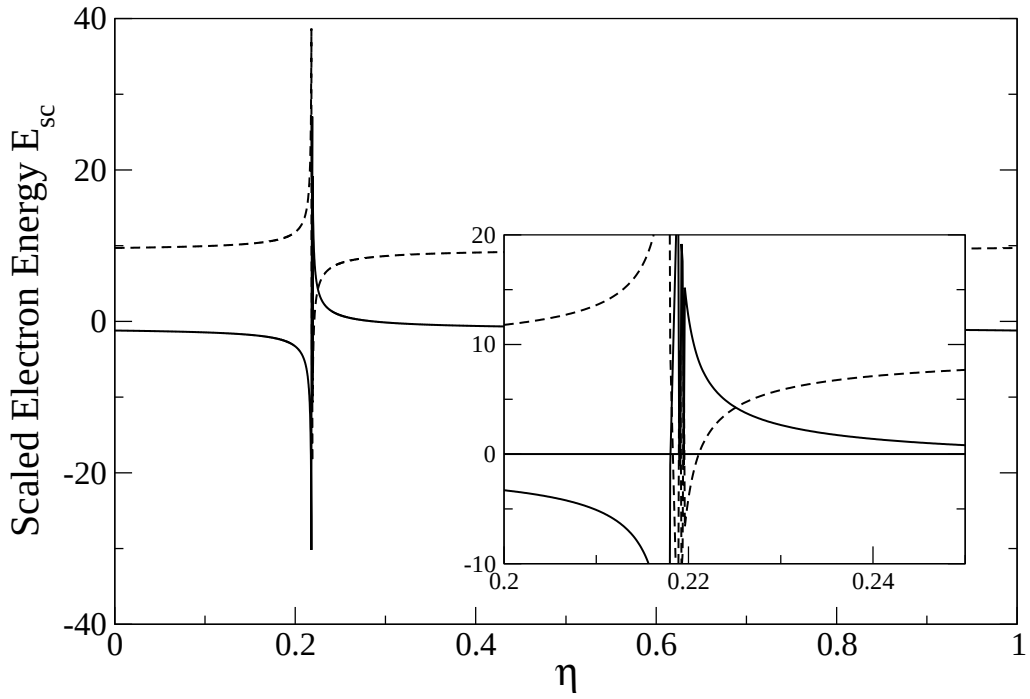

Figure 4.1: Scaled final energy of the classical bound (solid curve) and incoming (dashed curve) electrons versus the initial phase, η, of the bound electron. The initial position and velocity of the electron, ρ and ν, are found by solving the classical equations of motion for a time given by η times the Rydberg period with $\rho(0) = 1$ and $\nu(0) = 0$. This graph shows the result for $Z = 1$ and $E_{sc} = 9.5$. Note that the width of the region where η is positive for both electrons (shown in the insert) is the ionization probability.

4.2.4 Collinear R-Matrix method

In the collinear s-wave R-Matrix method [49], symmetrized product states of single-particle orbitals generated by the diagonalization of the one electron Hamiltonian

$$h(r) = \frac{p^2}{2} - \frac{Z}{r}, \tag{4.19}$$

are used to span the basis for the diagonalization of the two electron Hamiltonian,

$$\mathcal{H}_R = H(r_1, r_2) + \frac{1}{2}\delta(r_1 - R)\frac{\partial}{\partial r_1} + \frac{1}{2}\delta(r_2 - R)\frac{\partial}{\partial r_2} \tag{4.20}$$

where R is the box size and the Bloch operators $(1/2)\delta(r_\alpha - R)(\partial/\partial r_\alpha)$ ensure the Hermiticity of $\mathcal{H}_R$. The ionization cross sections are calculated as a sum over all the excitation cross sections to positive energy states of the basis in which $\mathcal{H}_R$ is diagonalized to obtain the R-Matrix. The R-Matrix is related to the K and J Matrices, which are then used to determine the S Matrix. In this study, the excitation cross section from state i to state f is given by

$$\sigma_{i\to j}(E) = \frac{\pi}{k_i^2}\left|S_{ij} - \delta_{ij}\right|^2. \tag{4.21}$$

For electron-impact scattering from hydrogen, we used a 2400-point lattice with a uniform mesh spacing of $\delta r = 0.025$ and a box size of $R = 60.0$ (a.u.).

4.3 Results

4.3.1 Effect of using a model potential: $\frac{1}{r_1+r_2}$ versus $\frac{1}{r_>}$

Besides fully three dimensional treatments, the problem of electron-impact scattering from hydrogen has been studied within simple s-wave models primarily to reduce the computational burden posed by solving the time-dependent Schrödinger equation in three dimensions. In one of these models, which was developed by Temkin [50] and Poet [51], the interaction potential between the electrons is described by the s-wave term of the partial wave expansion of the true electron-electron interaction potential, i.e. $1/|\vec{r}_1 - \vec{r}_2|$, and is $1/r_>$. The Temkin-Poet model has been used extensively in the literature for studying electron-impact scattering from hydrogen atoms (see e.g. Refs. [34, 52, 53, 54, 49] and references therein). Our choice of the collinear s-wave model for studying electron-impact ionization stems from the fact that although the Temkin-Poet potential is exact for s-waves, it was shown not to yield the correct threshold law in one dimension [28] due to its cusp along the $r_1 = r_2$ ridge. This cusp weakly pushes the probability density away from the $r_1 = r_2$ ridge resulting in distortion of the depicted threshold law. On the other hand the collinear s-wave potential yields the correct threshold law.

One of the differences between the Temkin-Poet and the collinear models is that the collinear model potential is weaker than the exact s-wave potential of the Temkin-Poet model. As a consequence, the collinear DW method agrees very well with both TDCC and RMPS methods as demonstrated in the next two sections and Figs. 4.3 and 4.4. Due to the

perturbative nature of the DW method, a weaker potential means better agreement with the non-perturbative methods.

To demonstrate this point, we have carried out DW and RMPS calculations for ionization from ground state of hydrogen within Temkin-Poet model and compared to the cross sections obtained using the collinear s-wave model. Results from these two calculations are shown in Fig. 4.2. The pseudo resonances in our RMPS data were smoothed out using a least squares fit to obtain the smooth RMPS curves in Fig. 4.2. As expected, there is better agreement between the DW and RMPS for the collinear s-wave model potential than in the case of the Temkin-Poet model potential. Cross sections for electron-impact ionization obtained using the Temkin-Poet potential are roughly a factor of 3 larger than those obtained using the model potential.

4.3.2 Electron-impact ionization of hydrogen

Fig. 4.3 shows electron-impact ionization cross sections from fully quantal collinear s-wave TDCC, DW, and CTMC calculations for up to $n = 4$ of the hydrogen atom for the singlet symmetry of the initial wave packet. The CTMC result for $E_{sc} = 1.5$ starts out $\sim 44\%$ off the TDCC result at $n = 1$, then converges to the TDCC result by $n = 4$. Note that the agreement between the CTMC and the TDCC methods gets better with the increasing electron-impact energy.

The collinear s-wave DW results are in good agreement with the collinear s-wave TDCC for the ground state ionization. For ionization out of states with higher n, DW

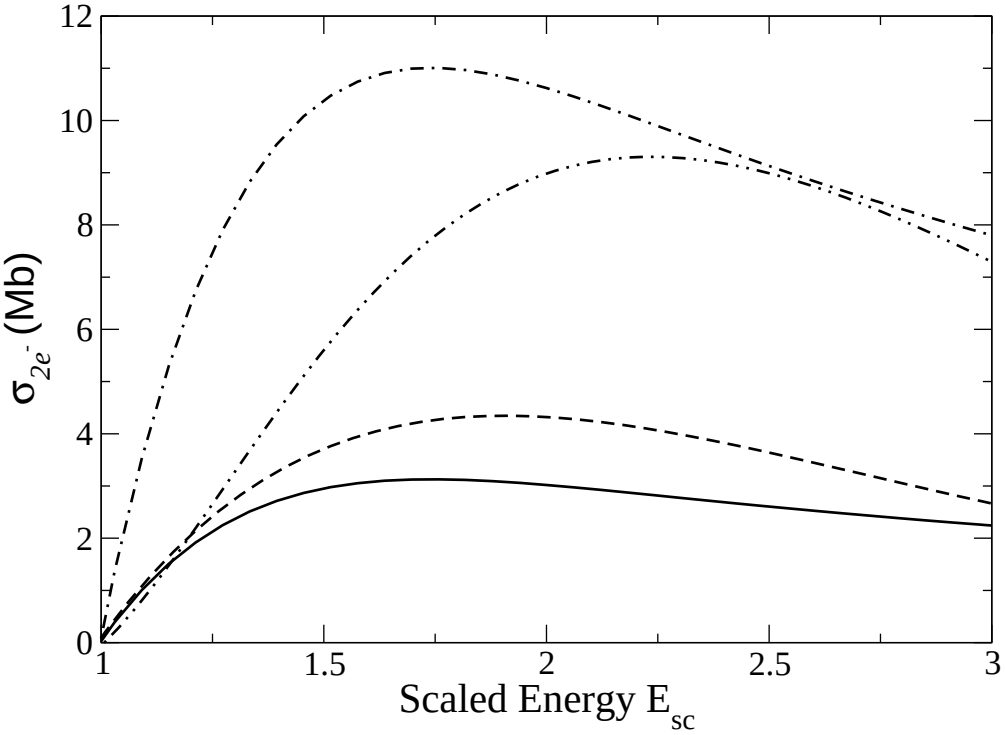

Figure 4.2: Ionization probability out of $n = 1$ for H versus the scaled energy of the incoming electron from collinear s-wave DW (solid curve), Temkin-Poet DW (dot-dash curve), collinear s-wave RMPS (dash curve) and Temkin-Poet RMPS (dot-dot-dash curve) calculations. Note that the agreement between the DW and RMPS is better for the weaker collinear s-wave model potential. The data are fitted using least squares method to obtain the smooth curves.

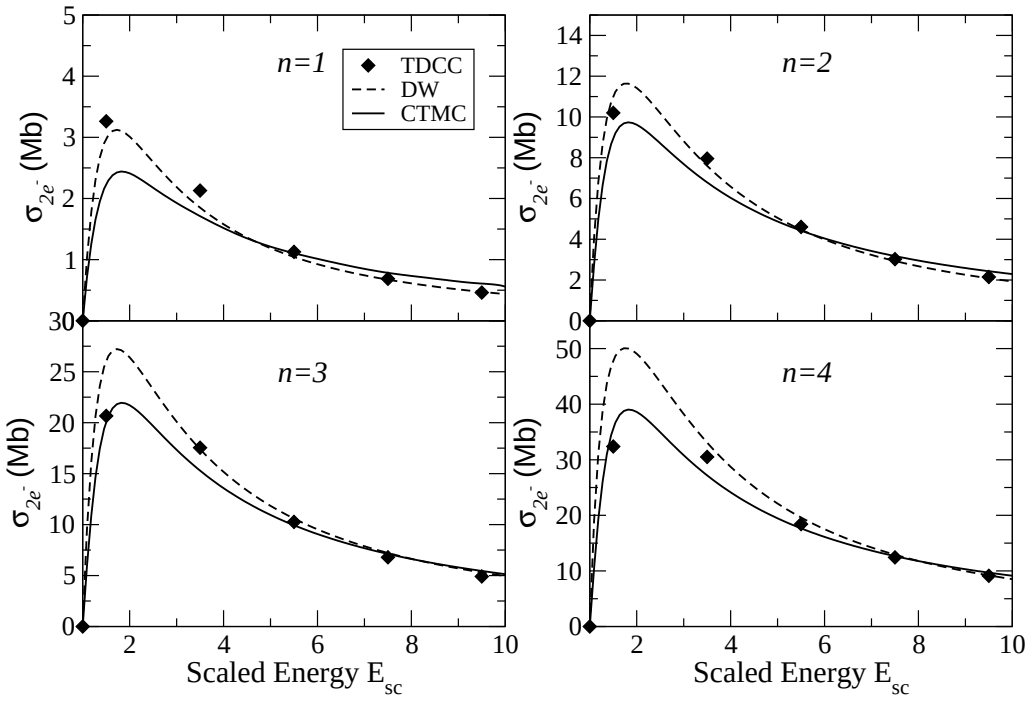

Figure 4.3: Ionization Cross sections for e^--$H(^1S)$ scattering from n up to 4 calculated in collinear DW, CTMC, RMPS, and s-wave TDCC methods as a function of the scaled energy E_{sc} of the incoming electron.

results slowly diverge from both TDCC and CTMC cross sections. This observation is consistent with what has been seen from the fully three dimensional calculations [40].

We have further carried out collinear s-wave RMPS calculations to serve as a benchmark for our TDCC results. We have observed reasonable agreement between the collinear s-wave RMPS and TDCC cross sections for all n we show in Fig. 4.3. This agreement can be considered to be an independent confirmation of the convergence of the TDCC results since both results are obtained via completely different quantal methods.

4.3.3 Electron-impact ionization of B^{4+}

Electron impact ionization cross sections as a function of the scaled energy of the incoming electron from collinear s-wave DW, TDCC, and CTMC calculations are plotted for B^{4+} for initial states of $n = 1, 2, 4$ and 8 in Fig. 4.4 for the ^1S symmetry. Cross sections from the CTMC calculations at $E_{sc} = 1.5$ start out as $\sim 74\%$ larger than the TDCC cross sections at $n = 1$, then very slowly converge to the TDCC results. For instance, at $n = 8$ the CTMC result differs from the TDCC result by $\sim 60\%$ for scaled impact energy of 9.5. The agreement between the collinear s-wave TDCC and DW methods is excellent for all n plotted in Fig. 4.4. Despite being perturbative, DW works very well even for the highly excited states studied here because the interaction potential is weak and the transition energy is large. The inelastic cross section to nearby n's are not as accurate due to the small energy spacing between Rydberg levels. Contrary to the case of hydrogen, both TDCC and DW results are below the classical cross sections.

It is expected that the results of the CTMC calculation would not be as close to the wave packet results as the H cross sections since higher nuclear charge manifests less classical behavior. Therefore, to see how high in n one should go for B^{4+} to reach agreement with the CTMC results, we have performed TDCC calculations for $n = 1, 2, 4, 8, 12, 16, 20$ and 25 for the ^1S symmetry of the initial wave packet. The ionization probabilities versus the scaled energy of the incoming electron are plotted for all n in Fig. 4.5. The agreement between the CTMC and TDCC results improves substantially slower than it does for hydrogen as the principal quantum number n increases. For instance for $n = 25$, the CTMC results differ from the TDCC results by $\sim 17\%$ at $E_{sc} = 5.5$ and by $\sim 38\%$ at $E_{sc} = 9.5$.

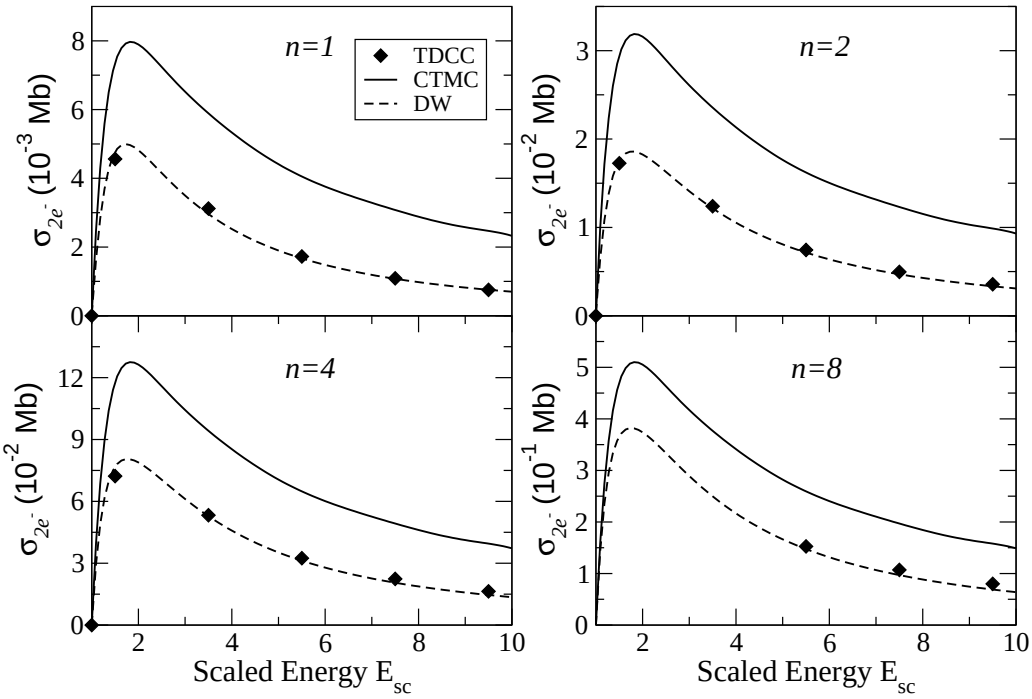

Figure 4.4: Ionization Cross sections for e^--$B^{4+}(^1S)$ scattering from $n = 1, 2, 4$ and 8 calculated in collinear DW, CTMC, and s-wave TDCC methods as a function of the scaled energy of the incoming electron.

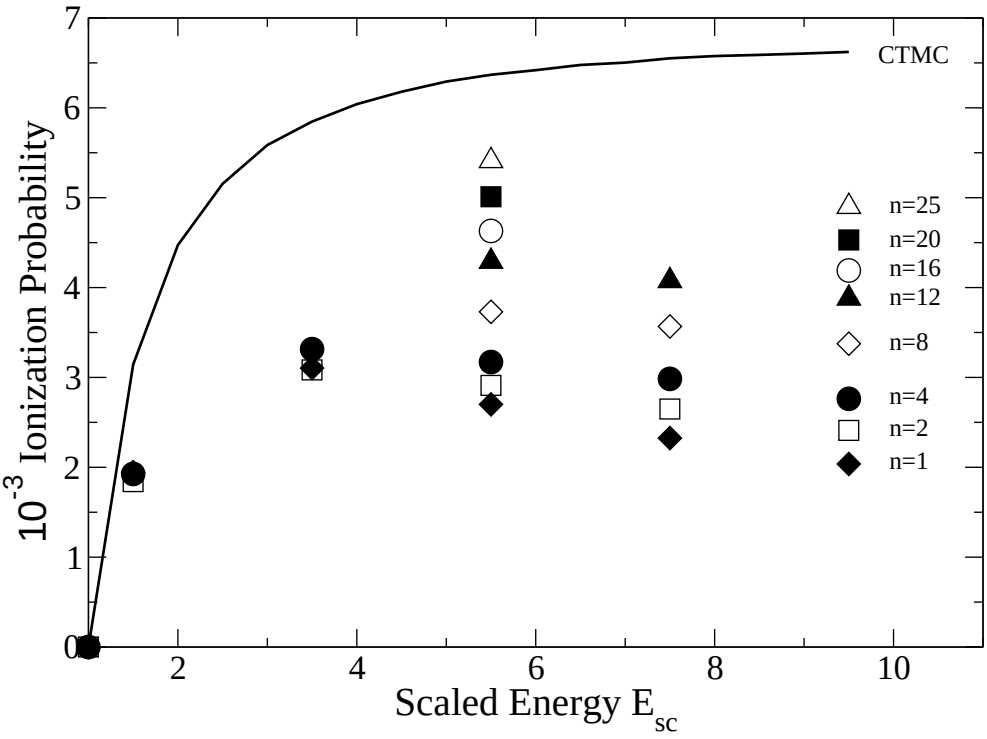

Figure 4.5: CTMC versus s-wave TDCC method for the electron impact ionization of B^{4+} for up to $n = 25$ for the ^1S symmetry of the initial wave packet.

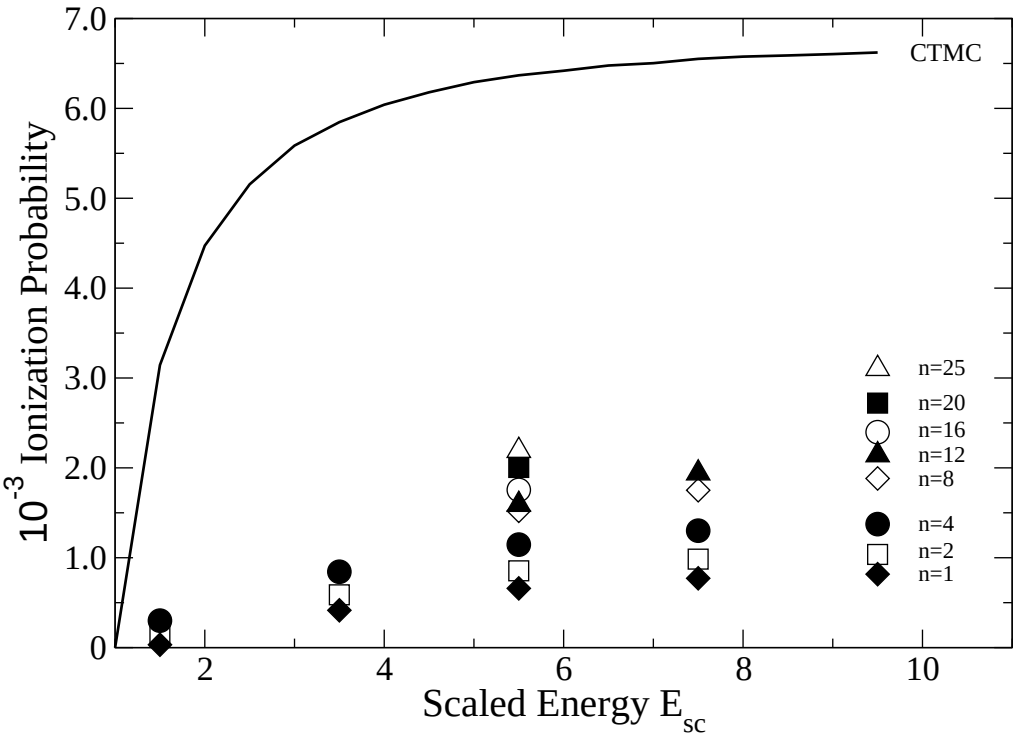

Figure 4.6: CTMC versus s-wave TDCC method for the electron-impact ionization of B^{4+} for up to $n = 25$ for the ^3S symmetry of the initial wave packet.

We have performed the same set of TDCC calculations for the ^3S symmetry of the initial wave packet and the results are seen in Fig. 4.6. Ionization probabilities for the ^3S symmetry are smaller than those for the ^1S symmetry as expected since the ^3S wave packet has a node along the $r_1 = r_2$ ridge. The ^3S result from the TDCC calculation for $n = 25$ at $E_{sc} = 9.5$ is about a factor of 2 smaller than that from the CTMC calculation.

4.3.4 Effect of the ion stage

Since going from $Z = 1$ to $Z = 5$ drastically decreased the speed of convergence to the CTMC results as a function of n, we repeated the collinear s-wave TDCC calculation

for an incoming electron with scaled energy of $E_{sc} = 9.5$ for $Z = 1$ through 6 for initial states with $n = 1, 2, 3, 4, 8, 12, 16, 20$ and 25 to see the effect of the ion stage, Z, on the convergence speed of the quantal ionization probabilities to the classical ones as a function of n. In Fig. 4.7, we have plotted the ratio $P^{QM}(n, Z)/P^{CM}(Z)$ for the ^1S symmetry of the initial wave packet where $P^{QM}(n, Z)$ is the ionization probability from the TDCC calculation and $P^{CM}(Z)$ is the CTMC result. As noted before, for the case of $Z = 1$ the TDCC method quickly converges to the CTMC result by $n = 4$ within $\sim 4\%$ and by $n = 8$ within $\lesssim 1\%$ for $E_{sc} = 9.5$. The oscillations about the CTMC result for higher n are at the couple percent level and they may be due to the overall numerical accuracy of the TDCC method, although they may also be due to quantum interference.

Fig. 4.8 shows $\ln[P^{QM}(n, Z)]$ versus $\ln(Z)$ for $n = 1, 4, 16$ and 25 at the scaled electron-impact energy of $E_{sc} = 9.5$. On top of the data points we have plotted lines of the form $2\ln(Z) + C$ where C is constant for each n line and evaluated so that the last data point for each n is fixed on its respective line. Note that for $n = 1$ and 2 all the points lie on their lines whereas for the highest two ns the low Z substantially deviates from their respective lines. The fact that the slope of the lines is 2 means that for low n the ionization probability scales $\sim 1/Z^2$ and for high n it scales $\sim 1/Z^2$ only for the high Z.

4.3.5 Node structure near the scattering center

Looking at the classical trajectories that give rise to ionization, we can roughly estimate the size of the region where the energy exchange between the electrons takes place at the time of scattering from the core. To gain physical insight about the discrepancy

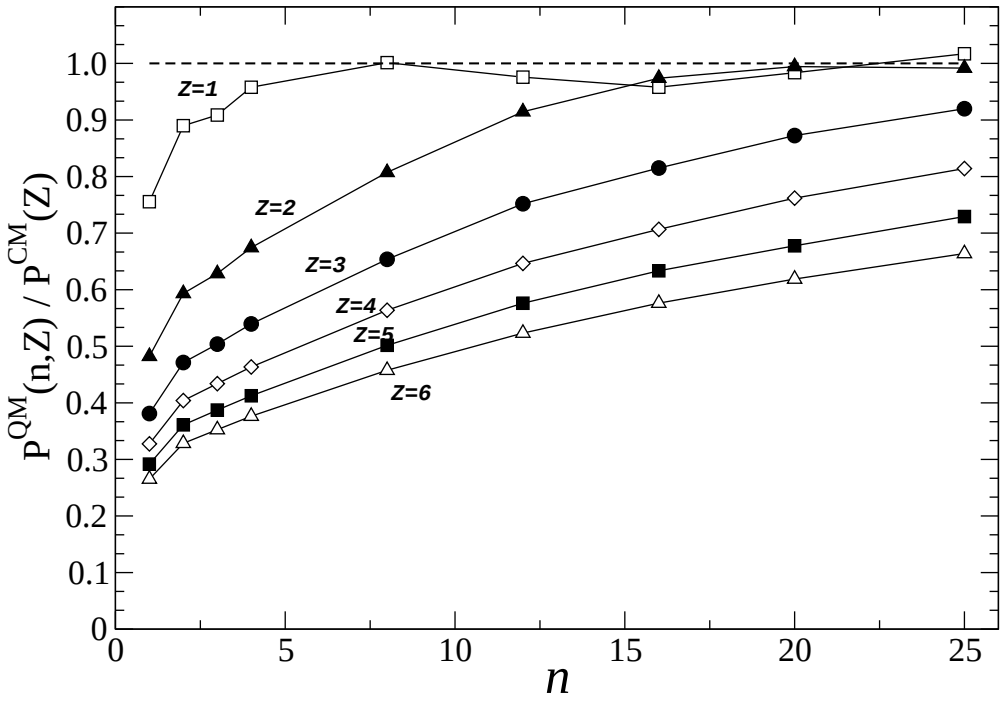

Figure 4.7: Ratio of the quantal and classical ionization probabilities, $P^{QM}(n,Z)/P^{CM}(Z)$, as a function of n for $Z = 1 - 6$.

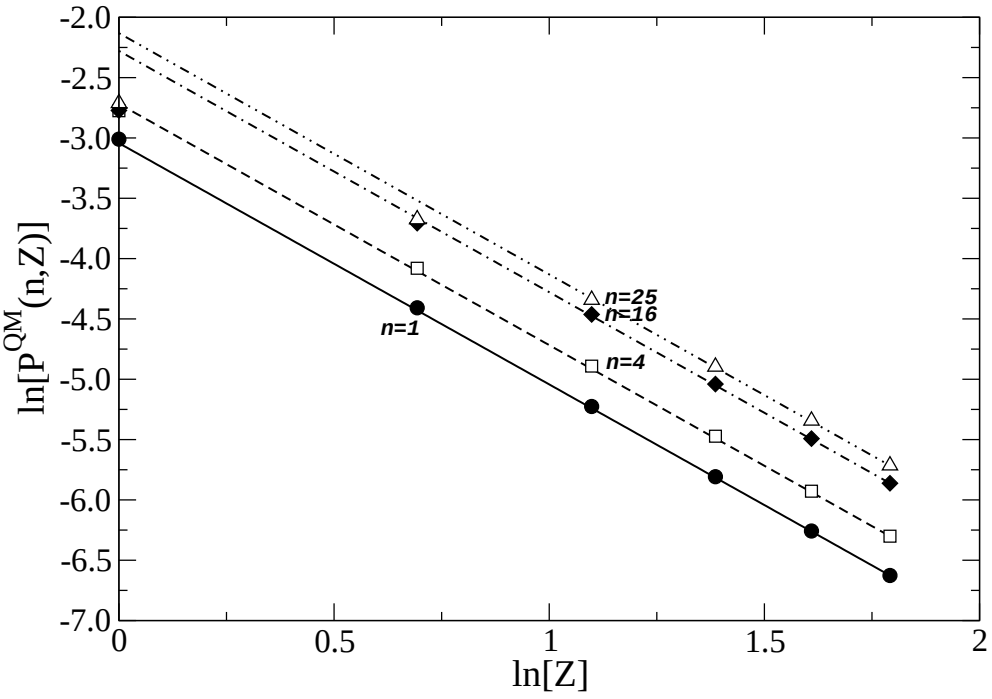

Figure 4.8: $\ln[P^{QM}(n,Z)]$ versus $\ln(Z)$ for various n at $E_{sc} = 9.5$. Note that the straight lines have a slope of 2 which implies $\sim 1/Z^2$ scaling of the ionization probability for $n = 1$ and 4 and for higher Z of $n = 16$ and 25.

between the classical and quantal results even for such high n, we may draw analogy to geometrical-wave optics correspondence. According to the geometrical-wave optics correspondence, light exhibits classical behavior when the wavelength is much smaller than the size of the region with which it interacts. In other words, we recover geometrical optics as the wave number gets larger within the interaction region. Applying the same idea to the matter waves, we can expect the system to behave more classically as the number of nodes increase in the region where classical energy exchange between the electrons takes place.

The classical size of the scattering region that give ionization is $\ell_c \sim 0.1$ in scaled units (which is $L_c = 2n^2\ell_c$) for $Z = 5$ when the scaled energy of the incoming electron is 9.5. Using the Z-scaled potential, this characteristic size can be shown to be $L_c = 51.2$ (a.u.) for $n = 16$. For the lowest energy component in the wave function, the kinetic energy is approximately equal to the Z-scaled potential energy, i.e. $k^2/2 \sim 1/r$, from which $k(r) \sim \sqrt{2/r}$. We can use half wavelength in this energy regime to obtain a typical length scale of the region where the scattering takes place from the core. Half wavelength corresponding to $k(r)$ is

$$\pi \sim \int_0^{L_q} k(r)dr = \sqrt{8L_q} \tag{4.22}$$

from which $L_q \sim \pi^2/8 \simeq 1.2$. Comparing this with the classical size of the scattering region yields an intriguing result since the size of the classical scattering region is about a factor of 43 larger than the quantal length scale; therefore one would expect the quantal results to be in good agreement with the classical result at $n = 16$.

In Fig. 4.9 we have plotted the absolute value square of the wave function for both $Z = 1$ (top panel) and $Z = 5$ (bottom panel) at $n = 16$ for scaled energy $E_{sc} = 9.5$. Various classical trajectories that give ionization are also plotted on top of each probability distribution. In these plots, we can define regions by using the points of the trajectories at which the coordinate of one electron vanishes, which we call bounce points. Note that for $Z = 1$, the number of nodes in the region bound by the last two bounces of the outmost classical trajectory is considerably larger than in the case of $Z = 5$. For $Z = 5$, Eq. (4.22) with $L_q \rightarrow L_c$ yields the number of nodes in the classical scattering region as $\sim \sqrt{8L_c}/\pi \sim 6$ which roughly equals the number of nodes in the bottom panel of Fig. 4.9 bounded by the last two bounces of the outmost classical trajectory.

4.4 Conclusions

We have performed collinear s-wave time-dependent close-coupling (TDCC), classical trajectory Monte Carlo (CTMC), and distorted-wave (DW) calculations for electron-impact ionization of H-like ions with $Z = 1 - 6$ for various principal quantum numbers up to $n = 25$. We have observed good agreement between the s-wave TDCC and the CTMC methods for hydrogen as the principal quantum number reached $n = 4$. The good agreement between the collinear s-wave TDCC and the classical results for hydrogen in the high-n limit is in accord with the expectations raised by the Bohr correspondence principle. Repeating the same set of calculations for B^{4+}, we have found that one has to go to much higher n for the collinear s-wave TDCC and the CTMC methods to agree. We showed that the TDCC results converge to the classical results very slowly with increasing n, which is

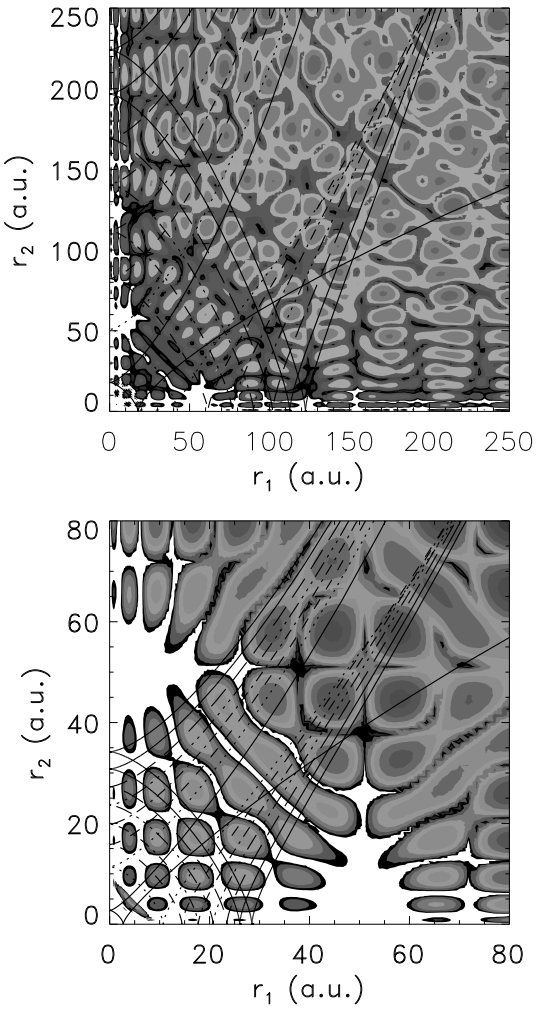

Figure 4.9: Contour plots for $|\psi_{n=16}(r_1, r_2)|^2$ for H (top panel) and B^{4+} (bottom panel) at the time of scattering from the nucleus at $E_{sc} = 9.5$. The lines in each figure represent classical trajectories that lead to ionization.

in agreement Griffin *et al.* [40] have observed in their full three dimensional calculations up to $n = 4$. At $n = 25$ and for the ^1S symmetry of the initial wave packet, the TDCC method yields ionization probability which is $\sim 35\%$ less than the classical result at the highest electron-impact energy we considered. For the same n and electron-impact energy, the TDCC result is about a factor of 2 less than the CTMC result for the ^3S case.

The collinear s-wave DW calculations for hydrogen resulted in cross sections which are in good agreement with the collinear s-wave TDCC calculations for the ground state, and gradually got worse as n is increased. In the case of B^{4+}, we have shown that the agreement between the DW and TDCC is excellent up to $n = 8$. This suggests that, for the low lying excited states, the DW is just as good as the exact TDCC method, which makes it useful for the plasma modeling and diagnosing purposes. One would expect a perturbative method to work when only a small fraction of the initial state ionizes, leaving most of the initial population in the initial state. The fact that the collinear s-wave DW method works so well even though it is perturbative may be due to the small interaction potential compared to the ionization energy. The energy difference between the adjacent states decreases as $\sim 1/n^3$ for high n and the incoming electron can knock the atom in a nearby n state instead of ionizing it. This is even more probable for the model potential we used, which is weaker than the actual $1/|\vec{r}_{12}|$ potential.

To illustrate the effect of the ion state Z on the ionization probabilities, we have carried out collinear s-wave TDCC calculations for Z up to 6 and for n up to 25 at the scaled electron-impact energy $E_{sc} = 9.5$. We found that for low-n the ionization probability scales like $\sim 1/Z^2$ and for high-n it behaves the same only for high Z.

In order to understand the physical size scales involved and gain some insight on the dynamics behind this slowly converging behavior, we drew analogy to geometrical-wave optics correspondence and estimated the number of nodes in the region near the core outlined by the classical trajectories that give ionization. We have found that the size of the classical scattering region is about a factor of 50 larger than the quantal length scale; therefore, one would expect the TDCC and CTMC methods to agree, which is not in accord with what we have observed. The peculiar dynamics behind this slow convergence is intriguing and may be due to an inherent characteristic of the line-land potential or a quantum interference effect.

CHAPTER 5

RADIATIVE CASCADE OF HIGHLY EXCITED HYDROGEN ATOMS IN STRONG MAGNETIC FIELDS

5.1 Introduction

In this chapter, we investigate the radiative cascade from the Rydberg states with energies effectively corresponding to hydrogenic n-manifolds of up to $n = 35$ in magnetic field strengths of up to 4.0 T. We have also followed the radiative cascade from these initial states in the presence of the black body radiation since the positron and anti-proton plasmas have a temperature of 4 K in case of the ATRAP experiment.

High-$|m|$ Rydberg atoms in the presence of strong magnetic fields were also investigated by Guest and Raithel [55]. They found that in case of the high-$|m|$ states in strong magnetic fields the motions that are parallel and transverse to the magnetic field are adiabatically separable. They studied the break down of the adiabaticity as they decreased $|m|$ from 200 to 40 and observed that the motion in states with $|m| \sim 200 - 80$ are adiabatically separable to the extent where no more than 50% of the energy levels are overtaken by the non-adiabatic couplings. As they decreased $|m|$ further down to $|m| \sim 40$ the energy spectrum experienced a transition from adiabaticity to non-adiabaticity. They have also calculated the natural and thermally enhanced decay rates for the states in which the motion is adiabaticaly separable [56]. In this paper we perform calculations for the $|m| \lesssim 40$ region which has not yet been treated.

In this study, we also exploit the fact that the size of the positron and anti-proton plasmas are small compared to the size of the trap. As a result, once an anti-hydrogen atom is formed, it quickly leaves the plasma and moves into the vacuum of the trap. If the anti-atom is trapped then it spends its time in this vacuum radiatively decaying without positron−anti-atom collisions. Therefore this study only considers radiative cascade in vacuum.

The radiative cascade from high Rydberg states exhibit interesting details. Reference [57] studied the phase space trajectory of an initial n, ℓ state cascading to the ground state in zero magnetic field. In principle, a similar treatment using the quantum numbers in the magnetic field could be performed but is beyond the scope of this study.

We also give a semiclassical treatment for the radiative cascade from the highly excited circular Rydberg states for the sake of physical transparency. We have shown that the population time for the ground state strongly depends on the fraction of circular high-$|m|$ states in the initial distribution. We considered the relative effect of the cyclotron motion with respect to the magnetron motion in circular high-$|m|$ states on the decay rates and draw conclusions on the affinity of these states to magnetic field gradients.

All our calculations are for regular hydrogen rather than anti-hydrogen but the results apply equally well to anti-hydrogen. In this study, atomic units are used throughout unless stated otherwise. The work presented in this chapter has been published as a paper in Physical Review A [58].

5.2 Theory

Our results are obtained using an approximate Hamiltonian of a hydrogen atom placed in a magnetic field,

$$H = \frac{(\vec{p} - \vec{A}/c)^2}{2} - \frac{1}{r} \tag{5.1}$$

where $\vec{A}$ is the vector potential. In the Appendix we discuss the limitations of this Hamiltonian and show that it serves our purposes. With the choice of symmetric gauge $\vec{A} = -\frac{1}{2}\vec{r}\times\vec{B}$ and a uniform magnetic field of magnitude B_0 along the z direction, i.e. $\vec{B} = B_0\hat{z}$, the Hamiltonian in spherical coordinates becomes,

$$H = H_{atom} + \frac{\gamma}{2}L_z + \frac{\gamma^2}{8}r^2\sin^2\theta \tag{5.2}$$

where H_{atom} is the atomic Hamiltonian in the absence of the magnetic field,

$$H_{atom} = \frac{p^2}{2} - \frac{1}{r} \tag{5.3}$$

and $\gamma = B_0/(2.35 \times 10^5\ \mathrm{T})$ is the magnetic field strength in atomic units when B_0 is in Tesla. Note that the total Hamiltonian H has rotational symmetry about the z axis like the unperturbed atomic Hamiltonian.

In the next subsection, we describe the method used to compute the eigenenergy spectrum of the hydrogen atom in the magnetic field where we diagonalize the total Hamiltonian H in the basis spanned by the eigenstates of the atomic Hamiltonian H_{atom}. In the second subsection, we evaluate the dipole matrix elements in the magnetic field by rotating the

dipole matrix elements calculated in the $\{n, \ell, m\}$ basis into the dipole matrix elements in the $\{m, \pi\}$ basis. The radiative decay rates in the magnetic field is then evaluated by using these rotated dipole matrix elements. In the last subsection, we solve the time dependent rate equation for an initial probability distribution of the eigenstates of H, which tells us how the initial probability distribution evolves in time.

5.2.1 Calculation of the Energy Spectrum in the Magnetic Field

To calculate the new energy spectrum in the magnetic field, we diagonalized the matrix representation of the full Hamiltonian H in the basis spanned by the eigenstates $\psi_{n\ell m}$ of the unperturbed atomic Hamiltonian. The matrix elements of the Hamiltonian $H = H_{atom} + H_{magnetic}$ in this basis are

$$\begin{aligned} < n\ell m|H|n'\ell'm' > &= \left[\epsilon_{n\ell} + \frac{\gamma}{2}m\right]\delta_{n,n'}\delta_{\ell,\ell'}\delta_{m,m'} \\ &\quad + \frac{\gamma^2}{8} < n\ell m|r^2\sin^2\theta|n'\ell'm' > \end{aligned} \tag{5.4}$$

where $\epsilon_{n\ell}$ are the eigenvalues of H_{atom}, i.e. energies of the hydrogen atom in the absence of the magnetic field. Noting that $\sin^2\theta = (2/3)[1 - \sqrt{4\pi/5}\, Y_2^0(\theta, \phi)]$, the angular part of the last integral in Eq.(5.4) can be evaluated as

$$\begin{aligned} < \ell m|\sin^2\theta|\ell'm' > &= \frac{2}{3}\delta_{\ell,\ell'}\delta_{m,m'} - \frac{2}{3}(-1)^m \\ &\quad \times \sqrt{(2\ell+1)(2\ell'+1)} \begin{pmatrix} \ell & 2 & \ell' \\ 0 & 0 & 0 \end{pmatrix} \begin{pmatrix} \ell & 2 & \ell' \\ -m & 0 & m' \end{pmatrix}. \end{aligned} \tag{5.5}$$

Selection rules for these matrix elements can be deduced from the fact that the 3-j symbols must satisfy the triangle relations (Ref. [62]) simultaneously in order to survive. For the 3-j symbols involved in Eq. (5.5) this condition is realized as $|\ell - \ell'| \leq 2$. Also the survival of the first 3-j symbol in the Eq. (5.5) requires that the sum of the elements on the first row must be an even integer. This condition along with $|\ell - \ell'| \leq 2$ implies that the magnetic field will only induce transitions for which $\Delta\ell = 0$ or $\Delta\ell = \pm 2$. Therefore with the definition

$$R^{n,\ell}_{n',\ell'}(\eta) = \int R_{n,\ell}(r) r^{\eta} R_{n',\ell'}(r) dr \tag{5.6}$$

where $R_{n,\ell}(r)$ is the radial part of the eigenfunction $\psi_{n\ell m}$, the matrix elements of the full Hamiltonian H in the $\{n\ell m\}$ basis become,

$$\begin{aligned} < n\ell m|H|n'\ell'm' > \;\; = \;\; & \left[\epsilon_{n\ell} + \frac{\gamma}{2} m\right] \delta_{n,n'} \delta_{\ell,\ell'} \delta_{m,m'} \\ & + \frac{\gamma^2}{12} \Bigg[\delta_{m,m'} \delta_{\ell,\ell'} - (-1)^m \sqrt{(2\ell+1)(2\ell'+1)} \\ & \times \begin{pmatrix} \ell & 2 & \ell' \\ 0 & 0 & 0 \end{pmatrix} \begin{pmatrix} \ell & 2 & \ell' \\ -m & 0 & m' \end{pmatrix} \Bigg] R^{n,\ell}_{n',\ell'}(2). \end{aligned} \tag{5.7}$$

Here $R_{n,\ell}(r)$ is generated on a square root mesh by direct integration of the Schrödinger Equation in a box. All orbitals satisfy the boundary condition such that $R_{n,\ell}(r_f) = 0$ where the box size r_f is chosen to be larger than the size of the physical states in our simulations. By choosing this boundary condition, we greatly increase the rate of convergence with n

because eigenenergies $\epsilon_{n\ell}$ increase rapidly with n for large n [59]. Thus our basis has substantial continuum character.

We have checked the convergence of our results with respect to the box size r_f, the number of radial grid points N and the n_{max} and ℓ_{max} describing the basis set used in the diagonalization of H. For example, in a 4.0 T field, decay times obtained for $n = 30$ in a 2000 (a.u.) box with 8000 radial points using a basis with $(n_{max}, \ell_{max}) = (45, 40)$ differ from the decay times obtained in a 3000 (a.u.) box with 12000 points using a basis described by $(n_{max}, \ell_{max}) = (50, 45)$ at a few percent level. The energy of the state $(n_{max}, 0)$ in the 2000 (a.u.) box is $\epsilon_{45,0} = 4.1138 \times 10^{-4}$ (a.u.) and the energy of the state $(30, 0)$ is $\epsilon_{30,0} = -5.5526 \times 10^{-4}$ (a.u.). For the 3000 (a.u.) box the state with $(n_{max}, 0)$ has the energy $\epsilon_{50,0} = 3.8628 \times 10^{-5}$ (a.u.) whereas energy of the state $(30, 0)$ is the exact value -5.5556×10^{-4} (a.u.).

Diagonalization of the matrix with the matrix elements given by Eq. (5.7) gives the new energy spectrum $\{\tilde{\epsilon}_j\}$ of the hydrogen atom in the magnetic field. Note that in the presence of the magnetic field the good quantum numbers are the magnetic quantum number m and the z-parity π rather than the principal quantum number n and the orbital quantum number ℓ.

As a check on our codes, we have compared our energies for hydrogenic $n = 23$ manifold in a 4.7 T field for states with $m = 0, 1, 2$ listed in Ref. [60] and found very good agreement except at a few particular energy values. The difference might be due to the fact that usage of non-orthogonal basis set methods, like the one used in Ref. [60], can be unstable, e.g. their energies may not be converged for those particular states.

5.2.2 Calculation of the Dipole Matrix Elements

To calculate the dipole matrix elements in the magnetic field, we first calculated the dipole matrix elements in the $\{n\ell m\}$ basis and rotated those matrix elements obtaining the dipole matrix elements in the $\{m\pi\}$ basis of the full Hamiltonian H.

Dipole matrix elements for the linearly polarized states in the $\{n\ell m\}$ basis are

$$< n\ell m|z|n'\ell' m' >=< n\ell|r|n'\ell' >< \ell m|\cos\theta|\ell' m' > . \tag{5.8}$$

Again noting that $\cos\theta = \sqrt{4\pi/3}\; Y_1^0(\theta,\phi)$ one can deduce

$$\begin{aligned} < n\ell m|z|n'\ell' m' > \;&=\; (-1)^m\sqrt{(2\ell+1)(2\ell'+1)} \\ &\times \begin{pmatrix} \ell & 1 & \ell' \\ 0 & 0 & 0 \end{pmatrix} \begin{pmatrix} \ell & 1 & \ell' \\ -m & 0 & m' \end{pmatrix} R^{n,\ell}_{n',\ell'}(1). \end{aligned} \tag{5.9}$$

In the same manner, for the left and right hand circularly polarized states one obtains

$$\begin{aligned} < n\ell m|\frac{x \pm iy}{\sqrt{2}}|n'\ell' m' > \;&=\; \mp(-1)^m\sqrt{(2\ell+1)(2\ell'+1)} \\ &\times \begin{pmatrix} \ell & 1 & \ell' \\ 0 & 0 & 0 \end{pmatrix} \begin{pmatrix} \ell & 1 & \ell' \\ -m & \pm 1 & m' \end{pmatrix} R^{n,\ell}_{n',\ell'}(1). \end{aligned} \tag{5.10}$$

respectively. Selection rules for the magnetic field induced transitions can be deduced from the properties of the 3-j symbols in Eqs.(5.9) and (5.10) as before. Since the second row of the second 3-j symbols in both of the expressions need to add up to zero for the survival of

the term, we can immediately conclude that there is no m change for the linearly polarized states while the circularly polarized states change m by 1. Also the first 3-j symbols in the terms tell us that $|\ell - \ell'| \leq 1$ and $|\ell + \ell'|$ must be an odd integer implying that ℓ must change by one for the term to survive. Since $\ell_{min} = m + \pi$ and ℓ increases from ℓ_{min} to $n - 1$ in integer steps for a given m it can be concluded that $|\Delta m| + |\Delta \pi| = 1$ for an allowed transition.

To obtain the dipole matrix elements in $\{m\pi\}$ space, we will simply rotate the matrix elements in Eqs.(5.9) and (5.10) computed in the $\{n\ell m\}$ basis. Let us index the state $(n\ell m)$ by j and the state $(m\pi)$ by α. Denoting the new rotated dipole matrix element by $d_{\alpha,\alpha'}$ we have

$$d_{\alpha,\alpha'} = \sum_{j} \sum_{j'} < \psi_j | d \, | \psi_{j'} > U^*_{j,\alpha} U_{j',\alpha'} \tag{5.11}$$

where d is the dipole operator which is z for linearly polarized states and $(x \pm iy)/\sqrt{2}$ for the left and right hand circularly polarized states respectively. The rotation matrix $\mathbb{U}$ is the matrix whose columns are the eigenvectors of the full Hamiltonian H in the $\{n\ell m\}$ basis which is obtained by direct diagonalization of H,

$$\sum_{j} H_{kj} U_{j\alpha} = U_{k\alpha} \tilde{\epsilon}_{\alpha} \tag{5.12}$$

where $\tilde{\epsilon}_{\alpha}$ is the αth eigenenergy of the Hamiltonian H with the eigenstate U_{α}.

Having obtained the dipole matrix elements we now can calculate the partial decay rates of the states of the hydrogen atom in the magnetic field. Partial decay rate from initial

state i to final state f in length gauge is given by

$$\Gamma_{fi} = \frac{4}{3c^3}(\tilde{\epsilon}_i - \tilde{\epsilon}_f)^3| < \tilde{\psi}_f|\vec{r}\,|\tilde{\psi}_i > |^2 \tag{5.13}$$

where $\tilde{\epsilon}_\alpha$ and $\tilde{\psi}_\alpha$ are the energy and the eigenfunction of state α of the hydrogen atom in the magnetic field and $4/(3c^3) = 5.181 \times 10^{-7}$ in atomic units. Note that the usual velocity gauge expression derived in the absence of a magnetic field becomes

$$\Gamma_{fi} = \frac{4}{3c^3}(\tilde{\epsilon}_i - \tilde{\epsilon}_f)| < \tilde{\psi}_f|\vec{p} - \vec{A}/c\,|\tilde{\psi}_i > |^2 \tag{5.14}$$

with the inclusion of the magnetic field because the physical momentum of the electron is now $(\vec{p} - \vec{A}/c)$ as being different from the canonical momentum $\vec{p}$ of the electron.

5.2.3 Solution of the Rate Equation

Having obtained the partial decay rates $\Gamma_{\alpha,\alpha'}$ in the magnetic field, we solved the time dependent rate equation to simulate the flow of initial probability distribution among the states. The rate equation for the probability $\wp_\alpha$ of finding the atom in state α is

$$\frac{d\wp_\alpha}{dt} = -\Gamma_\alpha \wp_\alpha + \sum_{\alpha' > \alpha} \Gamma_{\alpha\alpha'} \wp_{\alpha'} \tag{5.15}$$

where Γ_α is the total decay rate of state α,

$$\Gamma_\alpha = \sum_{\alpha' < \alpha} \Gamma_{\alpha'\alpha}. \tag{5.16}$$

Note that the condition $\alpha > \alpha'$ implies the constraint $\tilde{\epsilon}_{\alpha'} < \tilde{\epsilon}_{\alpha}$. The first term on the right hand side of the rate equation represents the total flow of probability out of the state α while the sum in the second term is due to the total flow of probability into state α from all higher states α'. The $\Gamma_{\alpha,\alpha'}$s span several orders of magnitude making Eq. (5.15) difficult to solve. Assume the solution to be of the form $\wp_\alpha = \wp_\alpha^{(0)} + \wp_\alpha^{(1)}$ where $\wp_\alpha^{(0)}$ satisfies

$$\frac{d\wp_\alpha^{(0)}}{dt} = -\Gamma_\alpha \wp_\alpha^{(0)}. \tag{5.17}$$

The time propagation of this equation by one time step δt for a given $\wp_\alpha^{(0)}$ at a time t is

$$\wp_\alpha^{(0)}(t+\delta t) = e^{-\Gamma_\alpha \delta t}\wp_\alpha(t). \tag{5.18}$$

Substituting $\wp_\alpha = \wp_\alpha^{(0)} + \wp_\alpha^{(1)}$ into the rate equation and noting that $\sum_\alpha \wp_\alpha(0) = \sum_\alpha \wp_\alpha^{(0)}(0) = 1$, one obtains,

$$\wp_\alpha^{(1)}(t+\delta t) = \sum_{\alpha'>\alpha} B_{\alpha\alpha'}(1 - e^{-\Gamma_{\alpha'}\delta t})\wp_{\alpha'}(t). \tag{5.19}$$

where $B_{\alpha\alpha'} \equiv \Gamma_{\alpha\alpha'}/\Gamma_{\alpha'}$ is the branching ratio. Combining Eq.(5.18) and Eq.(5.19) $\wp_\alpha$ becomes,

$$\wp_\alpha(t+\delta t) = e^{-\Gamma_\alpha \delta t}\wp_\alpha(t) + \sum_{\alpha'>\alpha} B_{\alpha\alpha'}(1 - e^{-\Gamma_{\alpha'}\delta t})\wp_{\alpha'}(t). \tag{5.20}$$

For an initial distribution of probability among the states one can propagate the probability distribution along time with the knowledge of the decay rates. We have checked the convergence of our results with respect to the maximum effective cut off quantum numbers n_c, ℓ_c of the basis states used to describe the radiative decay from a given initial distribution. The

states that make up this initial distribution have effective quantum numbers that are smaller than these cut off n_c, ℓ_c quantum numbers. Convergence with respect to the time step δt was also checked.

5.3 Results

We will start by making some rough estimates for the effect of the magnetic field on the classical velocity of the electron in a circular orbit to obtain an idea of the extent to which the decay rates from these states change from their field free estimates. The second subsection contains results from calculations for the radiative cascade in 1.0 T, 2.0 T, 3.0 T and 4.0 T fields where the initial distribution of states with energies corresponding to various principal quantum numbers up to $n = 35$ are completely ℓ, m mixed. These results are compared with some results obtained using an analytical rate formula. In the following subsection we present results from calculations for which the initial states are localized in the highest $|m|$ regions of an n manifold and again some results obtained using an analytical formula for the decay rates. The effect of the black body radiation will be taken into account to see if the results of the previously presented radiative cascade calculations are affected by a 4 K [5, 6] radiation field. Finally we present a semiclassical treatment for the calculation of the radiative decay rates of circular orbits and compare them to those calculated quantum mechanically.

5.3.1 Rough Estimates

For a classical electron in a closed circular orbit in a Coulomb field, Newton's laws give

$$m_e \frac{v_0^2}{r} = k\frac{e^2}{r^2} \tag{5.21}$$

where we have employed the SI units. Solution of this equation for the classical velocity immediately yields $v_0 = \pm\sqrt{ke^2/m_e r}$. In the presence of a uniform magnetic field of strength B_0 directed perpendicular to the plane of the circular orbit, Eq. (5.21) becomes

$$m_e \frac{v^2}{r} = k\frac{e^2}{r^2} + evB_0 \tag{5.22}$$

whose direct solution for v now yields

$$v = \frac{eB_0 r}{2m_e} \pm \sqrt{\Big(\frac{eB_0 r}{2m_e}\Big)^2 + v_0^2}. \tag{5.23}$$

Note that the $\pm$ sign in front of the square root term in Eq. (5.23) implies the fact that electron either speeds up or slows down depending on the sign of L_z of the orbit for a given direction of the magnetic field. Expanding the square root to the 4th order in binomial series for the case $eB_0 r/(2m_e) < v_0$, one approximates the classical velocity in magnetic field v by

$$v \approx \frac{eB_0 r}{2m_e} \pm \left[v_0 + \frac{1}{2v_0}\Big(\frac{eB_0 r}{2m_e}\Big)^2 + \frac{1}{8v_0^3}\Big(\frac{eB_0 r}{2m_e}\Big)^4\right]. \tag{5.24}$$

Noting that $k = m_e = e = 1$ in atomic units and $r \sim n^2$ for a circular classical orbit with energy $\epsilon \sim -1/(2n^2)$, we can infer

$$v_n^{cl} \approx \pm\frac{1}{n}\left[1 \mp \frac{\gamma n^3}{2} + \frac{1}{8}(\gamma n^3)^2 + \frac{1}{128}(\gamma n^3)^4\right] \tag{5.25}$$

where we have recalled that $\gamma = B_0/(2.35 \times 10^5 \text{ Tesla})$ is the magnetic field in atomic units when B_0 is in Tesla.

In the field free case, Eq. (5.25) predicts $v_n^{cl} \approx 1/n$ for all n which is exactly the quantum mechanical velocity $v_n = 1/n$. For $n = 10$, the zero field velocity differs from the $B_0 = 4.0$ T value by $\sim 1\%$. At $n = 20$ the difference between the velocities for 2.0 T field and the zero field is $\sim 3\%$ and $\sim 7\%$ at 4.0 T. When we are up to $n = 30$, v_n^{cl} differs from zero field value by $\sim 12\%$ for $B_0 = 2.0$ T, by $\sim 19\%$ for $B_0 = 3.0$ T and by $\sim 26\%$ for $B_0 = 4.0$ T. This suggests that magnetic field strengths of interest in the anti-hydrogen experiments has little effect on the circular orbits with $n < 10$ while starting to effect the velocities in the orbits with $n \sim 20$ within $\sim 10\%$ and in the orbits with $n \sim 30$ within $\sim 30\%$. Noting that the radiative decay rate scales like $a^2 \sim v^4/r^2$, we can infer that the magnetic field affects the decay rates more strongly than it affects the velocity of the electron in the orbit.

In the limit where $eB_0r/2m_e \gg v_0$ Eq. (5.23) can be expanded to 2nd order as

$$v_n^{cl} \approx \frac{eB_0r}{2m_e} \pm \frac{eB_0r}{2m_e}\left(1 + \frac{v_0^2}{2(eB_0r/2m_e)^2}\right) \tag{5.26}$$

yielding $v_+^{cl} \approx eB_0 r/m_e + v_0^2/(eB_0 r/m_e)$ for the orbit in which the electron is sped up, and $v_-^{cl} \approx -v_0^2/(eB_0 r/m_e)$ for the orbit in which the electron is slowed down by the magnetic field. The case where the electron is slowed down corresponds to the guiding center approximation since the Larmor period is much smaller than the orbital period of the electron. In 4.0 T field, the absolute value of the ratio of the velocities in orbits with same energy but of opposite helicities, i.e. $|v_+^{cl}/v_-^{cl}|$, is ≈ 1.0 for orbits with n up to 25, ~ 1.2 at $n = 30$ and ~ 2.2 at $n = 40$.

5.3.2 Energy Spectrum in the Magnetic Field

From the diagonalization of the full Hamiltonian H, we have found that the energies of the states with negative magnetic quantum numbers decrease whereas the energies of the states with positive magnetic quantum numbers increase with the increasing magnetic field strength. In the anti-hydrogen experiments, magnetic field will be deliberately generated in such a way that it is stronger near the walls of the cylindrical container in which anti-proton and positron plasmas are mixed. Therefore the states with negative m's are attracted by the increasing magnetic field strength and states with positive m's are repelled by the increasing magnetic field. Hence we can expect the states with negative m that are close to the magnetic field gradient to plummet to the wall of the container faster than those with positive m. Therefore atoms that are formed with high field seeking character will need to decay especially rapidly if they are not to be accelerated by the magnetic field gradients. For extremely negative $m \sim -200$ of [56], the atoms could have low field seeking character because the positive magnetic moment from the electron's cyclotron motion is larger in

magnitude than the negative magnetic moment from the guiding center character of the electron's motion around the proton.

5.3.3 Radiative Cascade Starting from Completely Random (ℓ, m) Distribution

Since n is not a good quantum number when magnetic field is present, the initial probability distribution was chosen such that the probability of finding the atom in a state whose energy is between energies of hydrogenic n and $n-1$ manifolds is equally partitioned between the states that lay in this energy range. Initial distributions that correspond to $n = 10, 15, 20, 25, 30$ and 35 in magnetic fields of strengths 1.0 T, 2.0 T, 3.0 T and 4.0 T have been explored. Furthermore, instead of monitoring the flow of probability of finding the atom within a particular state, we have monitored the probability of finding the atom in a state whose energy lies in a range which embraces 5-10 n manifolds. Evolution of the probability distribution with time when started out in states with effective $n = 35$ in a 4.0 T field are plotted in Fig. 5.1. As time progresses states of lower energies become populated, eventually with all population ending up in the ground state. At early times the fast decay is mostly coming from the low-$|m|$ states which cascade by large Δn steps. The slow decay at later times is due to the states with large-$|m|$ which cascade through $\Delta n \sim -1$ transitions.

In the anti-hydrogen experiments, the formed anti-hydrogen atoms move through a magnetic field that is spatially dependent, e.g. stronger near the walls of the cylindrical container. Since the magnetic force on the center of mass of the anti-hydrogen atom depends on its internal energy, it is important to know the time scale for the variation of the internal

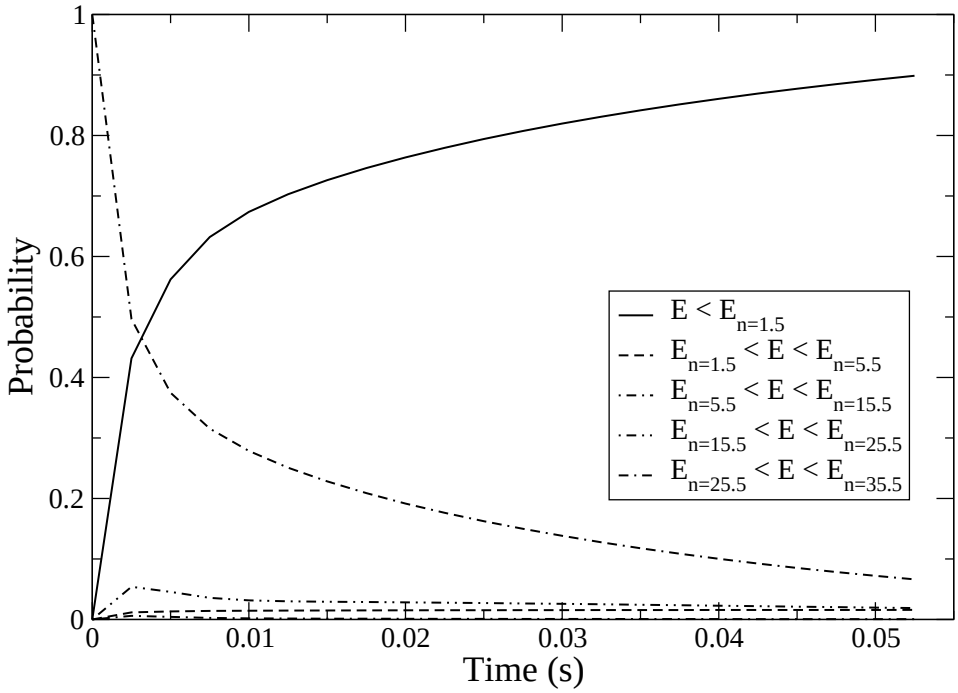

Figure 5.1: Flow of probability in the completely ℓ, m mixed distribution for $n = 35$ in a 4.0 T field as a function of time. Each curve represents the total probability of finding the atom in a state whose energy is in one of the particular energy ranges indicated on the legend.

energy of the anti-hydrogen atom to estimate the time it has before colliding with the wall of the container and get annihilated. A practical percentage of the anti-atoms should decay to the ground state before they get destroyed to be used in the CPT and Lorentz violation experiments. Therefore we have calculated the time it would take to populate the ground state by 10%, 20%, 50% and 90% if everything starts from states that are in aforementioned n regimes. In Figs. 5.2(a) and (b) the time it takes 10% and 50% of the hydrogen atoms to decay down to the ground state as a function of the given initial state n is plotted for four different magnetic field strengths. It can be seen that for $n \lesssim 25$ the magnetic field makes no important difference in terms of populating the ground state by 10% and when we are up to $n = 35$ we see ~ 0.4 ms separation between 1.0 T and 4.0 T values. This implies that the increase in the time it takes to populate the ground state by n is mainly a zero field effect. When we look at the 50% population plot it can be noted that for $n \lesssim 25$ there is no change coming from increasing the field strength but by $n = 30$ there is ~ 0.8 ms and by $n = 35$ there is ~ 3.5 ms separation between the lowest and highest magnetic field strengths.

The thermal speed, $\sqrt{k_B T/M}$, of an anti-hydrogen atom at 4 K [5, 6] is ~ 260 m/s which is ~ 26 cm/ms and higher by a factor of 2 at 16 K [4]. Noting that the diameter of the cylindrical container is approximately a couple of centimeters, we can conclude that in the field regime of the experiments there is not enough time to populate the ground state by even 50% before the anti-hydrogen atoms hit the walls and get destroyed. According to Fig. 5.2(a), for $n = 35$ the time needed to populate the ground state by 10% is about 0.2 ms in which the thermal anti-hydrogen atoms can move ~ 6 cm. Hence we can conclude

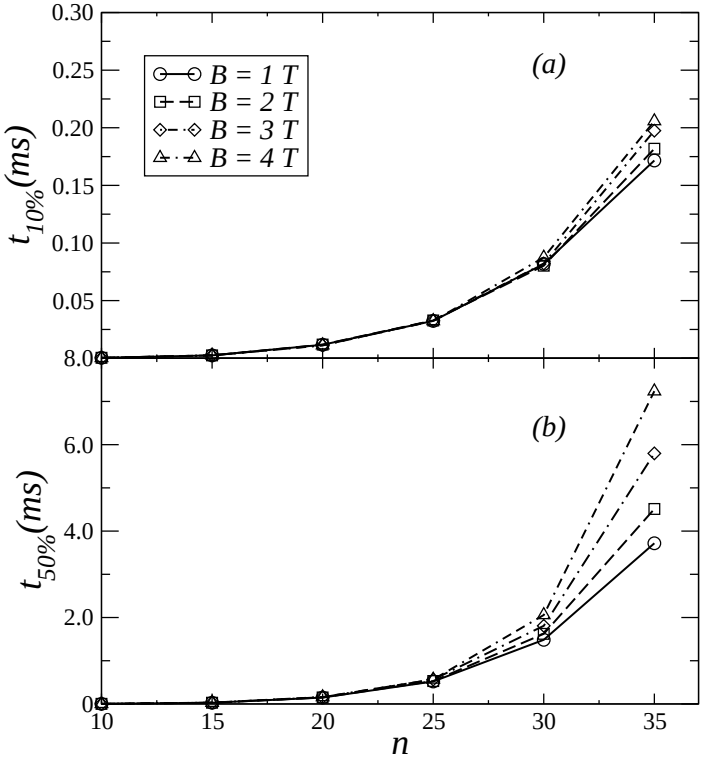

Figure 5.2: Time required to populate the ground state of the hydrogen atom by (a) 10% and (b) 50% as a function of the effective hydrogenic principal quantum number n for 1.0 T, 2.0 T, 3.0 T and 4.0 T fields. Initial distribution of states is completely ℓ, m mixed.

that at 4 K and in magnetic fields up to ~ 4 T the ground state population will not be able to exceed 10%. Since ATHENA experiment runs at a higher temperature, this population percentage would be even lower in their experiment. It seems clear that in order to trap substantial amounts of anti-hydrogen, the anti-atoms need to be trapped while in Rydberg states.

Since the lifetime of the completely ℓ, m mixed case increases $\sim n^5$ for a highly excited hydrogenic state in the absence of a magnetic field, time scaled by n^5 would stay roughly constant as n increases. Therefore we scaled our results for the decay times by n^5 to see the n range for which decay times are practically unaffected by the magnetic field. These scaled plots can be seen in Fig. 5.3 where we have plotted scaled time needed for the ground state to be populated by 10%, 50% and 90% versus initial n. In all the plots scaled time stays approximately constant up until $n \sim 25$ meaning that decay rates of these states are not affected by the magnetic field compared to the field free case; this is due to the fast direct decay to low n-states. Scaled time then starts to spread out noticeably with growing n there on. The states with higher-$|m|$ decay more slowly and have rates that are more strongly affected by the magnetic field. This is the reason for the larger magnetic field effect in Figs. 5.3(b) and (c) than in Fig. 5.3(a).

For comparison, we have also done the same calculations for zero field case using decay rates calculated via an analytical formula which assumes complete ℓ mixing of the states populated in the initial distribution when there is no magnetic field [62]. In the actual decay process, states with low-$|m|$ can make bigger Δn jumps towards the ground state than the ones with high-$|m|$, resulting in the pile up of population in states with $|m| \sim n$

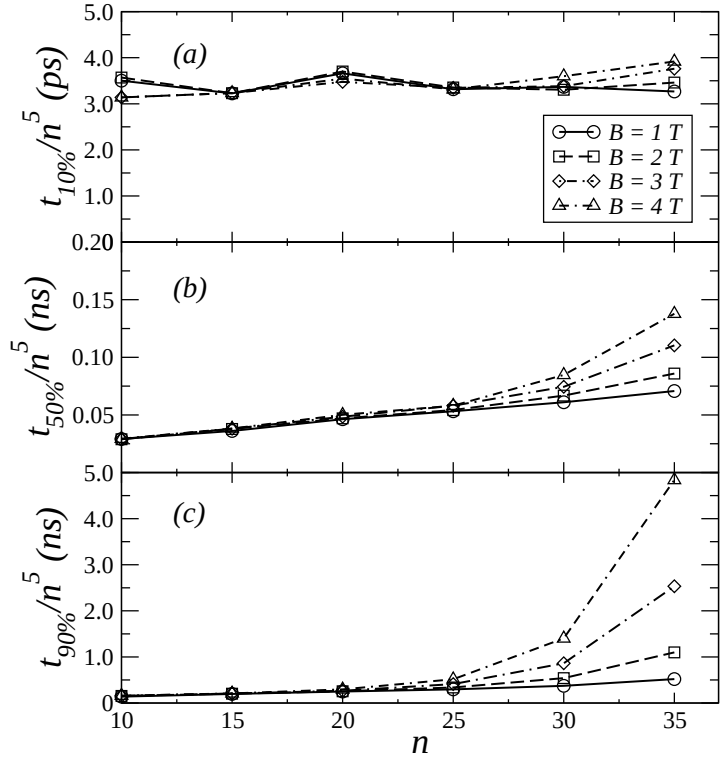

Figure 5.3: Scaled time required to populate the ground state of the hydrogen atom by (a) 10%, (b) 50% and (c) 90% as a function of the effective hydrogenic principal quantum number n for 1.0 T, 2.0 T, 3.0 T and 4.0 T fields. Initial distribution of states is completely ℓ, m mixed.

over time. Since the analytical formula assumes complete ℓ mixing within individual n-manifolds, it does not simulate the actual behavior after the piling up of population in high-m states. Therefore the applicability of this analytical formula is limited to short time periods from the beginning. In this picture, partial decay rate from state n_i to state n_f goes like

$$\Gamma_{n_i \to n_f} = \frac{8\alpha^3}{3\sqrt{3}\pi} \frac{1}{n_i^5 n_f} \frac{1}{1 - (n_f^2/n_i^2)} \tag{5.27}$$

where α is the fine structure constant. The total decay rate is again calculated as usual,

$$\Gamma_{n_i} = \sum_{n_f=1}^{n_i-1} \Gamma_{n_i \to n_f}. \tag{5.28}$$

For $n = 20$, time needed for population of the ground state to reach 10% is calculated using the rates from Eq. (5.27) is about 27% bigger than our quantal result while 90% population result is off by about 60%. Going up to $n = 30$ we found that time for 10% population of the ground state is longer by $\sim 14\%$ and 90% population time is longer by $\sim 76\%$ than our quantum mechanical result.

5.3.4 Radiative Cascade Starting from High-$|m|$ Distribution

The dominant process in the anti-hydrogen formation is believed to be three body recombination. It is also known that the atoms formed in this process are likely to be in a high m state [12]. This is clearly a different situation than the completely ℓ, m mixed case where every state within a prescribed energy range is equally likely to be populated. To simulate the case of the three body recombination we restricted our initial states not just

being in the $[\epsilon_{n-1}, \epsilon_n]$ energy range but also their m values to be extreme to qualify as one of the initial states. We investigated both extreme cases in which $m \sim n$ and $m \sim -n$ although it seems that the $m \sim -n$ case is more likely. High-$|m|$ states are chosen such that there are only a few states that make up the initial distribution.

For comparison, we also calculated the time it takes the atom to reach to its ground state in zero magnetic field by an approximate formula for the decay of circular states:

$$\Gamma_{n\to(n-1)} = \frac{2}{3(n-\frac{1}{2})^2 n^3 c^3}. \tag{5.29}$$

The decay rate estimates we made using Eq. (5.29) for zero magnetic field are in agreement with the exact quantum results within about 5% for the states with $n = 2$ and get better with increasing n reaching agreement with the quantal result within 0.5% by $n = 5$ for $B = 0$.

The results of the quantum mechanical calculations for 10% population of the ground state are plotted in Fig. 5.4 for magnetic field strengths of 1.0 T and 4.0 T for highest and lowest m states in their respective n manifolds with the zero field results for comparison. Both 1.0 T and 4.0 T curves for high m lie just below the zero field results throughout the whole n range from 10 to 30, while for the states with lowest m's 1.0 T field lifts the 10% population time just above the zero field curve and 4.0 T field stretches the required time for 10% population of the ground state from the zero field value by a factor of ~ 13 for $n = 30$. Note that the largest effect is for the states with $m \sim -n$, only becoming important above $n \sim 25$. The fact that the 4.0 T field has a more pronounced effect for the $|m| \sim -n$

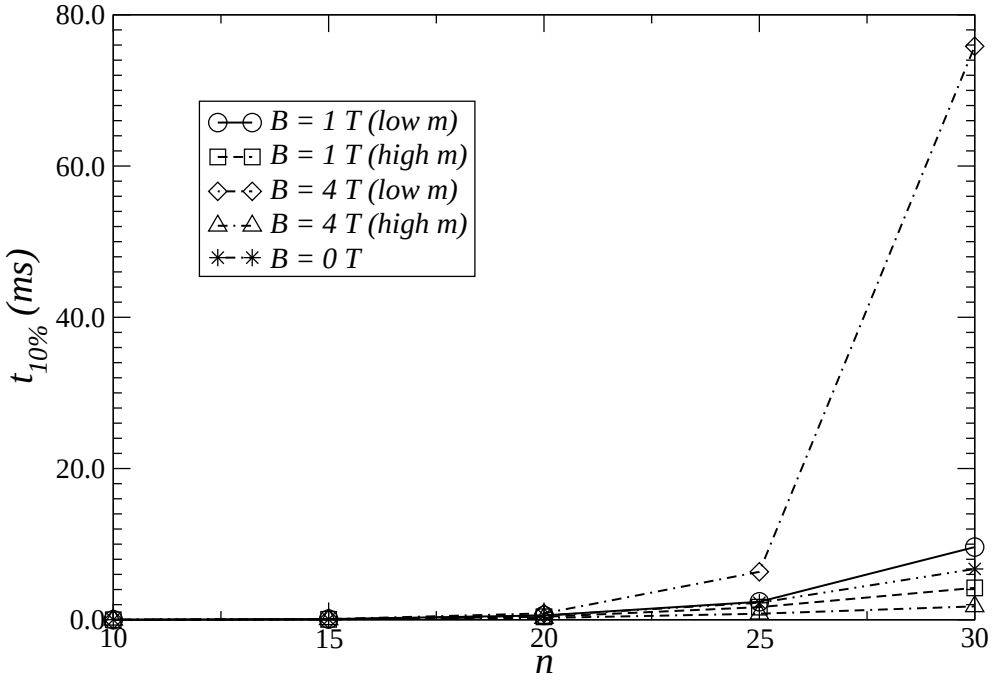

Figure 5.4: Time required to populate the ground state of the hydrogen atom by 10% as a function of the effective hydrogenic principal quantum number n for 1.0 T and 4.0 T fields. Initial distribution of states only involves states with high $|m|$.

mixed distribution than for the completely ℓ, m mixed distribution is because now the states in the distribution are mostly circular and most of the transitions are of $\Delta n = -1$ type.

In Fig. 5.5, the times required for the population of the ground state by 10%, 50% and 90% are scaled by n^6 since now initial distribution involves only circular states. Scaled decay times are plotted versus n for the high-$|m|$ states again in magnetic fields of strengths 1.0 T and 4.0 T. In all three plots, both of the $m \sim n$ cases lie just below the zero field

curve. For the states with $m \sim -n$, 1.0 T field cannot alter the scaled time of 10% population by more than $\sim 30\%$ from the field free case but for the 4.0 T field scaled population time is larger than zero field case by a factor of ~ 2.5 at $n = 25$ and by a factor of ~ 11 by $n = 30$. Again starting from the states with $m \sim -n$, 50% population of the ground state in 1.0 T field does not differ from the field free value by more than $\sim 25\%$ but for the 4.0 T field scaled population time is larger than zero field case by a factor of ~ 3 at $n = 25$ and by a factor of ~ 11 by $n = 30$. For the 90% population of the ground state, 1.0 T field again does not do a good job in lifting the scaled time by $n \sim 25$ from the zero field value and the 4.0 T field is again gives higher scaled time than zero field by a factor of ~ 2.5 at $n = 25$ and by a factor of ~ 15 at $n = 30$. The fact that the decay time for the negative m-states is much longer than the positive m-states can be understood from classical arguments. The classical radiation is proportional to the square of the acceleration of the electron which goes $\sim v^2/r$. Since the electrons in states with $m \sim -n$ are slowed down by the magnetic field, they have lower acceleration than the electrons in states with $m \sim n$. Therefore the electrons in states with $m \sim -n$ radiate less intensely and decay more slowly compared to the electrons in states with $m \sim n$.

5.3.5 Effect of Black Body Radiation

One concern was whether the experimentally reported black body temperatures of 16 K [4] and 4 K [5, 6] could strongly affect the radiative decay rates. The effect would be stimulated emission and photoabsorption fueled by the black body radiation. Expressing the decay rates in terms of Einstein A and B coefficients, the rate of radiative decay from

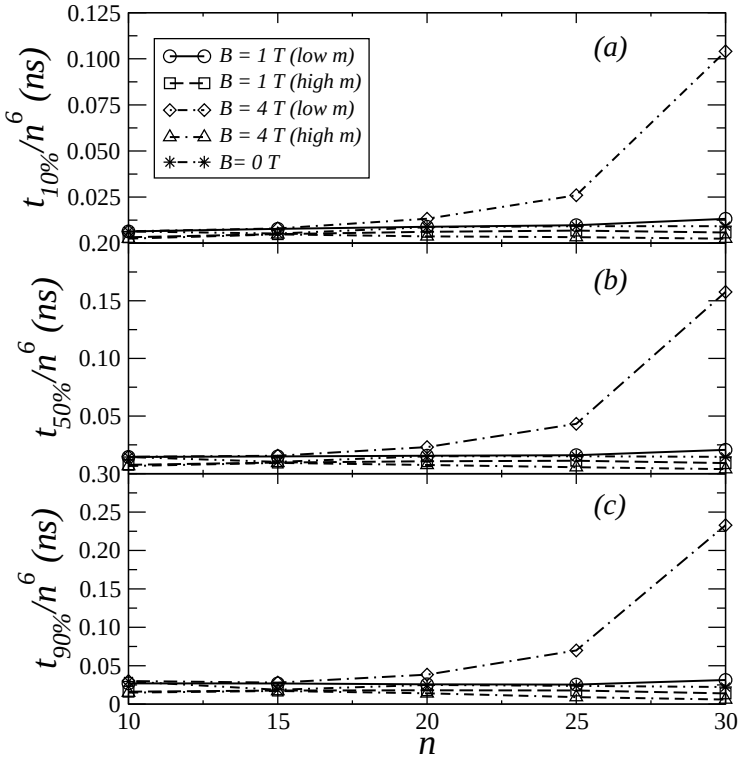

Figure 5.5: Scaled time required to populate the ground state of the hydrogen atom by (a) 10%, (b) 50% and (c) 90% as a function of the effective hydrogenic principal quantum number n for 1.0 T and 4.0 T fields. Initial distribution of states only involves states with $|m| \sim n$.

state i to state f would be

$$A_{i\to f} + B_{i\to f} u(\nu_{if}) \tag{5.30}$$

where $u(\nu_{if})$ is the Planck distribution

$$u(\nu_{if}) = \frac{\hbar\omega^3}{\pi^2 c^3} \frac{1}{e^{h\nu_{if}/k_B T} - 1}. \tag{5.31}$$

Einstein $B_{i\to f}$ coefficient is evaluated from the $A_{i\to f}$ coefficient in the following manner.

$$B_{i\to f} = \frac{\pi^2 c^3}{\hbar\omega^3} A_{i\to f} \tag{5.32}$$

In terms of evaluating the effect of the black body radiation, an important quantity is the ratio of the stimulated emission rate to the spontaneous emission rate, $(e^{h\nu_{if}/k_B T} - 1)^{-1}$. At 4 K, the $n \to (n-1)$ transitions up to about $n = 20$ the ratio is of the order of 10^{-6} and jumps up to about 5×10^{-2} at $n = 30$ and becomes ~ 0.4 at $n = 40$. Substantial contribution to this ratio comes from the transitions between the lowest energy states of different m manifolds. To see the effect of the black body radiation on the decay times, we used the rate in Eq. (5.30) and found that the time needed to populate the ground state changed by less than 10% for $n < 40$. We conclude that the black body radiation will not qualitatively affect the radiative cascade for $n < 40$.

5.3.6 Semiclassical Treatment

The time averaged classical power over one orbit emitted from an electron in a circular orbit with radius r in SI units is given by [63]

$$\begin{aligned} I &= \frac{2}{3}\frac{e^2}{4\pi\epsilon_0 c^3}|\ddot{\vec{r}}|^2 \\ &= \frac{2}{3}\frac{e^2}{4\pi\epsilon_0 c^3}\left(\frac{v^2}{r}\right)^2 \end{aligned} \tag{5.33}$$

where v is given by Eq. (5.23) and r is given by the Bohr-Sommerfeld quantization condition:

$$\begin{aligned} m\hbar &= m_e v_m r_m - \frac{eB_0}{2}r_m^2 \\ &= \pm r_m\sqrt{\left(\frac{eB_0 r_m}{2}\right)^2 + \frac{ke^2 m_e}{r_m}}. \end{aligned} \tag{5.34}$$

The canonical angular momentum is $L_z = m\hbar$ and $\pm$ indicates the sign of m.

Energy of the orbit is obtained by

$$E = \frac{1}{2}m_e v_m^2 - \frac{e^2}{4\pi\epsilon_0}\frac{1}{r_m} \tag{5.35}$$

and the semiclassical decay rate is evaluated as $\Gamma_m = I_m/\hbar(v_m^{(\pm)}/r_m)$ where the $\pm$ again indicates the sign of m. Note that this semiclassical treatment is only for the circular states, i.e. the high-$|m|$ states of a given n-manifold. Therefore the only allowed transitions are $n \to (n-1)$ transitions and the ground state does not decay.

Comparing the rates calculated semiclassicaly with the fully quantal rates in a 4.0 T field we saw that at $n = 10$ the quantal rate is larger by $\sim 11\%$, at $n = 20$ by $\sim 4\%$ and at $n = 30$ by less than 1%. Similar errors were found for other field strengths.

We can use this semiclassical method to estimate the relative size of the decay rate due to the cyclotron motion compared to the decay rate due to the magnetron motion. For example, the cyclotron decay rate in a 1.0 T field is $\sim$ 1 Hz for the $n = 3$ state which corresponds to 4 K. The decay rate of the $m = -85$ state due to the magnetron motion is also of the same size.

An important question is whether guiding center atoms with $m << -1$ can be trapped using magnetic field gradients. The change in the energy of the circular states as a function of the magnetic field strength is an indication of the affinity of the state to a magnetic field gradient. For the purposes of trapping Rydberg atoms using magnetic field gradients the internal energies of the atoms must increase with increasing magnetic field strength. To see if the atom is a high field or low field seeker we have approximated the motion of the electron in the orbit as a superposition of a cyclotron motion and a magnetron motion. The force on the center of mass of an atom is $\vec{F} = -(\vec{\nabla}B)(dE/dB)$ when it is slowly moving and has internal energy E. For an electron in a central potential, $dE/dB = (e/2)\hat{B}\cdot(\vec{r}\times\vec{v})$. We computed this quantity for the circular states in this semiclassical approximation and compared it to the dE/dB for pure cyclotron motion which is E/B. In a 1.0 T field, dE/dB is -24 K/T for $m = -85$ and is -20 K/T for $m = -125$. The comparable values in a 3.0 T field are -14 K/T and -12 K/T. The magnetron motion leads to high field seeking character.

To trap the anti-hydrogen atoms in a spatially dependent magnetic field which is stronger near the wall of the container, one needs the atoms to be low field seekers. The dE/dB for the magnetron motion can be counteracted by the cyclotron motion. The dE/dB for pure cyclotron motion at 4 K in a 1.0 T field is 4 K/T; this is a factor of 6 smaller in magnitude than for the magnetron motion at $m = -85$ and of opposite sign. Thus the contribution from the cyclotron motion into the low field seeking character of the atom is much smaller than the contribution into the high field seeking character of the atom from the magnetron motion. Hence we can conclude that either a lot of energy must be put into the cyclotron motion if the atoms are in circular negative m states or the atoms cannot be in nearly circular negative m states to be able be trapped by the spatially dependent magnetic field.

5.4 Conclusions

We have investigated the radiative cascade of highly excited hydrogen atoms in strong magnetic fields up to 4.0 T where we have considered states up to effective $n \sim 30 - 35$. We have considered two different cases of initial distributions. In one case, the states were equally populated within a small energy range and in the other case only the states with $|m| \sim n$ are populated. We have found that in the completely random ℓ, m case the time needed to populate the ground state by 10% is longer than the time it would take the anti-hydrogen atoms in recent experiments to hit the walls of the container due to their thermal speed. We have also shown that the experimentally reported black body radiation at 4 K did not affect the rates and the times needed to cascade down to the ground state by more

than a few percent which suggests that the black body radiation will not be of much help in getting the anti-hydrogen atoms to the ground state faster. This also means that it cannot slow down the cascade process by means of photoabsorption either.

Both in the completely random (ℓ, m) distribution and the $|m| \sim n$ distribution we see that states up to about $n \sim 20$ are not affected much by the magnetic field as would be expected considering the atomic unit of the magnetic field being of the order of 10^5 T, compared to the external field of a few Teslas.

When the initial distribution only involves states with $|m| \sim n$, time needed to populate the ground state is found to be longer than the completely random ℓ, m case. This results from the initial states being high-m states, which are circular or almost circular, and the fact that in completely random ℓ, m case these states comprise a smaller fraction of the population. The only allowed transitions for the circular states in the presence of the magnetic field are either $\Delta m = 0$ or $|\Delta m| = 1$ transitions depending on the parity change in the transition. Therefore the states with high-$|m|$ need to cascade down through smaller Δn transitions than those with smaller $|m|$. This greatly increases the decay time to the ground state from the highly excited states in the case where the cascade initiated from the negative large m states when the magnetic field points in the z-direction. When started from positive large m states the magnetic field actually speeds up the cascade process since in these states the electron is sped up by the magnetic field, radiating more intensely and decaying faster. In the case of the negative large m states the same argument can be drawn noting that this time the magnetic field slows down the electron which radiatively loses its energy at a slower rate than in the field free case. We have shown that when started from

a distribution of extreme negative m states, it takes about 800 times longer for the ground state to reach 10% population level than it does for the completely random ℓ, m distribution at $n = 30$ in 4.0 T magnetic field.

We have also found that when the radiative cascade starts from a circular state, the semiclassical treatment we have given here does a very good job in terms of yielding the decay rates, especially for the states with effective $n \gtrsim 20$. In cases where the large fraction of the atoms are in high-$|m|$ states, the old quantum theory can be used to evaluate the decay rates instead of the full quantum theory. We used this semiclassical method to estimate the decay rate due to the cyclotron motion of the electron and compare it to the rate originating from the magnetron motion of the electron in a circular orbit. We evaluated the force on the center of mass of the atom due to the magnetic field gradient and found that for the atoms to be trapped with a spatially dependent magnetic field they should be either in highly eccentric orbits or a large amount of energy must be imparted into the cyclotron motion of the electron.

APPENDIX

The exact Hamiltonian for a Hydrogen atom in an external magnetic field $\vec{B} = B\hat{z}$ is

$$H = \frac{\left(\vec{p} - q\vec{A}(\vec{r})\right)^2}{2\mu} + \frac{B^2}{2M}(x^2 + y^2) + \frac{BK}{M}x - \frac{1}{r^2} + \frac{K^2}{2M}$$

where $M = m_e + m_p$, $\mu = m_e m_p/M$ is the reduced mass, K is the pseudomomentum assumed to be in the y direction, and $q = e(m_p - m_e)/M$ [64]. The Hamiltonian (5.2)

can be obtained by making four approximations to the exact Hamiltonian. *(1)* We use the mass of the electron, m_e, instead of the reduced mass, μ. This gives a change at the $\sim 1/1000$ level and thus is not interesting for our purposes. *(2)* We do not include the last term $K^2/2M$ since this a constant and does not affect the composition of the states or their relative energies. *(3)* We do not include the term $B^2(x^2+y^2)/2M$. This term is ~ 500 times smaller than the comparable diamagnetic term in our Eq. (5.2) and thus does not have an important effect our results. *(4)* We do not include the term BKx/M. The effect of this term is the motional Stark effect since the atom has a velocity perpendicular to the magnetic field $\vec{B}$. The pseudomomentum

$$\vec{K} = \vec{P} + \frac{e}{2}\vec{B} \times \vec{r} \tag{5.36}$$

where $\vec{P} = M\vec{V}$ is the linear momentum of the proton and $\vec{r}$ is the distance from the proton to the electron. In a 4 T field and with a kinetic energy of 4 K the first term in $\vec{P}$ has magnitude $\sim 4.3 \times 10^{-25}$ kg m/s while the second term $e\vec{B} \times \vec{r}/2$ has magnitude $\sim 1.5 \times 10^{-26}$ kg m/s. Thus we can take $K \sim MV$ in our estimates. To see that the Stark shift does not have an important effect on our results, we note that the magnitude of the paramagnetic splitting of the levels due to the magnetic field is $\Delta E_P^{(1)} = (B/2)|\Delta m|$ and is $\sim 2.13 \times 10^{-6}$ (a.u.) in a 1 T field for the adjacent levels. The thermal speed of an anti-hydrogen atom at 4 K [5, 6] is ~ 260 m/s. An anti-hydrogen atom moving with a velocity $\vec{V}$ in a magnetic field $\vec{B}$ experiences an electric field of magnitude $\mathcal{E} \sim |\vec{V} \times \vec{B}|$. The correction to the energy levels in the first approximation in an n-manifold due to the

linear Stark effect resulting from this field is $E_S^{(1)} = \frac{3}{2}\mathcal{E}n(n_1 - n_2)$ where n_1 and n_2 are the parabolic quantum numbers [61]. The separation of the adjacent Stark levels would be $3\mathcal{E}n$ which is $\sim 4.5 \times 10^{-8}$ (a.u.) in $n = 30$ manifold for an atom moving at 260 m/s in a 1 T field. Note that the paramagnetic splitting is larger than the Stark splitting by roughly two orders of magnitude, therefore the linear Stark effect is negligible.

Actually, the eigenvalues and eigenvectors of $VBx + BL_z$ can be found analytically within an n-manifold. We computed the average spread in m for each state in an n-manifold which we defined to be $\Delta m^2 \equiv \langle L_z^2 \rangle - \langle L_z \rangle^2$. We averaged Δm^2 over all of the states and found it to be $3V^2n^3(n+1)/4$ which is $\sim 9 \times 10^{-3}$ for $n = 30$. Again this shows that most states hardly mix with other m's and the main mixing is with $m \pm 1$. Since each state is mixing with states of similar radiative properties, our results on radiative cascade should be accurate to better than a few percent.

Clearly, the extent to which the Hamiltonian of Eq. (5.2) is accurate depends on the application. For investigations of large scale and/or averaged quantities, several different estimates including comparison of the sizes of MV and $eBr/2$ in the pesudomomentum, comparison of the proton cyclotron frequency to the frequency of the electron in the guiding center atom and the size of the motional Stark field to the magnetic field suggest that the Hamiltonian (5.2) is good enough for accuracy better than $\sim 10\%$ for $n \lesssim 60$ for $B \lesssim 4$ T and kinetic energy less than 4 K.

In addition to the strong magnetic fields, anti-hydrogen experiments also involve spatially dependent electric fields of $\sim$ 10 V/cm which is roughly a factor of $\sim$ 1-4 times larger than the motional Stark field. Since the configurations of the traps are not known

at this time, we will not speculate on the effect of these electric fields. In the light of the estimates in this appendix, it seems unlikely that these electric fields will have a substantial effect on our results.

CHAPTER 6

CHAOTIC IONIZATION OF A HIGHLY EXCITED HYDROGEN ATOM IN PARALLEL ELECTRIC AND MAGNETIC FIELDS

6.1 Introduction

Within the last two decades, systems whose underlying classical mechanics exhibit chaos attracted much attention both from the theoretical and the experimental point of view. Considerable effort has been made to observe and explain chaotic behaviour within the purely quantum mechanical framework. These efforts resulted in observations of a rich variety of signatures of chaos in the energy level statistics [65], wave functions [66], absorption-ionization spectra [67, 68, 69] etc., of quantum systems whose classical counterparts exhibit chaos. Unfortunately, attempts to explain the physical origins of such *irregular* behaviour in quantum mechanics have failed and it was found that even though quantum systems imitate classical systems for a finite time, the classical chaos is suppressed in quantum systems in the long time limit. In the sense of positive Liapunov exponents, chaos does not exist in quantum mechanics, mainly due to the linearity of the Shrödinger equation. Due to its lack of origin in the quantum mechanics, much work went into developing semiclassical and statistical quantum mechanical theories such as random matrix theory [70] to study manifestations of classical chaos in quantum systems [71]. Unbounded irregular scattering has attracted particular attention to generalize certain signatures of chaos to

a wide variety of systems since Blümel and Smilansky [72] showed that Ericson fluctuations are a universal phenomenon. These fluctuations were originally proposed by Ericson [73] as a signature of chaos in the photoabsorption spectrum of compound nuclear reactions before its experimental observation [74].

In this chapter, chaotic ionization of Rydberg systems have been investigated in the energy domain both classically and semiclassically for different regimes of microwave ionization [75] characterized by a scaled frequency. Furthermore, classical theories such as closed orbit theory have been developed to analyze long range chaotic fluctuations in the photoabsorption spectra to interpret spectra of atoms in external fields. But there is a lack of effort in the exploration of chaotic ionization dynamics in the time domain. Recently Mitchell *et al.* performed classical calculations to investigate ionization of a hydrogen atom in parallel electric and magnetic fields as an example of chaotic escape dynamics in an open system in the time domain [76, 77]. In their simulations, they excited a hydrogen atom to a Rydberg state with $n \sim 80$ and studied the time-dependent structure of the ionization rate for a distribution of launch angles and energies. They observed distributions of electrons ionizing via a train of pulses - a consequence of the classical chaos induced by the external magnetic field. They looked at the ionization rate and studied the initial launch angular distribution of the classical trajectories as a function of the time it takes the electrons to reach their detector. They observed a self-similar structure in the launch angle versus time distribution which they were able to link to a fractal structure. They showed that each escape segment in the launch angle-time distribution corresponds to a particular pulse in the pulse train of the ionizing electrons and therefore the fractal structure of the launch angle

versus time distribution is directly reflected in the time-dependent ionization-rate. They also argued that the true quantum mechanical treatment of this problem may bring in some interesting effects due to interference and the Heisenberg uncertainty principle. The purpose of this paper is to investigate these purely quantum mechanical effects and to explore quantum signatures of the underlying classical chaos for this system in the time domain.

We will discuss results from our non-perturbative quantum mechanical and classical trajectory Monte Carlo (CTMC) calculations and observe ionization pulse trains induced by chaos. We present results on time-dependent ionization of a hydrogen atom excited to high Rydberg levels around $n = 40$, $n = 60$ and $n = 80$ by a short laser pulse in parallel electric and magnetic fields. We have further extended our calculations up to $n = 120$ and observed very similar behaviour in the time-dependent dynamics that we have seen for the lower n values. We look at the current of ionizing electrons as a function of time through a spherical detector placed just outside the peak of the potential. We compare these results with those from our CTMC calculations to see the extent to which the Bohr correspondence principle holds. We look at the wave function of the system as a function of time and investigate angular momentum distribution of the escaping electrons as they hit the detector. We compare our results with the classical calculations of Mitchell *et al.* [76, 77] where possible. We study the time evolution of the interference patterns on the detector. We observed dependence of the escape time of a trajectory on its classical launch angle which incited us to manipulate the pulse train by placing nodes at certain angles into the angular distribution of the initial wave packet in our quantum wave packet calculations. At this point we introduce core scattering into the problem via a model core potential

and explore the coupling between two different mechanisms that produce ionization pulse trains. Then we turn to the question of the onset of chaos in our system and introduce scaled energy E_c to examine the transition from chaotic ionization dynamics to regularity as we vary the magnetic field strength. We also study the time-dependent autocorrelation function and the corresponding spectral autocorrelation function to look for any effects of Landau quantization, such as the quasi-Landau oscillations. We perform our quantal and classical calculations in parallel in each of these sections to see if the Bohr correspondence principle applies in each case. The work presented in this chapter has been published as a paper in the Journal of Physics B [78].

6.2 Theory

In the following two subsections we discuss methods of non-perturbative quantum mechanical wave packet and the classical trajectory Monte Carlo (CTMC) calculations. We use atomic units throughout this chapter unless we state otherwise.

6.2.1 Quantum mechanical time-dependent wave packet method

The total Hamiltonian of a hydrogen atom in parallel electric and magnetic fields is:

$$\begin{aligned} H_0 = \quad & -\frac{1}{2}\frac{d^2}{dr^2} - \frac{1}{r} + \frac{l(l+1)}{2r^2} + \frac{\gamma}{2}L_z \\ & + \frac{\gamma^2}{8}r^2\sin^2\theta + \mathcal{F}r\cos\theta \end{aligned} \tag{6.1}$$

where $\gamma = B/(2.35 \times 10^5 \text{ T})$ is the magnetic field strength in atomic units when B is in T, and $\mathcal{F} = F \times (1.94 \times 10^{-10} \text{ a.u./(V/cm)})$ is the electric field strength in atomic units when F is in V/cm. The external fields are taken to be in the z-direction such that $\vec{B} = B\hat{z}$ and $\vec{F} = F\hat{z}$, respectively. A detailed account of the approximations made in the Hamiltonian (6.1) can be found in Ref. [58]. We break up the Hamiltonian H_0 into two pieces; the atomic Hamiltonian H_a, the static field Hamiltonian H_f:

$$H_0 = H_\text{a} + H_\text{f} \tag{6.2}$$

and introduce a laser term $H_{\rm l}$ to excite the hydrogen atom to a Rydberg state with energy E,

$$H = H_0 + H_{\rm l} \tag{6.3}$$

with

$$\begin{aligned} H_{\rm a} &= -\frac{1}{2}\frac{d^2}{dr^2} - \frac{1}{r} + \frac{l(l+1)}{2r^2} && \text{(6.4a)} \\ H_{\rm f} &= \frac{\gamma}{2}L_z + \frac{\gamma^2}{8}r^2\sin^2\theta + \mathcal{F}r\cos\theta. && \text{(6.4b)} \\ H_{\rm l} &= \zeta(t)e^{-i(E-E_g)t}r\cos\theta && \text{(6.4c)} \end{aligned}$$

where $\zeta(t) = \exp\{-t^2/t_{\rm w}^2\}$ is the Gaussian laser pulse and E_g is the energy of the initial ground state that is being excited. We use first order time-dependent perturbation theory to evaluate the time-dependent wave function of the system. The total first order wave function $\Psi(\vec{r},t)$ within the time-dependent perturbation theory is

$$\Psi(\vec{r},t) = \psi(\vec{r},t)e^{-iEt} + \psi_g(\vec{r})e^{-iE_gt}. \tag{6.5}$$

Here $\psi_g(\vec{r})$ is the wave function of the initial ground state that is being excited to the Rydberg state with energy E. $\psi(\vec{r},t)$ is the wave packet excited by the laser. Within this approximation, the time-dependent Schrödinger equation for $\psi(\vec{r},t)$ reads [27]

$$\left(i\frac{\partial}{\partial t} - (H_0 - E)\right)\psi(\vec{r},t) = S_0(r,t). \tag{6.6}$$

Note that the energy E of the Rydberg state that is being excited is subtracted from the diagonal elements of the Hamiltonian to reduce the numerical errors due to phase accumulation. We choose the source term $S_0(r,t)$ to be spherically symmetric and spatially compact. It is launched to a Rydberg state with energy E by a short laser pulse;

$$S_0(r,t) = \delta_{l,0}\ \zeta(t)\ r^2 e^{-r/2}. \tag{6.7}$$

The laser pulse peaks at $t = 0$ and we start time propagating Eq. 6.6 at $t = -6t_{\rm w}$ where $t_{\rm w}$ is the width of the laser pulse. In our calculations we have chosen $t_{\rm w}$ to be $\tau_{Ryd}/15$ where $\tau_{Ryd} = 2\pi(-2E)^{-3/2}$ is the Rydberg period of the state being excited. Integrating Eq. 6.6 over one time step and using the trapezoidal rule for the integrations, one obtains

$$i\big[\psi(t+\delta t) - \psi(t)\big] = \frac{\delta t}{2}\Big((H_0 - E)\big[\psi(t+\delta t) + \psi(t)\big] + \big[S_0(t+\delta t) + S_0(t)\big]\Big) \tag{6.8}$$

which yields the quantum propagator,

$$\psi(t+\delta t) = \left(\frac{1 - i(H_0 - E)\delta t/2}{1 + i(H_0 - E)\delta t/2}\right)\psi(t) - \frac{i\delta t}{1 + i(H_0 - E)\delta t/2} S_0(t + \frac{\delta t}{2}) + \mathcal{O}[\delta t^3]. \tag{6.9}$$

We further make the approximation

$$\frac{i\delta t}{1 + i(H_0 - E)\delta t/2} \simeq i\delta t + \frac{\delta t^2}{2}(H_0 - E) + \mathcal{O}[\delta t^3] \tag{6.10}$$

for the second term on the right hand side which preserves the order of the propagator. The operator acting on $\psi(t)$ in Eq. 6.9 is the lowest order Padé approximation to the time evolution operator e^{-iH_0t}. We therefore evaluated the first term on the right hand side of Eq. 6.9 by means of the split operator technique without altering the order of the propagator. We used a higher order split operator technique than the one employed on pg.2 in Ref. [80]. We have found that going to higher order in the split operator technique significantly reduced the phase errors.

$$\begin{aligned}
\psi(t+\delta t) &= \left(\frac{1-iH_{\rm f}\delta t/4}{1+iH_{\rm f}\delta t/4}\right)\left[\left(\frac{1-i(H_{\rm a}-E)\delta t/4}{1+i(H_{\rm a}-E)\delta t/4}\right)\left[\left(\frac{1-i(H_{\rm a}-E)\delta t/4}{1+i(H_{\rm a}-E)\delta t/4}\right)\right.\right. \\
&\quad \times\left[\left(\frac{1-iH_{\rm f}\delta t/4}{1+iH_{\rm f}\delta t/4}\right)\psi(t)-\frac{1}{4}\left(i\delta t+\frac{\delta t^2}{2}(H_0-E)\right)S_0(t+\frac{\delta t}{2})\right] \\
&\quad \left.-\frac{1}{2}\left(i\delta t+\frac{\delta t^2}{2}(H_0-E)\right)S_0(t+\frac{\delta t}{2})\right] \\
&\quad \left.-\frac{1}{4}\left(i\delta t+\frac{\delta t^2}{2}(H_0-E)\right)S_0(t+\frac{\delta t}{2})\right]+\mathcal{O}[\delta t^3]. \qquad (6.11)
\end{aligned}$$

The effect of the external fields on the solutions of the field free hydrogen atom can simply be deduced by noting that [see Ref. [79], pg. 250]

$$\cos\theta\, Y_l^m = \sqrt{\frac{(l+1)^2-m^2}{(2l+1)(2l+3)}}\, Y_{l+1}^m + \sqrt{\frac{l^2-m^2}{(2l+1)(2l-1)}}\, Y_{l-1}^m \tag{6.12}$$

$$\begin{aligned}\sin^2\theta\, Y_l^m = & -\sqrt{\frac{[(l+1)^2-m^2][(l+2)^2-m^2]}{(2l+1)(2l+3)^2(2l+5)}}\, Y_{l+2}^m \\ & + \left[1 - \frac{(l+1)^2-m^2}{(2l+1)(2l+3)} - \frac{l^2-m^2}{(2l+1)(2l-1)}\right] Y_l^m \\ & - \sqrt{\frac{[l^2-m^2][(l-1)^2-m^2]}{(2l+1)(2l-1)^2(2l-3)}}\, Y_{l-2}^m.\end{aligned} \tag{6.13}$$

From this it can be seen that the electric field mixes state l with states $l \pm 1$ and the magnetic field mixes state l with states l, $l \pm 2$. A natural representation of the wave function can be realized on an (l, r) grid. On this grid, operator $H_{\rm f}$ acts only along the l-direction and it is pentadiagonal. The atomic Hamiltonian $H_{\rm a}$ acts along the r-direction and involves the usual kinetic energy operator and the Coulomb potential. We describe the second derivative in the kinetic energy within the three point differencing scheme and therefore $H_{\rm a}$ is tridiagonal in r (see Ref. [80]) and diagonal in l. The number of points N_l in the l-direction are chosen to be 150, 200, and 250 for $n = 40$, $n = 60$, and $n = 80$ cases respectively. The number of points N_r in the r-direction are 1000, 1500, and 2500 for $n = 40$, $n = 60$, and $n = 80$ and the results we present are converged with respect to N_l and N_r.

We use square root mesh along the r-direction of the grid as described in Ref. [80]. The radial extent of the spatial direction on the grid, i.e., box size $r_{\rm f}$, is chosen to be twice the radial extent of the peak of the potential, i.e., $r_{\rm f} \sim 2r_{\rm p}$. The number of points in

this direction is chosen such that the maximum r-mesh spacing δr_{max} is less than $0.5/p_{\text{max}}$ where p_{max} is the largest possible linear momentum an ionized electron can attain, i.e.,

$$p_{\text{max}} = \sqrt{-2(E - V(r_{\text{f}}))} = \sqrt{(1/n^2) + 5\sqrt{F}}. \tag{6.14}$$

The time step we use for the time propagation of Eq. 6.9 is chosen such that it is smaller than the time scales involved in our problem. The time scale set by the electric field can be deduced from the electric field part of the propagator in Eq. 6.11;

$$\exp\{-izF\delta t/2\} \simeq \frac{1 - izF\delta t/4}{1 + izF\delta t/4} \tag{6.15}$$

which is $\sim -i$ for $zF\delta t/4 \sim 1$, giving a $\pi/2$ phase shift. This constricts the appropriate time step below $4/(Fr_{\text{f}})$. In the same manner, the magnetic field part of the propagator contributes another $\pi/2$ phase error when $\exp\{-iB^2\rho^2\delta t/16\} \sim 1$ which implies $\delta t \lesssim 32/(B^2 r_{\text{f}}^2)$. The time step is also chosen to be much less than the Rydberg period of the state corresponding to the energy E, specifically, $\delta t \sim \tau_{\text{Ryd}}/800$. We have performed convergence checks with respect to both δr_{max} and δt and the results we present are converged within a percent.

Since we are using a finite size box to time propagate the wave function, we use a mask function to absorb current that reaches the end of the box to prevent reflections from the box edge. The form of the mask function is $M(r) = 1 - s\ \delta t((r - r_{\text{m}})/(r_{\text{f}} - r_{\text{m}}))^2$ and it spans the radial range from $r_{\text{m}} = (1/\sqrt{F} + 2r_{\text{f}})/3$ to r_{f}. The parameter s quantifies the strength of the absorption. To remove the part of the wave function that reaches the end of

the box, we simply multiply the wave function with $M(r)$ for each l on the grid after each time step during the time propagation.

Since we are interested in time-dependent current of ionizing electrons, we calculate the probability current density through a spherical detector which we then integrate over the surface to obtain the current as a function of time. We place the detector such that its surface is located just outside the peak of the potential. When the electron goes beyond this peak in space it is considered ionized. Since the peak of the potential is located at $r_{\rm p} = 1/\sqrt{F}$, we chose the radius of our spherical detector at $r_{\rm s} = (r_{\rm p} + 2r_{\rm f})/3$. The total current through the surface of the detector is therefore

$$\Phi = -\mathrm{Re}\left[i \sum_l \psi^*(r_{\rm s}, l, t) \frac{\partial \psi_l(r, l, t)}{\partial r}\bigg|_{r=r_{\rm s}} \right]. \tag{6.16}$$

To check our codes, we have also calculated the total current as the rate of change of the total probability that lies within the spherical region enclosed by the detector after the laser pulse is turned off. We find total agreement between the two methods as expected since

$$\frac{\partial \wp(r,t)}{\partial t}\bigg|_{r=r_{\rm s}} = -\frac{\partial j(r,t)}{\partial r}\bigg|_{r=r_{\rm s}} \tag{6.17}$$

where $\wp$ is the survival probability density within the spherical region and j is the probability current density through the surface of the detector.

6.2.2 Classical trajectory Monte Carlo method

To compare results of the fully quantal time-dependent formalism to the underlying classical dynamics, we have also performed classical calculations in the framework of classical trajectory Monte Carlo (CTMC) method. We solved Newton's equations for the trajectory of the hydrogenic electron in presence of the external parallel electric and magnetic fields using fourth order adaptive time step Runga-Kutta algorithm described in Ref. [81]. We worked in cartesian coordinates and time propagated the trajectories until certain criteria are met. Time propagation of a trajectory is terminated when the electron passes through the spherical detector or when a predefined final propagation time $t_{\rm f}$ is reached. When the propagation of the Newton's equations is terminated, it is binned in time as an escaped trajectory or discarded depending on whether the electron has reached at the detector or not. After a large number of trajectories are calculated, what is left is a probability distribution of survival in time within the spherical region inside the detector. Each bin in time contains a fraction of probability to escape within the corresponding time interval. Integrating this probability distribution over time up to a particular bin τ gives the probability of survival $P(\tau)$ inside the spherical region up until the time τ. Widths of the time bins in our calculation are $d\tau = t_{\rm f}/200$. From this survival probability, current through the spherical detector is evaluated as $(P(\tau) - P(\tau - d\tau))/d\tau$. To have good statistics, we had to sample a large number of trajectories and we have checked convergence with respect to the number of trajectories to insure good statistics. The results we present here have been obtained with 3×10^6 classical trajectories.

To closely match the fully quantal case, each classical trajectory is launched in a spherically symmetric fashion, i.e., the distribution of the cosine of the angle θ at which a trajectory is launched is chosen from a flat distribution to mimic the angular distribution of the initial quantum wave packet. The azimuthal angle φ is a cyclic coordinate due to the cylindrical symmetry of the problem. There are three random initial parameters for each launched trajectory in our calculations: the cosine of the launch angle of the trajectory, launch time distribution $\mathcal{F}(t)$, and initial energy distribution $\mathcal{G}(\epsilon)$ of the trajectory. The launch time distribution is given by the squared absolute value of the Gaussian laser pulse $\zeta(t)$ in Eq. 6.4c, and the energy distribution $\mathcal{G}(\epsilon)$ is evaluated as the squared absolute value of the Fourier transform of $\zeta(t)$.

$$\begin{aligned} \mathcal{F}(t) &= e^{-2t^2/t_{\mathrm{w}}^2} \\ \mathcal{G}(\epsilon) &= e^{-(\epsilon-E)^2 t_{\mathrm{w}}^2/2} \end{aligned} \tag{6.18}$$

Here E is the central energy of the laser pulse, and t_{w} is the width of the laser pulse in time. We have generated these Gaussian distributions of launch time and initial energy using the methods described in Ref. [81]. The laser pulse used to excite the Rydberg states is exactly the same as the one used for the quantum wave packet calculations.

6.3 Results

6.3.1 Flux of ionizing electrons

Results from the calculations for the current of ionizing electrons through the spherical detector for $n = 40$, 60, and 80 can be seen in Fig. 6.1(a), (b), and (c) respectively. Figures show both quantum mechanical (solid curve) and classical (dotted curve) calculations to contrast the quantum mechanical current with its classical counterpart which exhibits chaos. The electric and magnetic field strengths for the $n = 40$ calculations are $B = 3.92$ T and $F = 304$ V/cm. For the cases of $n = 60$ and 80, we scaled the magnetic field we used for $n = 40$ by $1/n^3$ and the electric field by $1/n^4$ to stay at the same dynamical regime. The external field strengths for these calculations are chosen such that the system is in the n-mixing regime and the energy is above the classical ionization threshold. The box size used in each of the quantum mechanical calculations are 8000, 18000, and 32000 (a.u.) for $n = 40$, $n = 60$, and $n = 80$ respectively and the width of the laser pulse is $t_{\rm w} = \tau_{\rm Ryd}/15$. As pointed out in Ref. [77], the actual resolution of the pulses in the pulse train is determined by the interplay of Δt and ΔE. Therefore, since both Δt and ΔE contribute to the broadening of the pulses, there exists an optimal set of $(\Delta t, \Delta E)$ for which the ionization pulses along the time axis are the sharpest. We have found that a longer pulse duration than we defined above actually gives a noticeably sharper pulse train than that seen in Fig. 6.1. The number of angular momenta included in each calculation scales roughly as $\sim n$ and is 150 for $n = 40$. We time propagate the wave function ψ for $(9/2)\tau_{\rm Ryd}$ in each case of

n. We have also extended our calculations up to $n = 120$ and did not find any significant shifts from the time-dependent dynamics we describe below for lower n values.

Whether a classical electron will ionize or not, and the time of its ionization, depend on the initial launch angle θ of the classical trajectory. The trajectories that are launched directly downhill, i.e., at $\theta = \pi$, will be the first ones to ionize. Ionization current due to these electrons makes up the first prominent pulse in each of the figures in Fig. 6.1, which is called the direct pulse. Classically, this corresponds to the first prominent escape segment in the self-similar pattern of the classical launch angles versus time seen in Fig. 2(a) and (b) of Ref. [77].

A remake of Fig. 2(a) and (b) of Ref. [77] can be seen in Fig. 6.2, which is generated using the data kindly supplied to us by K. A. Mitchell. Fig. 6.2(a) shows two time-dependent ionization rate curves as a function of scaled time t, which is related to the real physical time $\hat{t}$ through $t = \hat{t}n^3$. The calculation is for $n = 80$ in parallel electric and magnetic fields of $F = 19$ V/cm and $B = 0.49$ T. The ionization rate depicted by the solid line is calculated using an ensemble of trajectories with a precise energy and launch time, whereas the smooth solid line is calculated using a Gaussian wave packet (see Ref. [77] for more detail). Fig. 6.2(b) shows the time it takes for a trajectory to ionize as a function of its launch angle. This launch angle distribution is referred to as the escape-time plot in Ref. [77]. Each of the *icicles* in this plot marks out a range of launch angles such that when a trajectory is launched at an angle from within this range, it ionizes through a particular pulse in Fig. 6.2(a). These icicles are called escape segments and every escape segment gives rise to a particular pulse inthe ionization rate. The dotted lines in Fig. 6.2(b) matches

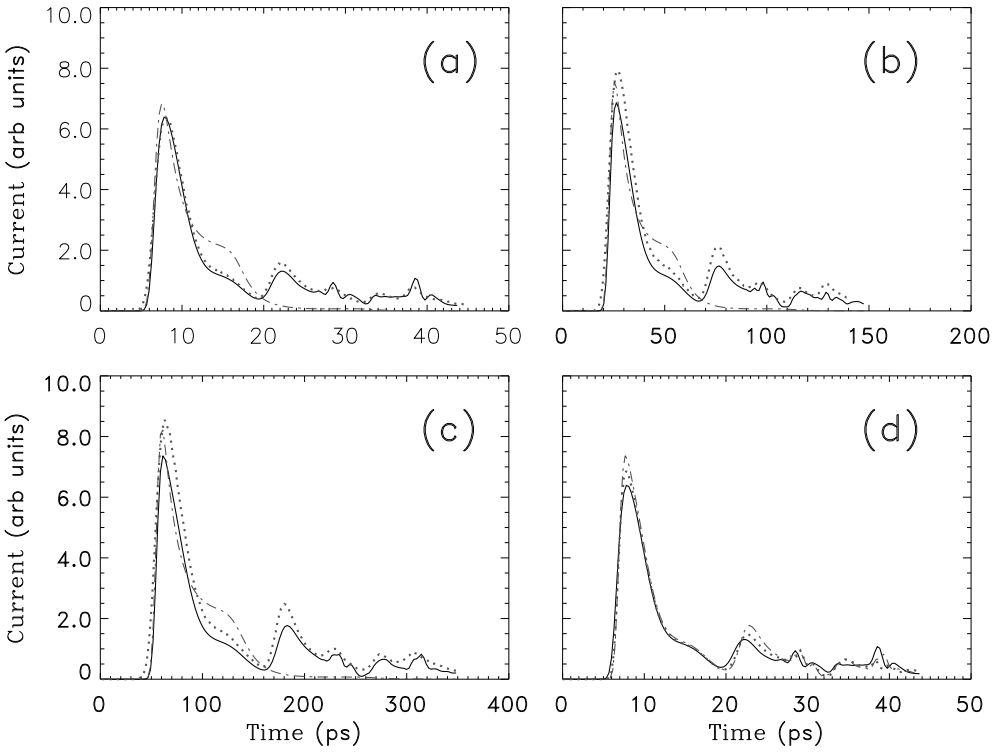

Figure 6.1: Current-time plots for ionization with excitation to (a) $n = 40$, (b) $n = 60$, and (c) $n = 80$ states of hydrogen via a short laser pulse in parallel electric and magnetic fields. Results from quantum mechanical wave packet (solid curve) and CTMC (dotted curve) calculations are plotted on top of each other along with the pure electric field case (dash-dotted curve). (d) shows just the quantum mechanical current-time plots in (a), (b), and (c) plotted together for comparison.

each escape segment with its corresponding pulse in the ionization pulse train. The escape segments of Fig. 6.2(b) show a self-similar structure and Ref. [77] connects this structure to fractal structure in the classical mechanics of the escape dynamics.

In the self-similar pattern of launch angles seen in Fig. 6.2(b), the trajectories launched from within the angular range $\theta \sim \pi \pm 0.94$ rad make up the direct ionization pulse. This escape segment is by far the widest compared to the rest of the escape segments in the pattern. Also notice that all the direct pulses seen in Fig. 6.1 terminate with a *knee* structure. This knee is due to the electrons that were not launched directly downhill but at a slightly smaller or larger angle. They are turned around by the force from the electric field before they can scatter from the nucleus and reach the detector before the direct pulse of electrons has completely passed through the detector. This knee is absent in the previous classical calculations of Mitchell *et al.* where they used a minimum uncertainty Gaussian wave packet for their ensemble of trajectories to obtain a smooth ionization rate curve, as the one seen in Fig. 6.2(a). In some of their calculations [76], the direct pulse is smaller than the second peak in the pulse train whereas our calculations and the calculations presented in Fig. 6.2(a) yield a larger prominent direct pulse compared to the rest of the peaks in the pulse train. This is due to the fact that Ref. [76] uses a p_{x} angular distribution for the initial launch angles of the trajectories while Fig. 6.2 and we use an s-wave distribution. Irregular peaks that come after the direct pulse in the pulse train are the electrons that were launched from angles outside of $\theta \sim \pi \pm 0.94$ rad. Their ionization is delayed for different durations of time depending on their launch angle. The trajectories perform a cyclotron motion due to the magnetic field while going down the potential hill as seen from the wave

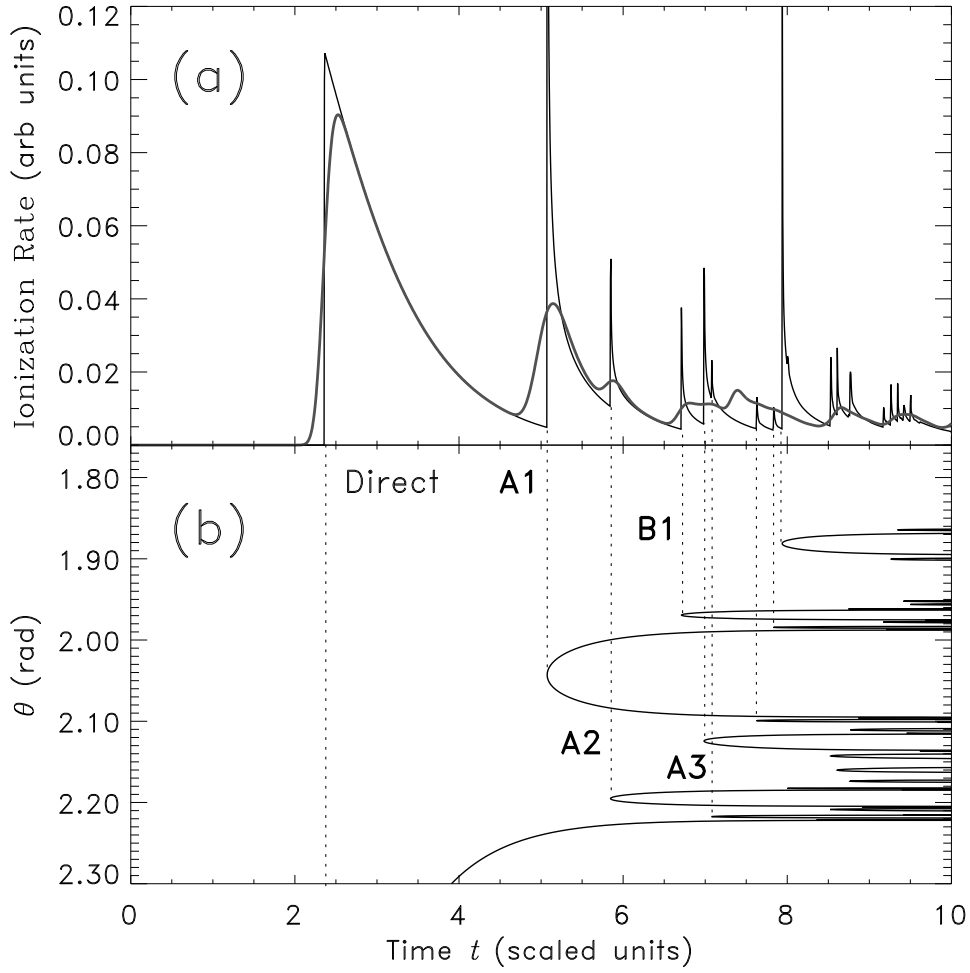

Figure 6.2: Classical calculations of Ref. [77] for the ionization of hydrogen in parallel electric and magnetic fields of $F = 19$ V/cm and $B = 0.49$ T for $n = 80$. (a) shows the ionization rate as function of scaled time, and (b) shows the scaled time for a trajectory to escape as a function of its launch angle. The solid curve in (a) is calculated using an ensemble of trajectories with a precise launch time and energy whereas the smooth solid curve is calculated using a Gaussian distribution for the energy and the launch time. Each of the escape segments seen in (b) correspond to a particular pulse in the ionization rate and are matched with their pulse via the dotted lines. The scape segment that gives rise to the direct pulse peaks at $\theta = \pi$ and most of it falls outside the θ range plotted. (We thank K. A. Mitchell for kindly supplying the data for this partial replot of Fig. 2 of Ref. [77]. We also thank K. A. Mitchell and J. B. Delos for their permission to include this replot in this paper.)

function plots of Fig. 6.3. Classically, these trajectories originate from the various smaller escape segments marked as **A1**, **A2**, **A3**, etc., in Fig. 6.2(b). As the pulse train grows longer, more escape segments contribute to a given pulse in the pulse train. Therefore one would expect that these later pulses in the pulse train would show quantum mechanical interference effects most prominently. This is indeed displayed in the time-dependent wave functions seen in Fig. 6.3. The fact that the launch angle of a classical trajectory determines its place in the pulse train suggests that by manipulating the launch angle distribution of the trajectories, we can tailor the pulse train to a desired shape (see Sec. III D).

Fig. 6.3 shows snapshots of the probability distribution $|\psi|^2$ in time for $n = 80$ in the ρ-z plane. The nucleus is positioned at the origin and the force from electric field is pointing in the negative z-direction. At $t = 58$ ps (Fig. 6.3(a)), the spherically symmetric outgoing wave is seen just when the current is near the peak of the direct pulse in Fig. 6.1(c). This outgoing wave gives rise to the direct ionization pulse. At $t = 117$ ps (Fig. 6.3(b)), the first pulse of ionizing electrons reaches the spherical detector and gets absorbed by the spherical mask just after it crosses the detector surface at $r = 2.68 \times 10^4$ (a.u.). The part of the wave function that corresponds to the ionizing electron current density (labeled as β in Fig. 6.3(b)) goes downhill as it performs a cyclotron motion due to the magnetic field parallel to the electric field. This β part of the wave function is the direct pulse of Fig. 6.1(c), at the time when the current reaches the knee of the direct pulse along the pulse train. Note that this part of the wave function does not yet show any interference patterns. This is due to the fact that it corresponds to the classical trajectories launched from within the first prominent escape segment in Fig. 6.2(b). The part of this escape segment that

makes up the direct pulse has no angular overlap with the rest of the escape segments. This means that there is only one way for a trajectory to escape during the direct pulse and that is to be launched from within this first escape segment. The lack of alternative escape paths results in no interference patterns in the wave function. The part of the wave function marked by σ is relatively localized between $0 < z < -1$ (a.u.) and shows the Stark oscillating part of the wave function. Nodes of this part of the wave function corresponds to the nodes of the Stark sublevels. Fig. 6.3(c) shows the wave function at $t = 175$ ps, near the peak of the second pulse in Fig. 6.1(c). The wave function shows two types of scattering: the β part seen in Fig. 6.3(b) and a part that is going directly down the potential hill (marked as κ). The β part makes up the skirt of the direct pulse in Fig. 6.1(c) onto which the second pulse sits. The κ part of the wave function gives rise to the second pulse in the pulse train. Note that there is an interference pattern on this part of the wave function which is due to the interference between the components of the wave function moving in opposite direction along the ρ dimension as they perform cyclotron motion rolling down the potential hill. The classical escape segment responsible for the second pulse has an angular overlap with the first prominent escape segment of Fig. 6.2(b), which is causing interference between the κ and the β parts of the wave function. Fig. 6.3(d) shows the wave function at $t = 233$ ps, around the third pulse in Fig. 6.1(c). The β and the κ parts of the wave function has now completely blended into each other such that the β part of the wave function is hardly recognizable. This is so since the escape segment that gives rise to the third pulse in Fig. 6.2(b) now overlaps in angle with both the first prominent escape segment as well as the escape segment **A1** which is responsible for the second pulse. The increased number of

ways to escape during the third pulse results in interference between these channels, leading to interference between the β and the κ parts of the wave function. The interference patterns formed show two standing wave patterns perpendicular to each other with roughly the same wavelength suggesting that both components have similar momentum. Figs. 6.3(e) and (f) sample the wave function further along the pulse train $t = 292$ ps and $t = 350$ ps. In these cases, the interference patterns in the wave function are noticably more complicated than those of the earlier times. The classical escape segments corresponding to these later times overlap with all the escape segments that gave rise to the previous pulses, resulting in the ever increasing complexity of the interference patterns. The interference patterns are dynamic, and resemble scars of the classical periodic orbits going downhill as they perform a cyclotron motion about the z-axis. Such scars are commonly observed in bound state eigenfunctions of classically chaotic Hamiltonian systems [66] and are well known signatures of chaos in quantum systems.

The classical chaotic dynamics of this open system can be attributed to the presence of the external magnetic field, without which the dynamics would be regular. To check this, we have extended our quantum mechanical wave packet calculations to exclude the magnetic field. This should result in a single prominent pulse of ionization in the absence of core electrons, and this is indeed in accord with our results (dash-dot-dashed curves in Fig. 6.1(a), (b), and (c)).

Fig. 6.1(d) shows all three quantum mechanical calculations for $n = 40$, 60, and 80 on top of each other to see if there is any effect due to the $1/n^3$ decreasing of the Rydberg

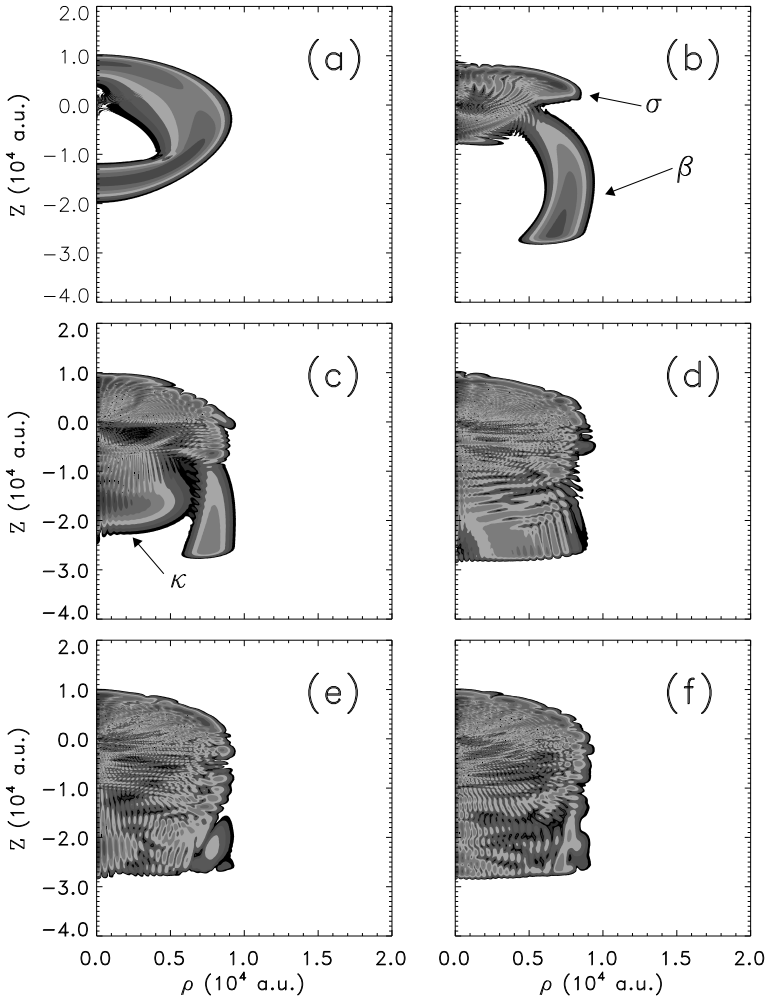

Figure 6.3: Snapshots of the absolute value squared wave function of hydrogen in parallel electric and magnetic fields for $n = 80$ case at (a) 58 ps, (b) 117 ps, (c) 175 ps, (d) 233 ps, (e) 292 ps, and (f) 350 ps. In (b), σ marks the part of the wave function that shows Stark oscillation whereas β shows the one that gives rise to the direct ionization pulse in Fig. 1(c). In (c), κ shows the part of the wave function that is responsible for the second peak in the pulse train.

level spacings as n is increased. We see no significant differences within the n range we investigate.

6.3.2 l-distributions of ionizing electrons

Fig. 6.4 shows the snapshots of the time-dependent angular momentum distribution of $|\psi|^2$ within the region bounded by the spherical detector for $n = 80$. The main plot in each panel is for the case of the parallel electric and magnetic fields whereas the inserts are for the pure electric field case. Fig. 6.4(a), (b), and (c) are snapshots of the l-distribution during the direct ionization pulse of Fig. 6.1(c) at $t = 44$ ps, $t = 58$ ps, and $t = 85$ ps, respectively. The angular momenta of the initially s-wave electrons spread to higher l as the wave function expands outward (Fig. 6.3(a)). At $t = 58$ ps, the l-distribution shows two distinct types of behavior: the part of the distribution that propagates out to higher l in the same manner as the pure electric field case (marked as ξ), and the irregular part that remains at low l (marked as δ). Given the fact that the ξ part of the distribution almost coincides with that of the pure electric field case, and in the pure electric field case one ends up with a single prominent ionization pulse, we can conclude that the ξ part of the distribution represents the electrons that are escaping through the direct pulse of Fig. 6.1(c). The δ part of the distribution however classically represents the electrons that stay bound in the atom and escape at a later time through another pulse in Fig. 6.1(c). The extent of the ξ part of the distribution reaches $l \sim 150$ at $t = 85$ ps. By this time the direct pulse has well passed its peak and $\sim 13\%$ of the electrons have escaped. Fig. 6.4(d) shows the l-distribution at $t = 129$ ps, just before the knee of the direct pulse reaches the detector. Note that the ξ part

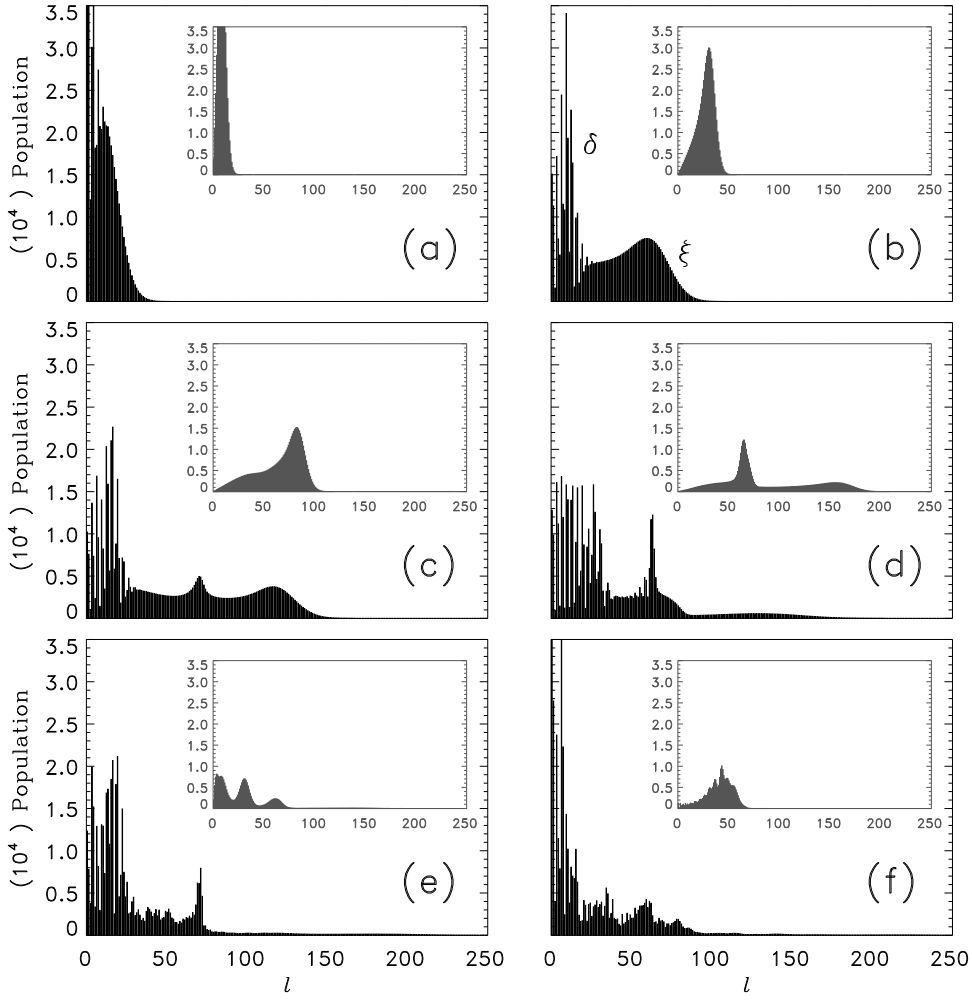

Figure 6.4: Time evolution of the angular momentum distribution of the electrons within the space bounded by the spherical detector at (a) 44 ps, (b) 58 ps, (c) 85 ps, (d) 129 ps, (e) 234 ps, and (f) 338 ps for $n = 80$. The inserts show the angular momentum distributions of the electrons at corresponding times for the pure electric field case for which the time dependent dynamics is regular.

of the distribution has almost entirely diminished, leaving behind the δ part from which the second peak in Fig. 6.1(c) is about to emerge. Fig. 6.4(e) and (f) are at $t = 234$ ps and $t = 338$ ps, are the snapshots of the l-distribution further along the chaos induced pulse train in Fig. 6.1(c). Note that these electrons do not go up as high in l as the population that ionized through the direct pulse.

The distribution starting from small l propagates into larger l's and a small part of it reflects back from $l \sim 200$ and moves back to the smaller l. This oscillation of l between the small and the large angular momenta continues until after the second pulse and the entire population more or less localizes to $l \lesssim 100$. Also notice that in the pure electric field case the irregular features of the l-distribution is absent and the ionization is regular.

6.3.3 Angular distribution of the ionizing pulse trains on the detector

Fig. 6.1 shows very good agreement between our classical and quantum mechanical calculations. Note that they show the current that reaches the detector integrated over the surface of the spherical detector. A more detailed look at the distributions of the electrons at the detector surface reveals differences between the classical and quantal pulse trains. Fig. 6.5 shows the time evolution of $|\psi|^2$ on the surface of the spherical detector as a function of θ. The angle θ spans the range $[\pi - \pi/6, \pi + \pi/6]$ for better visualization of the current through the spherical cap. The figure is for $n = 80$ and shows results obtained by both quantum mechanically (solid curves) and classically (dotted curves). Fig. 6.5(a) shows the angular distribution on the detector at $t = 85$ ps, just when the electrons are escaping through the direct pulse in Fig. 6.1(c). Note that all the probability density is

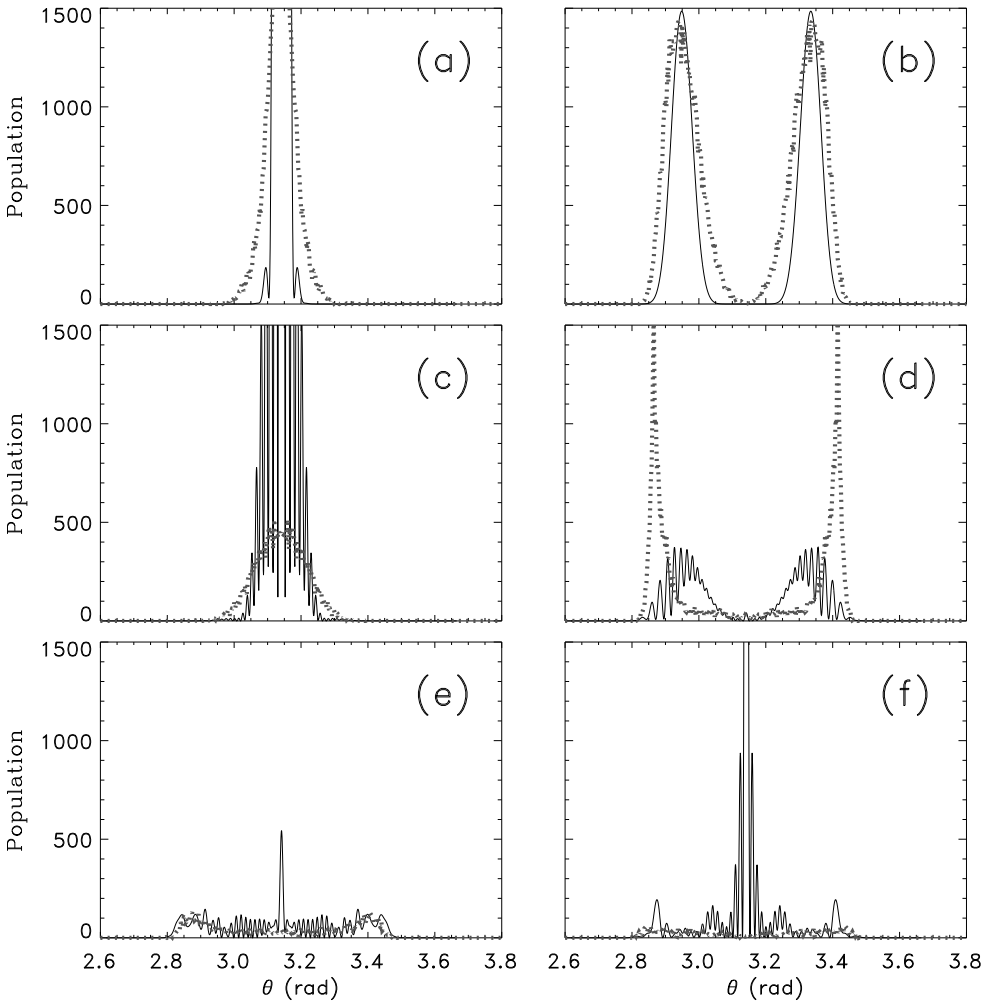

Figure 6.5: Time evolution of the classical (dotted curve) and quantum (solid curve) angular distributions of the electrons hitting the detector at (a) 85 ps, (b) 107 ps, (c) 151 ps, (d) 173 ps, (e) 289 ps, and (f) 347 ps for $n = 80$.

localized around $\theta = \pi$ since these are the electrons that were originally launched directly downhill. Figs. 6.5(b) and (c) show the angular distribution on the detector at $t = 107$ ps and $t = 151$ ps, at the beginning and the end of the knee of the direct pulse. In Fig. 6.5(b), there are no electrons at $\theta = \pi$ and all of the wave function is hitting the detector at $\sim \pi \pm 0.2$ rad, forming a ring that is centered at the point where the z-axis goes through the spherical detector. In Fig. 6.5(c), the two peaks in (b) come together at $\theta = \pi$. The quantum mechanical peaks interfere whereas the classical peaks simply rejoin without interference. The fact that the peaks in In Fig. 6.5(b) come together is a manifestation of the cyclotron motion the electrons perform as they approach the detector. In Fig. 6.5(d) is at $t = 173$ ps, during the second peak in the pulse train. Note that again the wave function arrives at the detector in two peaks as in (b), but this time quantum mechanical peaks show interference even though the peaks are separated. The classical distribution in this case is sharper than that of Fig. 6.5(b) meaning that the trajectories that give rise to the second pulse have a sharper distribution of launch angles.

Finally, Figs. 6.5(e) and (f) show the angular distribution on the detector at $t = 289$ ps and $t = 347$ ps. These are the distributions of electrons on the detector that escape after the second pulse. Note the interference patterns of the quantum mechanical distributions are much more complicated and intricate than those of the direct and the second pulses. This points out that the quantum mechanical distribution shows more and more interference as the pulse train grows longer which is in agreement with our discussions regarding the time-dependent wave function in Sec. III A. Even though the quantum mechanical and the classical distributions depicted in Fig. 6.5 show fine structural differences due to quantum

interference, the effect of the interference in the total current through the sphere is washed out when the current density is integrated over the surface of the detector. This results in the very well agreeing classical and quantum mechanical time-dependent currents seen in Fig. 6.1.

6.3.4 Effect of the angular distribution of the source term

In the quantum mechanical calculations we have presented so far, the initial electron wave packet has been chosen to be spherically symmetric. Furthermore, the CTMC results have also assumed a flat distribution of the launch angle of the trajectories. This allowed us to include all the possible trajectories that can be launched in our simulations. As discussed in Sec. III A, previous classical calculations [77] and Fig. 6.2 suggest that the angle at which a trajectory is launched ultimately defines its time of escape. Therefore, the launch-angular distribution of the trajectories in the classical calculations, or the angular distribution of the initial wave packet in our quantum mechanical calculations determine the shape of the ionization pulse train.

In this section, we explore the effect of the angular distribution of the initial wave packet in the quantum mechanical calculations on the structure of the ionization pulse trains. In the classical case, the launch angle distribution of the trajectories determine the relative heights of the peaks in the pulse train which means that the angle at which a trajectory is launched is directly related to its ionization dynamics. For example, the electrons launched from $\theta = \pi$ would be expected to ionize via the direct pulse whereas an electron launched initially uphill, i.e. $\theta < \pi/2$, would escape at a relatively later time via

one of the later pulses in the pulse train. This suggests that eliminating certain trajectories from the CTMC calculations that give rise to ionization through a certain pulse in the pulse train may give us the ability to manipulate the structure of the pulse train. This can be realized classically by finding the angular range which spawns the trajectories that escape via a given pulse and excluding these angles from the classical launch angle distribution. In our quantum mechanical calculations, this would correspond to placing a node in the angular distribution of the initial wave packet.

We have particularly attempted to eliminate the second pulse in Fig. 6.1(c) for $n = 80$. To eliminate this second pulse we needed to know classically at what angle a trajectory must be launched to contribute to this pulse in the train. This was done by binning the trajectories that reached the detector between 158 ps and 213 ps in angle. The result is seen in Fig. 6.6(d) as a function of the classical launch angle. The angular range from which a trajectory must originate to contribute to the second pulse is a fairly sharp distribution with a smaller secondary peak. The main peak is centered at $\theta \sim 2.0$ rad whereas the secondary peak is located at $\theta \sim 2.2$ rad. Comparing with Fig. 6.2, we realize that these peaks correspond to the escape segments **A1** and **A2** in the escape-time plot, which are responsible for the second and the third peaks in the classical calculations of Mitchell *et al*. Restricting the launch angles of the classical trajectories to outside of this range in the CTMC calculations should therefore eliminate the second peak in the pulse train. The same should also be true in our quantum mechanical calculations if we place a node at the peak of the angular distribution of Fig. 6.6(d) in the angular distribution of the initial wave packet.

Placing a node in the angular distribution of the source term in our quantum mechanical calculations physically corresponds to superposing a p-wave onto our otherwise s-wave initial wave packet or source term. The radial part of the zero energy solution to the Schrödinger equation for the hydrogen atom is [82]

$$R_{\infty,l}(r) = \frac{A}{\sqrt{2r}} J_{2l+1}(\sqrt{8r}) \tag{6.19}$$

where J_{2l+1} is the Bessel function of order $2l+1$, and A is a normalization constant. Therefore, to introduce a node in the wave packet, we superpose a p-wave source $S_1 = \delta_{l,1} r(1-r/2)e^{-r/2}$ with an s-wave source S_0 (see Eq. (6.7)) via a mixing coefficient a.

$$\left(\int_0^\infty S_0 J_1(r)dr\right) J_1(r)Y_0^0 + a\left(\int_0^\infty S_1 J_3(r)dr\right) J_3(r)Y_1^0 = 0. \tag{6.20}$$

The zero of this superposition for a given angle θ_0 in Y_1^0 yields the mixing coefficient a. The integrals in Eq. (6.20) can be evaluated by standard techniques to give an exact result. For the Bessel functions $J_1(r)$ and $J_3(r)$ outside the integrals we have used the asymptotic form of the Bessel function retaining only its outgoing wave part, i.e.,

$$J_m(z) \sim \sqrt{\frac{2}{\pi z}} e^{-i(z-m\pi/2-\pi/4)} \quad (z >> |m^2 - 1/4|). \tag{6.21}$$

Solving Eq. (6.20) for a, we have found that the mixing coefficient for which there is a single node at $\theta = \theta_0$ is $a = -1.47/\cos(\theta_0)$.

Superposing higher angular momentum components can help making the node sharper. Such a wave packet may be experimentally tailored by first exciting a ground state hydrogen to a low-n state in an external electric field. The fact that the electric field mixes states with $l \pm 1$ gives rise to Stark oscillations in the l-distribution. This forms a Stark wave packet, which then can be excited to a Rydberg wave packet via a second laser pulse. Hitting this Stark wave packet at the right time would enable one to control the l-distribution of the initial wave packet at the time of its launch to the Rydberg wave packet. For instance, exciting the ground state up to a wave packet within the $n = 2$ manifold results in a wave packet composed of $l = 0$, 1, and 2 angular momentum components, mixed in a time-dependent fashion. Hitting this wave packet with the second laser pulse at the right moment would launch it with a desired superposition of $l = 0$, 1, and 2 states to a high-n Rydberg wave packet. Since the Stark period would be longer compared to the period of the laser pulse, with the proper timing of the second laser pulse, a desired nodal pattern can be achieved for the initial wave packet.

To eliminate the second pulse in Fig. 6.1(c), we have excluded the launch angles in the range [1.8,2.4] rad in our CTMC calculation and placed a node at $\theta = 1.9$ rad in the angular distribution of the source term in the quantum mechanical wave packet calculation. The results are the dotted curves in Fig. 6.6(a) and (b) for quantum and classical calculations respectively. Clearly excluding the entire range of angles that make up the peaks in Fig. 6.6(d) does not only remove the second pulse in Fig. 6.1(c), but knocks out the entire pulse train after the direct ionization pulse. This means that the excluded angular range does not only give rise to the electrons that escape through the second pulse of electrons

but also includes almost all the other trajectories that escape afterwards within the time range we explore. This is in accord with the previous classical calculations of Mitchell *et al.* [76, 77] since the angular range we excluded is actually larger than the entire range they explored and resolved for particular peaks in the pulse train. The fact that the direct pulse remains intact in this case is expected since it is mainly risen by the trajectories that are launched directly downhill, i.e. $\theta = \pi$.

Instead of removing the entire angular range that make up the peak in Fig. 6.6(d), we tried to remove smaller ranges of the classical launch angle θ within this peak. Results of these classical calculations can be summarized by the set of curves in Fig. 6.6(b).

a. *Allowing the full* $[0, 2\pi]$ *range for the launch angles in the classical calculations gives the solid curve in Fig. 6.6(b). This is the case investigated previously.*

b. *Excluding a thin slice from the center of the angular distribution depicted in Fig. 6.6(d), i.e. the range* $[1.998, 2.035]$ *rad, gives the dashed curve of Fig. 6.6(b). In this case, the second peak has gotten smaller and the rest of the pulse train remains intact.*

c. *Excluding a large slice of launch angles from the peak in Fig. 6.6(d) such that only the small secondary peak is left gives the dash-dotted curve of Fig. 6.6(b). Note that the second peak has now completely disappeared along with the later pulses in the pulse train except a large fraction of the third pulse. Comparing with the case in which the entire peaks in Fig. 6.6(d) were excluded (dotted curve), this suggests that the small secondary peaks in the launch angular distribution is almost entirely responsible for the third pulse in the pulse train.*

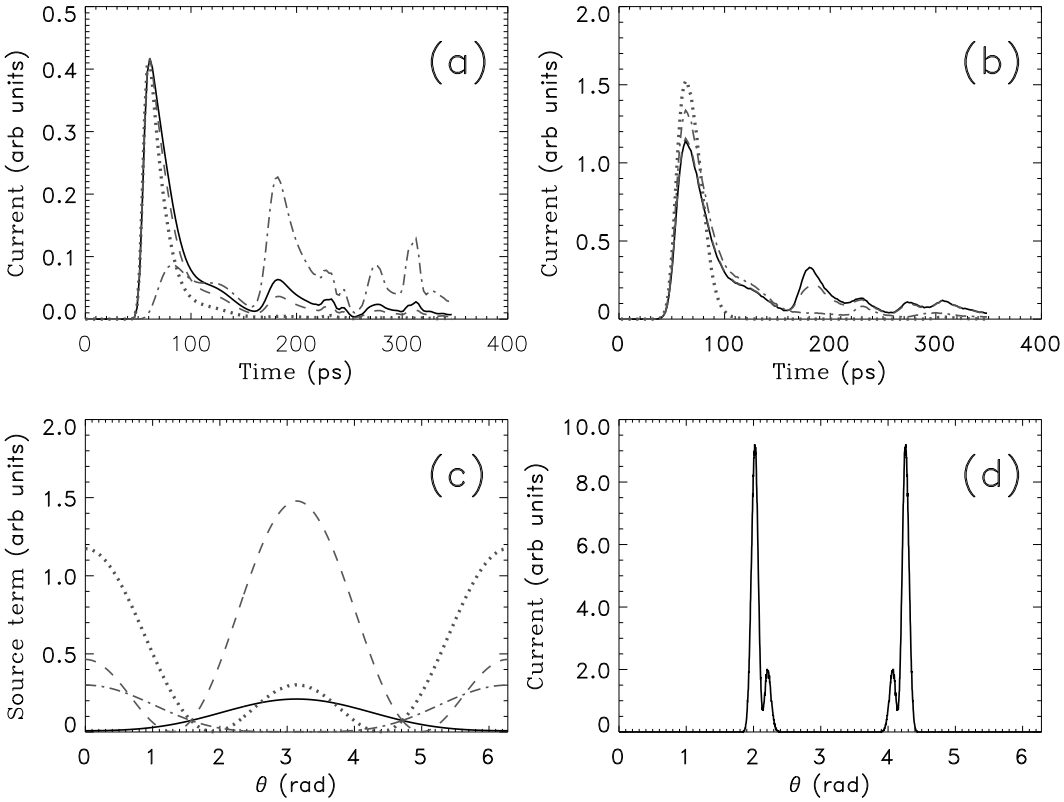

Figure 6.6: (a) Current-time plots from quantum mechanical wave packet calculations for various angular distributions of the source term. All the angular distributions we tried have at most a single node in the angular range $[0, \pi]$ and are plotted as a function of θ in (c). The solid curve has no nodes whereas the dash-dotted curve has node at $\theta = \pi$ rad, dashed curve at $\theta = 1.28$ rad, and the dotted curve at $\theta = 1.9$ rad. Figure (b) shows ionization current from the CTMC calculations for various exclusions from the angular range of the launch angle shown in (d). The solid curve allows this entire range whereas the dotted curve completely excludes it from its allowed launch angles. The dash-dotted and dashed curves are obtained by excluding the angular ranges $[1.8, 2.123]$ rad and $[1.998, 2.035]$ rad from the distribution shown in (d).

To simulate the same effect in our quantum calculations, we placed nodes at various angles in the angular distribution of the source term, i.e. the initial wave packet. Fig. 6.6(c) shows several angular distributions we have tried and the resulting current-time plots make up Fig. 6.6(a). Same line-styled curves in Fig. 6.6(a) and (c) correspond to each other.

a. *The solid curve in Fig. 6.6(a) corresponds to the angular distribution depicted by the solid curve in Fig. 6.6(c) with no nodes and a maximum at $\theta = \pi$ rad. This angular distribution reproduces the current-time curve in Fig. 6.1(c) almost exactly.*

b. *The dash-dotted curve in Fig. 6.6(a) has an angular distribution with a node at $\theta = \pi$ rad as seen in Fig. 6.6(c). This knocks out the direct pulse in Fig. 6.1(c) as expected since this is classically equivalent to removing the first prominent escape segment in Fig. 6.2(b).*

c. *The dashed curve of Fig. 6.6(a) is calculated using an angular distribution with a node at $\theta = 1.28$ rad which corresponds to the angular distribution in Fig. 6.6(c) with the same line style. Notice the direct pulse in this case remains unchanged while the second pulse is clearly reduced. This is because the node is not placed exactly at the center of the main classical peak in Fig. 6.6(d) but it is close enough such that it partially knocks it out.*

d. *When we place a node at $\theta = 1.9$ rad, at the center of the classical peak in Fig. 6.6(d), we get the dotted curve in Fig. 6.6(a). This kills off the entire pulse train following the direct pulse as in the classical case shown with the dotted curve in Fig. 6.6(b).*

Classically this is same as killing off the escape segments labeled as **A1** *and* **A2** *in Fig. 6.2(b).*

To sum up, we find that we can diminish the pulse train as much as we want by sliding the node within the classically calculated peaks of Fig. 6.6(d). We were also able to remove the direct ionization pulse by placing a node at π. This is physically identical to killing off the trajectories that were classically launched directly downhill. Elimination of the pulses by inserting nodes in the angular distribution of the quantum mechanical initial wave packet would be more clear and isolated from the neighboring pulses if the corresponding classical escape segments in Fig. 6.2(b) were to span wider angular ranges.

6.3.5 Effect of core scattering

We have already pointed out that in the presence of a pure electric field, the hydrogen atom ionizes only via a direct pulse due to the absence of a core. In the presence of a core, the direct ionization peak is followed by an irregular train of ionizing electrons due to the part of the wave function which did not directly ionize but initially headed uphill, turned around by the uphill potential and then scattered in all directions by the core electrons [83]. Non-hydrogenic atoms in external electric fields have also been found to show statistical properties in the nearest neighbor spacings that is neither regular nor chaotic suggesting that the dynamics is somewhere in between [84]. Therefore introducing a core into our problem may reveal interesting features attributable to the coupling between these two different dynamics.

We incorporated the core electrons into our calculations through a model potential. Instead of modeling a real atom using a model potential with proper quantum defects, it is more informative to use a model potential of the form $Ce^{-r/a}/r$. Playing with the parameters C and a we can control the range of the core potential. This allows us to control the extent of the core penetration by the electron.

Fig. 6.7(c) and (d) shows potentials for $C = -1$ and two different values of a along with the field free potential of the hydrogen atom for $l = 0$, 1, and 2. Values used for a are 0.05 and 0.5 for Fig. 6.7(c) and Fig. 6.7(d) respectively. The model potentials are plotted as the solid curves whereas the field free hydrogenic potentials are the dotted, dashed, and dash-dotted lines for $l = 0$, 1, and 2, respectively. Notice that in case of $a = 0.05$ the model core potential is buried deep below the angular momentum barrier even for the lowest angular momentum considered, i.e. $l = 0$. It is natural to expect the core potential to have no effect on the ionization dynamics in which we are interested, and this is indeed the case. The fully quantal ionization pulse train for this case is the solid curve in Fig. 6.7(a). Same case within our CTMC model is again the solid curve in Fig. 6.7(b). Both classical and fully quantal computations yield exactly what was seen for hydrogen in Fig. 6.1 due to the inability of the electron to penetrate into the core region. Increasing a to 0.5 we extend the range of the core potential beyond the $l = 1$ potential barrier and obtain dotted curves in Fig. 6.7(a) and Fig. 6.7(b) using quantum mechanical and CTMC methods respectively. Fig. 6.7(a) also shows the pure electric field case for $a = 0.5$ (dashed curve). Contrasting the solid curve with the dotted curve in Fig. 6.7(a) we can tell that the addition of the core potential that extends beyond the $l = 1$ potential barrier enhances the pulses that come after

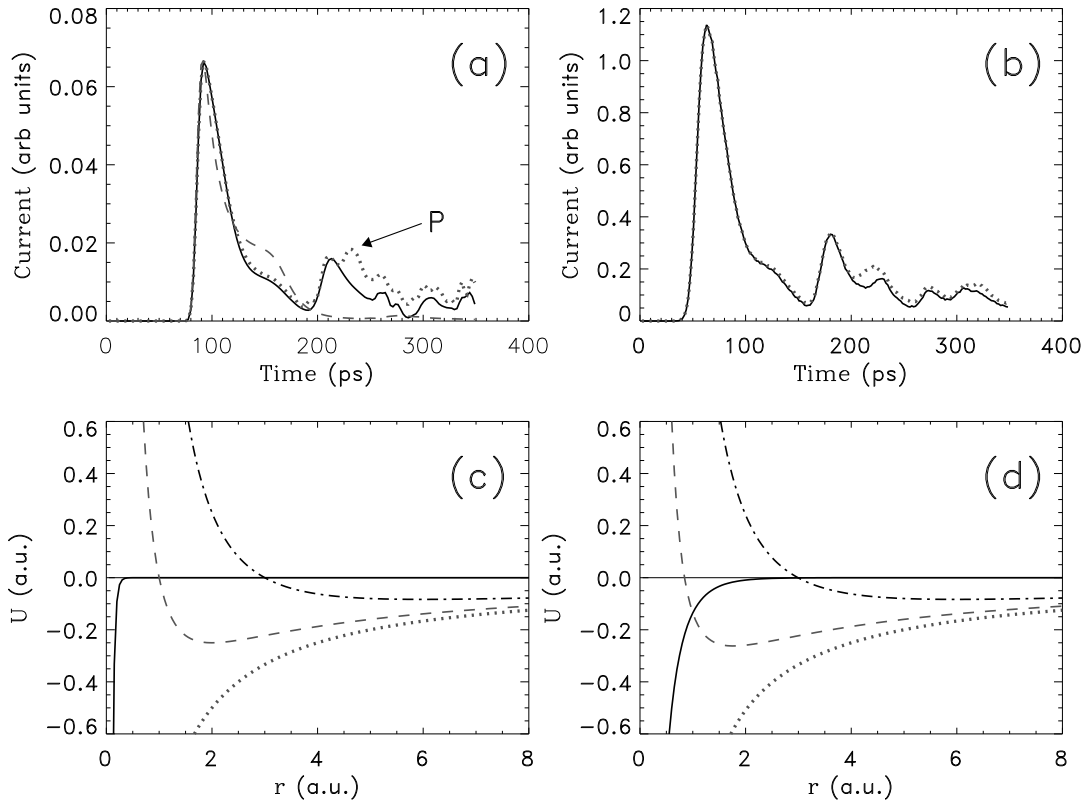

Figure 6.7: Quantum mechanical (a) and classical (b) current-time plots with the inclusion of core scattering. In (a) the solid curve is for $C = -1$ and $a = 0.05$ and the dotted curve is for $C = -1$ and $a = 0.5$. The dashed curve shows the pure electric field case in the absence of chaos. In (b) again the solid curve is for $C = -1$ and $a = 0.05$ and the dotted curve is for $C = -1$ and $a = 0.5$. The difference is less prominent compared to the quantum mechanical case in (a). (c) and (d) show the model core potentials curves (solid lines) and the field free atomic potential curves for $l = 0$, 1, and 2 for $a = 0.05$ and $a = 0.5$ respectively. All the calculations are for $n = 80$.

the second pulse in the train with an additional pulse of electrons dwelling on the skirt of the second pulse (marked as P). This new pulse is absent in the classical calculation in Fig. 6.7(a) suggesting that it is due to interference between the parts of the wave function that scatters from the core and the part that is escaping due to chaotic nature of the time-dependent dynamics.

6.3.6 Transition to regularity - the case of high magnetic fields

Transition from regular to chaotic dynamics in open atomic systems has been extensively studied in the energy domain for the diamagnetic Kepler problem and ionization of Rydberg atoms in external microwave fields. In the latter system, as the microwave frequency is varied from low to high, the dynamics pass through three distinct dynamical regimes of ionization. With the definition of a scaled frequency $\Omega_0 = \Omega n^3$ (the ratio of the microwave frequency Ω to the Kepler frequency of the Rydberg state $1/n^3$) microwave ionization in these regimes are categorized as the tunneling, chaotic and the multiphoton ionization regimes. In the diamagnetic Kepler problem, introduction of a scaled parameter $\eta = E/\gamma$ transforms this problem into a problem of two coupled two-dimensional harmonic oscillators where the coupling strength is quantified by η. By changing η, or equivalently changing magnetic field strength γ for fixed energy E, transition from regularity to chaos is observed by studying the statistical distributions of the nearest neighbor energy level spacings [85].

Due to the scaling properties of the classical Hamiltonian of the diamagnetic Kepler problem, the dynamics of the electron does not depend on the energy of the electron and

the magnetic field independently, but rather depend on a scaled energy $E_c = E/\gamma^{2/3}$ [86]. Several properties of the diamagnetic Kepler problem has been studied by fixing the scaled energy E_c such as the quasi-Landau modulations in the photoabsorption spectra of diamagnetic hydrogen. So far in our study of the ionization of diamagnetic hydrogen in uniform electric field, we have only considered a single ionization regime and observed signatures of chaos in the current, wave functions, and angular momentum distributions of the ionized electrons. This dynamical regime corresponds to $E_c \approx 0.48$ for all the energies and magnetic field strengths we have considered in previous sections.

We now will study different field regimes with different scaled energies while keeping the energy E and the electric field strength fixed. We particularly consider the $n = 80$ case and the scaled energies $E_c = \alpha^{-2/3}(E/\gamma^{2/3})$ with $\alpha = 0.5$, 1.0, 2.0, and 4.0 where $\alpha = 1.0$ being the case we have studied in Sec. III A. These scaled energies simply correspond to magnetic field strengths of $\alpha\gamma$, i.e. $B = 0.245$ T, $B = 0.49$ T, $B = 0.98$ T, $B = 1.96$ T respectively, and $E = 1/(2n^2) = 7.8 \times 10^{-5}$ (a.u.) and $F = 19$ V/cm. The current-time plots we have obtained are plotted in Fig. 6.8(a), (b), (c), and (d) in increasing magnetic field strength, i.e., α. Each plot shows quantum mechanical wave packet and CTMC results on top of each other for comparison. In case of $\alpha = 0.5$ of Fig. 6.8(a), the time-dependent ionization dynamics appears regular. This is expected since for a weak enough magnetic field the dynamics is dominated by the external electric field and the magnetic field has little effect. The case of the pure electric field gives a single ionization pulse as discussed before leading to the prominent direct pulse in Fig. 6.8(a) with no further escape at later times. The regularity in this case is a direct consequence of the integrability of the system

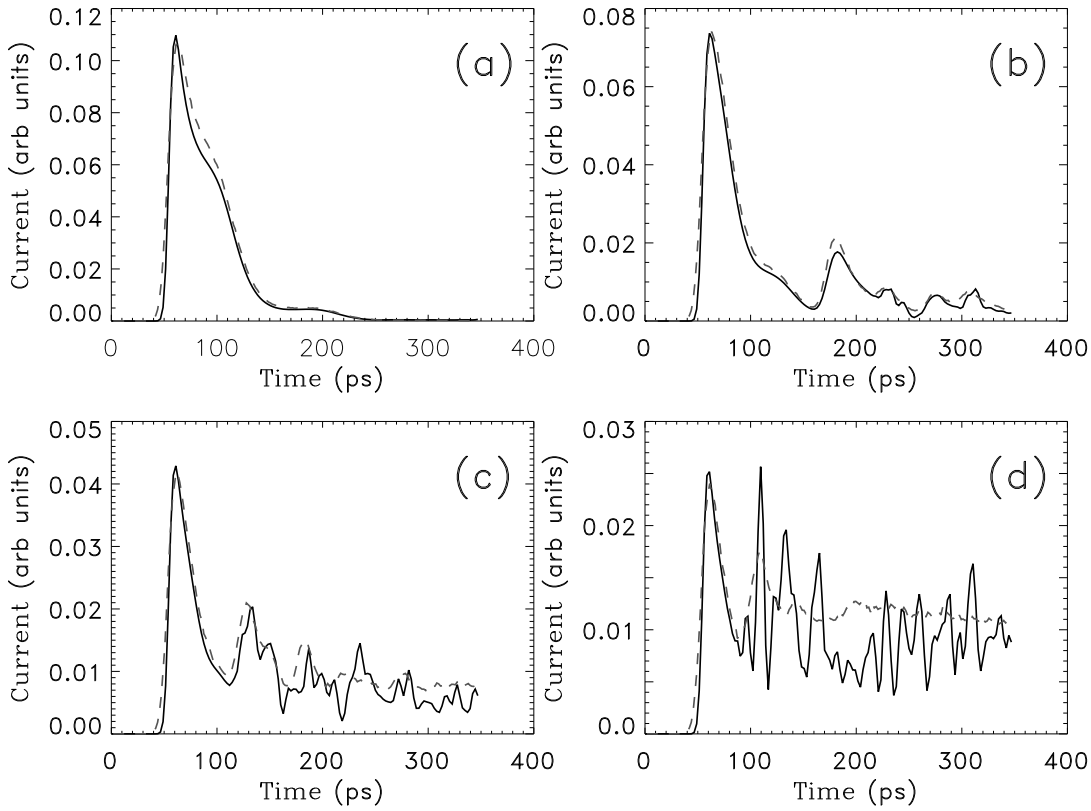

Figure 6.8: Quantum mechanical (solid curves) and classical (dashed curves) current-time plots for four different scaled energies quantified by α; (a) $\alpha = 0.5$, (b) $\alpha = 1.0$, (c) $\alpha = 2.0$, and (d) $\alpha = 4.0$. All the calculations are for $n = 80$.

due to the separability of the classical equations of motion and the agreement is perfect between the CTMC and the quantum mechanical calculations. Fig. 6.8(b) is the case for which $\alpha = 1.0$ which is what we have considered in Sec. III A and the ionization is chaotic with very good agreement between the classical and the quantum mechanical current-time plots.

Figs. 6.8(c) and (d) shows the time-dependent current of ionizing electrons for $\alpha = 2.0$ and $\alpha = 4.0$. Notice that the irregular structure of the ionization pulses from the CTMC calculation is getting washed out compared to the $\alpha = 1.0$ case. This is expected since higher the magnetic field closer we are to the Landau regime where the energy levels are becoming similar to those of the harmonic oscillator. Therefore the diamagnetic Kepler problem in a uniform parallel electric field is integrable in this regime since a harmonic oscillator in uniform parallel electric field is integrable. The fact that the Landau regime is integrable leads to regularity in the classical dynamics in this regime as displayed by the dashed CTMC calculations in Figs. 6.8(c) and (d). Transition towards regularity displayed in the CTMC calculations can also be understood in the semiclassical grounds. Volume of a unit phase-space cell is proportional to the inverse of the effective Planck constant divided by 2π, i.e. $1/\hbar_{\text{eff}}$ which scales like $\sim 1/n$ [87]. Instead of increasing the magnetic field strength γ, we might just as well decrease n and maintain the same scaled energy E_c. This would simply increase the volume of the unit phase-space cell, giving rise to blurring and hence washing out of the fine structures in the phase-space, suppressing chaos. In contrast to the classical case, the fully quantum mechanical results show more erratic fluctuations relative to the $\alpha = 1.0$ case. This situation is even more pronounced for the case of $\alpha = 4.0$ in Fig. 6.8(d). Even though the structure of the pulse train in this case gives a strong impression of chaos, these enhanced oscillations in the quantum case does not necessarily point to enhanced chaos. Actually, given the fact that the CTMC calculations suggest transition to regularity in the underlying classical dynamics as α is increased, it can be

concluded that the enhanced fluctuations in the quantum mechanical current-time plot are not due to enhanced chaos but rather are results of a different physical mechanism.

The reason for the enhanced fluctuations for the higher magnetic fields can be understood if one considers how the number of open ionization channels change as the magnetic field is increased. Since we are closer to the Landau regime in the high α (or magnetic field strength) limit, the energy levels are becoming more like the Landau levels. In this case, the energy levels are almost equally spaced by ω_c as for a harmonic oscillator and the separation increases linearly with increasing magnetic field strength. For a fixed electric field strength, the classical ionization threshold is fixed at $-2\sqrt{F}$ and this gives a fixed opening for ionization since the azimuthal symmetry is the dominant symmetry in the system in the Landau regime. Any escaping trajectory must pass through this opening. For $n = 80$ at $F = 19$ V/cm, the energy is $E = -1/(2n^2) \approx -7.8 \times 10^{-5}$ (a.u.) and the classical ionization threshold is $\mathcal{E} = -12.2 \times 10^{-5}$ (a.u.). Therefore the size of the opening is $\Delta W = E - \mathcal{E} = 4.4 \times 10^{-5}$ (a.u.). On the other hand, the Landau level spacing ω_c is 2.09×10^{-6}(a.u.) and 4.18×10^{-6}(a.u.) for $\alpha = 2.0$ and $\alpha = 4.0$ respectively. The ratio $\Delta W/\omega_c$ roughly gives the number of channels available for ionization and is ~ 21 for $\alpha = 2.0$ and ~ 10 for $\alpha = 4.0$. In the quantum mechanical case, the number of ionization channels that fit into this opening therefore decrease with the increasing separation of the equally spaced energy levels. This is what gives rise to the enhanced oscillations in the quantum mechanical current-time plot in Fig. 6.8(d).

One of the interesting phenomena observed for the diamagnetic Kepler problem is the quasi-Landau modulations in the photoabsorption spectrum at the zero-field threshold [88].

These modulations were originally observed to be separated by 1.5 times the Landau spacings for a free electron in magnetic field and are associated by the resonance states which are fairly localized in the plane perpendicular to the external magnetic field. Later wave packet calculations pointed out other Landau resonances with energy spacings of $0.64\omega_c$ [89]. Such quasi-Landau fluctuations were also seen at lower energies and explained in terms of the individual magnetic field states [90]. It was found that it was the highest energy diamagnetic states of the n-manifolds evolved into the Landau states [91]. To see whether such effects occur in our problem, we have evaluated the time-dependent autocorrelation function $C(t)$, and the corresponding spectral autocorrelation function $C(E)$ for the $\alpha = 2.0$ and $\alpha = 4.0$ cases of Fig. 6.8. The real part of $C(t)$ for each case is plotted as the solid curves in Figs. 6.9(a) and (b) respectively. The solid curves are obtained from the autocorrelation functions by smoothing them via boxcar averaging. Inserts in the figures show $C(t)$ near $t = 0$. Notice in the $\alpha = 2.0$ case there are clearly two modes of oscillation in the autocorrelation function; the thick oscillation modulated by much narrower fluctuations in time. Both types of oscillations correspond to revivals of particular pieces of the wave function and manifest themselves in the spectral autocorrelation functions $C(E)$ in Figs. 6.9(c) and (d). The spectral autocorrelation function $C(E)$ in our case roughly corresponds to the photoabsorption spectrum. In the spectral autocorrelation functions the frequency axis is shifted by $1/(2n^2)$ such that 0 frequency corresponds to the $n = 80$ component.

Both types of the oscillations depicted in Fig. 6.9(a) for $n = 80$ are due to the localized part of the wave function labeled as σ in Fig. 6.3(b), which is the Stark oscillating

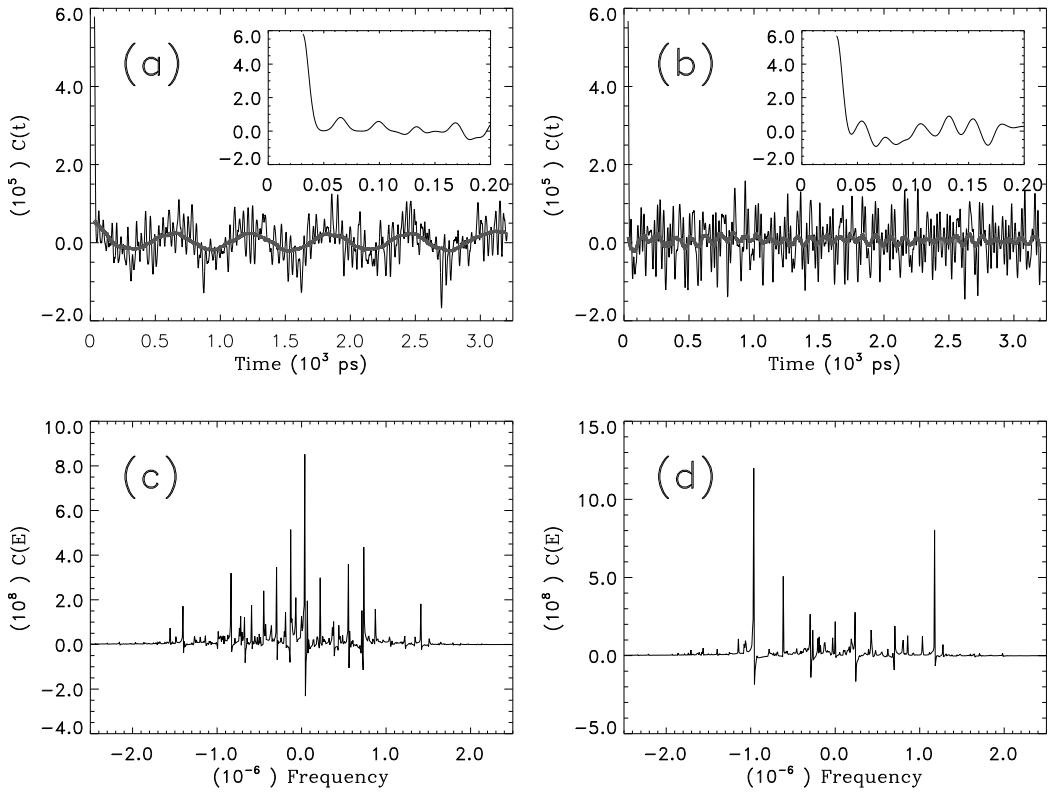

Figure 6.9: Time-dependent autocorrelation functions for (a) $\alpha = 1.0$ and (b) $\alpha = 4.0$. (c) and (d) are the spectral autocorrelation functions that correspond to (a) and (b) respectively. The time-dependent autocorrelation functions clearly show two types of oscillations whereas the spectral autocorrelation functions show equally spaced resonances which indicates Landau quantization.

part of the wave function. In particular, the revival time of the sharper oscillations modulating the oscillations depicted by the thick curve in Fig. 6.9(a) is $t_{\rm rev}^{(1)} \sim 40$ ps as can be seen from the insert. The revival time of the oscillation shown by the thick curve for the same scaled energy is $t_{\rm rev}^{(2)} \sim 600$ ps. These revival times correspond to energy spacings of $\Delta E_{\rm rev}^{(1)} = 2\pi/t_{\rm rev}^{(1)} \sim 3.8 \times 10^{-6}$ (a.u.) and $\Delta E_{\rm rev}^{(2)} = 2\pi/t_{\rm rev}^{(2)} \sim 0.25 \times 10^{-6}$ (a.u.). The spacings between the pronounced resonances of Fig. 6.9(c) have a spacing of $\sim 0.2 \times 10^{-6}$ (a.u.) which roughly corresponds to $\Delta E_{\rm rev}^{(2)}$. We do not see any resonances with spacings corresponding to $\Delta E_{\rm rev}^{(1)}$ for this is almost as wide as the frequency range spanned by the resonances in Fig. 6.9(c). The spectral autocorrelation functions seen Figs. 6.9(c) and (d) clearly show equally spaced resonances, much like the energy levels of a harmonic oscillator. This is due to the Landau quantization at the scaled energies we consider in Fig. 6.9. Number of such equally spaced resonances in Figs. 6.9(c) and (d) can be counted to be ~ 15 and ~ 8 respectively, which roughly agrees with the number of the ionization channels we have estimated above. The decrease in the number of Landau states is roughly a factor of two as would be expected, since the level spacing ω_c in the Landau regime linearly scales with the magnetic field strength, and the scaled energies considered in Figs. 6.9(a,c) and (b,d) are $\alpha = 2.0$ and $\alpha = 4.0$. Although we observe Landau states in the spectral autocorrelation function, we do not see any clear sign of quasi-Landau oscillations.

6.4 Conclusions

In this paper, we examined ionization of a hydrogen atom excited to a Rydberg state via a short laser pulse in parallel electric and magnetic fields. The field regime we have been

interested in is the one for which the classical dynamics of this system displayed chaos in the time domain as reported in Refs. [76, 77]. Since physical roots of irregular scattering is obscure and ill defined on purely quantum mechanical grounds, we tried to explore the time-dependent dynamics of ionization from this system using a non-perturbative quantum mechanical wave packet method along with a CTMC method.

Comparing quantum mechanical and classical results from these calculations, we observed quantum mechanical effects, which would be absent in the classical picture, such as interference effects. We have been able to reproduce chaos induced pulse trains of ionization, previously observed in classical calculations [76, 77]. We found very good agreement between our quantum mechanical and classical calculations of the ionization current in the time domain for high Rydberg states with $n = 40$, 60, and 80. Looking at the time-dependent wave function of the system, we have observed flux of electrons that ionize through different pulses in the ionization pulse train and connected certain parts of the wave function with the classically observed escape segments in the classical time-dependent launch angle distribution of Ref. [77], which we have included in our paper as Fig. 6.2. We have found that as the ionization pulse train grows longer, the number of escape segments that contribute to a given pulse in the pulse train increases which ultimately leads to interference between different escape channels in the quantum mechanical wave function. We have also observed these interference patterns on the surface of our spherical detector which confirmed the observation of previous classical calculations suggesting that the launch angle of a classical trajectory determines the time of the electron's escape, giving rise to a train of pulses in the time dependent ionization current. Although the total

ionization current, which is obtained by integrating the current density through the surface of the spherical detector, from the classical and the quantum mechanical calculations agree very well, this does not mean that the classical and the quantum mechanical pictures does not differ from one another. The main difference is the quantum interference discussed in Sec. III C, whose effect on the current gets washed out when the current density is integrated through the surface of the detector. Another difference between the classical and the quantum mechanical pictures is that the classical picture lacks the phase information which is incorporated into the quantum calculations through the time propagation operator. A semi-classical modeling of this problem could shed light into the question of how important the the phase information omitted is in the classical calculations.

This angular dependence of the shape of the suggested that it was possible to tailor the shape of the pulse train by using a proper angular distribution of the initial wave packet. In an attempt to manipulate the structure of the ionization pulse train, we ran CTMC simulations to figure out in which angular range a trajectory must be launched to contribute to the second pulse in the pulse train. Excluding this range of angles from the launch angular distribution in the CTMC calculations, we have eliminated pulses from our classical time-dependent ionization current. We further placed nodes at corresponding angles in the angular distribution of the initial wave packet in our quantum mechanical wave packet calculations, and successfully removed the second and the prominent direct pulses from the pulse train.

We have also investigated the angular momentum distributions of the electrons inside the region bounded by our spherical detector. We were able to recognize the part of the l-distribution that corresponds to the direct ionization pulse which extended up $l \sim 200$. This part of the distribution almost completely diminishes after the direct pulse terminates and the small fraction of the remaining decays away slowly since the prominent escape segment in the classical escape-time plot seen in Fig. 6.2(b) contributes to all the later pulses in the pulses train. We found that the angular momenta of the electrons escaping through the later pulses are confined to smaller l's than those escape through the direct pulse.

Inclusion of core scattering into our problem allowed us to study the extent to which the core penetration of the electron can affect the structure of the chaos-induced pulse train. We used a model core potential to allow $l = 0$ and $l = 1$ core penetrations of the electron. We reproduced our previous hydrogenic results for the $l = 0$ case as would be expected, and observed enhancements in the pulses that came after the second pulse in the pulse train for the $l = 1$ case. This enhancement of the pulses was more prominent in our quantum mechanical simulations than in our CTMC simulations.

To study the transition from chaotic dynamics to regularity in this system, we varied scaled energy of the system and found that for high scaled energy, i.e., high magnetic field, the approach to the Landau regime resulted in the transition to regular regime in the classical dynamics implied by the suppression of chaotic structure of the ionization pulse train. On the other hand, our quantum mechanical calculations showed enhanced oscillations in the current-time plot in this field regime. We have concluded that this was due to the decrease in the number of open ionization channels in the quantum case. Looking

at the time-dependent autocorrelation function, we were able to see revivals of the Stark oscillating part of the time-dependent wave function and the resonances that correspond to them in the spectral autocorrelation function. We observed equally spaced resonances in the spectral autocorrelation function which we believe to be due to the Landau quantization in the strong magnetic field strengths we consider. Despite the apparent existence of the Landau quantization in the spectral autocorrelation function, we see no clear signatures of quasi-Landau oscillations.

CHAPTER 7

SUMMARY

In this work, we have studied various fundamental atomic processes regarding highly excited one- and two-electron atoms. These processes include photo-double ionization, electron-impact ionization, and radiative cascade and chaotic ionization in static external fields. The primary tools we have used in these studies were based on solving the time-dependent Schrödinger equation in a non-perturbative manner, and we have made comparisons with perturbative calculations as well as purely classical results where possible.

After developing fundamentals of the numerical time-dependent techniques we use throughout this work in Chapter 2, we have first studied the photo-double ionization of helium atom from ground and the first excited state $1s2s(^1S)$ near double ionization threshold to investigate the threshold behavior of the double ionization probability just above the threshold. We have contrasted our results with the predictions of classical theories of Wannier and Temkin, which predict a smooth power law and an oscillating but monotonically increasing law for the threshold behavior of the double ionization cross section near threshold. We have found excellent agreement with our results and the prediction of the Wannier law and did not observe any oscillations modulating the ionization probability as were predicted by the Temkin's Coulomb-dipole theory and observed in the experiments of Wehlitz *et al* [24] and Lukič *et al* [25].

Then in the fourth chapter we have turned our attention to the electron-impact ionization of hydrogen-like Rydberg atoms, where we have reported results from collinear

time-dependent close-coupling (TDCC), distorted-wave (DW), and R-Matrix with pseudo states (RMPS) calculations for the electron-impact ionization of H-like ions up to $Z = 6$ within an s-wave model. We compared the results of these calculations with those from a collinear classical trajectory Monte Carlo (CTMC) calculation to investigate the correspondence between the quantal and classical ionization probabilities as the principal quantum number of the initial state increases. We studied the ionization probability from the ground state and highly excited states up to $n = 25$ as a function of incident energy and the charge of the ion. We have found that the fully quantal ionization probability converged to the classical results rapidly for hydrogen whereas the higher ion stages exhibited much slower convergence with respect to n. We have observed good agreement between the DW and TDCC for the n range we have considered for B^{4+}. For hydrogen, we have found fairly good agreement between the DW and TDCC for the ground state, but the worsening disagreement with increasing n. There was reasonable agreement between the results from the collinear R-Matrix calculations and the results from the TDCC calculations confirming the convergence of the TDCC results.

In the fifth chapter, we have studied the radiative decay of atomic hydrogen in strong magnetic fields of up to 4 T, which is believed to be an important process taking place in the anti-hydrogen experiments. We have followed the radiative cascade from completely ℓ, m mixed distributions of highly excited states as well as from distributions that involve highly excited states with $|m| \sim n$. We have found that the time it takes to populate the ground state is not affected by the magnetic field for the initial states with $n \lesssim 20$. For higher n-manifolds, the electrons in the most negative m states were substantially slowed

down by the magnetic field resulting in a much longer lifetime. We have showed that less than 10% of the anti-hydrogen atoms with $n \sim 35$ generated in anti-hydrogen experiments at 4 K would decay into their ground states before they hit the wall of the vacuum container unless they are trapped. We have also found that the decay time was mainly determined by the fraction of the atoms that were initially in the highest negative m states due to the fact that only $|\Delta m| + |\Delta \pi| = 1$ transitions are allowed in the magnetic field. We have given a semiclassical method for calculating the decay rates for circular states and showed that when the initial states have high-$|m|$, semiclassical decay rates agree with the full quantum mechanical rates within couple of percent for states with effective $n \gtrsim 20$.

Finally, we presented results of our simulations of the ionization of a hydrogen atom excited to a Rydberg wave packet in the presence of external parallel electric and magnetic fields. This is an example of an open, *quantum* system whose classical counterpart has been shown to display chaos in the time domain. Within the framework of classical mechanics, electrons escape through chaos induced pulse trains. We reproduced such previously observed signatures of classical chaos in the time-dependent current of ionizing electrons and studied the interference effects between the outgoing pulse trains which is absent in the classical picture. Our attempts at manipulating the ionization pulse trains and the effect of core scattering coupled with the chaotic ionization were also discussed. We further investigated the onset of chaos as a function of the scaled energy of the system. We found that for relatively high magnetic fields, quantum mechanical ionization current shows erratic fluctuations in contrast with the classical current which shows transition to regularity. We concluded that the oscillations result from the decrease in the number of

the ionization channels for the higher magnetic field strengths. We further studied the time-dependent autocorrelation function and its Fourier transform to look for the effects of the Landau quantization in the photoabsorption spectrum and did not observe any clear signatures of the quasi-Landau oscillations. Our results included calculations via classical trajectory Monte Carlo method to compare our non-perturbative quantum mechanical results with the underlying chaotic classical dynamics.

BIBLIOGRAPHY

[1] "Electron Impact Ionization of Sodium Rydberg Atoms below 2 eV", K. Nagesha and K. B. MacAdam, Phys. Rev. Lett. **91**, 113202 (2003).

[2] "Atomic data for modelling fusion and astrophysical plasmas", H. P. Summers, N. R. Badnell, M. G. O'Mullane, A. D. Whiteford, R. Bingham, B. J. Kellett, J. Lang, K. H. Behringer, U. Fantz, K-D Zastrow, S. D. Loch, M. S. Pindzola, D. C. Griffin and C. P. Ballance, Plasma Phys. Control. Fusion **44**, B323 (2002).

[3] "Collisional-radiative study of lithium plasmas", S. D. Loch, C. J. Fontes, J. Colgan, M. S. Pindzola, C. P. Ballance, D. C. Griffin, M. G. O'Mullane, and H. P. Summers, Phys. Rev. E **69**, 066405 (2004).

[4] "Production and detection of cold antihydrogen atoms", M. Amoretti *et al.*, Nature (London) **419**, 456 (2002).

[5] "Background-Free Observation of Cold Antihydrogen with Field-Ionization Analysis of Its States", G. Gabrielse *et al.*, Phys. Rev. Lett. **89**, 213401 (2002).

[6] "Driven Production of Cold Antihydrogen and the First Measured Distribution of Antihydrogen States", G. Gabrielse *et al.*, Phys. Rev. Lett. **89**, 233401 (2002).

[7] "CPT and Lorentz Tests in Hydrogen and Antihydrogen", R. Bluhm, V. A. Kostelecký, Neil Russell, Phys. Rev. Lett. **82**, 2254 (1999).

[8] "Phase-Coherent Measurement of the Hydrogen 1S-2S Transition Frequency with an Optical Frequency Interval Divider Chain", T. Udem *et al.*, Phys. Rev. Lett. **79**, 2646 (1997).

[9] "Two-Photon Spectroscopy of Trapped Atomic Hydrogen", C. L. Cesar *et al.*, Phys. Rev. Lett. **77**, 255 (1996).

[10] "Antihydrogen production using trapped plasmas", G. Gabrielse *et al.*, Phys. Lett. A **129**, 38 (1988).

[11] "Three-body recombination for protons moving in a strong magnetic field", F. Robicheaux and J. D. Hanson, Phys. Rev. A **69**, 010701(R) (2004).

[12] "Three-body recombination for electrons in a strong magnetic field: Magnetic moment", F. Robicheaux, Phys. Rev. A **73**, 033401(R) (2006).

[13] "Ionization of atoms in parallel electric and magnetic fields: The role of classical phase space", W. Ihra, F. Mota-Furtado, and P. F. O'Mahony, Phys. Rev. A **58**, 3884 (1998).

[14] "Rydberg wave packets in parallel electric and magnetic fields", I. Moser, F. Mota-Furtado, and P. F. O'Mahony, Phys. Rev. A **55**, 3724 (1997).

[15] "Rydberg atoms in parallel magnetic and electric fields: II. Theoretical analysis of the Stark structure of the diamagnetic manifold of hydrogen", P. Cacciani, E. Luc-Koenig, J. Pinard, C. Thomas, and S. Liberman, J. Phys. B **21**, 3499 (1988).

[16] "Photodetachment cross section of H- in crossed electric and magnetic fields. I. Closed-orbit theory", A. D. Peters and J. B. Delos, Phys. Rev. A **47**, 3020 (1993).

[17] "Symmetry Breaking in Crossed Magnetic and Electric Fields", C. Neumann, R. Ubert, S. Freund, E. Flöthmann, B. Sheehy, K. Welge, M. Haggerty, and J. B. Delos, Phys. Rev. Lett. **78**, 4705 (1997).

[18] "Time-dependnet electron-impact scattering from He^+" using variable lattice spacings", M. C. Witthoeft, M. S. Pindzola and J. Colgan, Phys. Rev. A **67**, 032713 (2003).

[19] "The threshold law for single ionization of atoms or ions by electrons", G. H. Wannier, Phys. Rev. **90**, 817 (1953).

[20] "WKB approximation and threshold law for electron-atom ionization", R. Peterkop, J. Phys. B **4**, 513 (1971).

[21] "Two Electrons in a Coulomb Potential. Double-Continuum Wave Functions and Threshold Law for Electron-Atom Ionization", A. R. P. Rau, Phys. Rev. A **4**, 207 (1971).

[22] "Optical-potential approach to the electron-atom impact-ionization-threshold problem", A. Temkin and Y. Hahn, Phys. Rev. A **9**, 708 (1974).

[23] "Test of Wannier threshold laws: Double-photoionization cross section in helium", H. Kossmann, V. Schmidt, and T. Andersen, Phys. Rev. Lett. **60**, 1266 (1988).

[24] "Oscillations in the Double-Photoionization Cross Section of Li near Threshold ", R. Wehlitz, J. B. Bluett, S. B. Whitfield, Phys. Rev. Lett. **89**, 093002 (2002).

[25] "Unexpected Behavior of the Near-Threshold Double-Photoionization Cross Section of Beryllium", D. Lukić, J. B. Bluett, R. Wehlitz, Phys. Rev. Lett. **93**, 023003 (2004).

[26] "Two-electron escape near threshold: A Classical Process?", Jan-Michael Rost, Phys. Rev. Lett. **72**, 1998 (1994).

[27] "The Search for Oscillations in the near threshold photo-double ionization cross section of helium", U. Kleiman, T. Topçu, M. S. Pindzola, and F. Robicheaux, J. Phys. B **39**, L61 (2005).

[28] "Time-dependent quantal calculations for L=0 models of the electron-impact ionization of hydrogen near threshold", F. Robicheaux, M. S. Pindzola, and D. R. Plante, Phys. Rev. A **55**, 03573 (1997).

[29] "Classical Limit of the Hydrogen Atom", L. S. Brown, Am. J. Phys. **41**, 525 (1973).

[30] "Breakdown of Bohr's Correspondence Principle", B. Gao, Phys. Rev. Lett. **83**, 4225 (1999).

[31] "Bohrs correspondence principle: The cases for which it is exact", A. J. Makowski and K. J. Górska, Phys. Rev. A **66**, 062103 (2002).

[32] "Observation of spatially localized atomic electron wave packets", J. A. Yeazell and C. R. Stroud, Phys. Rev. Lett. **60**, 1494 (1988).

[33] "Calculated cross sections for the electron-impact ionization of Na(ns) and Na(nd) Rydberg atoms", H. Deutsch, K. B. MacAdam, K. Becker, H. Zhang, and T. D. Märk, J. Phys. B **39**, 343 (2006).

[34] "Differential ionization cross-section calculations for hydrogenic targets with $Z \leqslant 4$ using a propagating exterior complex scaling method", Philip L. Bartlett and Andris T. Stelbovics, Phys. Rev. A **69**, 040701(R) (2004).

[35] "Electron impact ionization of Rydberg atoms", D. Vrinceanu, Phys. Rev. A **72**, 022722 (2005).

[36] "Electron-impact ionization of hydrogen and lithiumlike systems", M. A. Uddin, A. K. F. Haque, A. K. Basak, K. R. Karim, and B. C. Saha, Phys. Rev. A **72**, 032715 (2005).

[37] "Electron-impact ionization of atomic hydrogen from the 1S and 2S states ", K. Bartschat and I. Bray, J. Phys. B **29**, L577 (1996).

[38] "Time-dependent close-coupling theory for e + H elastic and inelastic scattering", M. C. Witthoeft, S. D. Loch, and M. S. Pindzola, Phys. Rev. A **70**, 022711 (2004).

[39] "Electron-impact ionization of all ionization stages of beryllium", J. Colgan, S. D. Loch, M. S. Pindzola, C. P. Ballance, and D. C. Griffin, Phys. Rev. A **68**, 032712 (2003).

[40] "The validity of classical trajectory and perturbative quantal methods for electron-impact ionization from excited states in H-like ions", D. C. Griffin, C. P. Ballance, M. S. Pindzola, F. Robicheaux, S. D. Loch, J. A. Ludlow, M. C. Witthoeft, J. Colgan, C. J. Fontes, and D. R. Schultz, J. Phys. B **38**, L199 (2005).

[41] "Two-electron escape near threshold: A classical process?", J. M. Rost, Phys. Rev. Lett. **72**, 1998 (1994).

[42] "Inelastic semiclassical Coulomb scattering", Gerd van de Sand and Jan M. Rost, J. Phys. B **33**, 1423 (2000).

[43] " Electron-impact ionization of highly excited hydrogenlike ions in a collinear s-wave model ", T. Topçu, M. S. Pindzola, C. P. Ballance, D. C. Griffin, and F. Robicheaux, Phys. Rev. A **74**, 062708 (2006).

[44] "The Threshold Law for Single Ionization of Atoms or Ions by Electrons", G. H. Wannier, Phys. Rev. **90**, 817 (1953).

[45] "Differential cross sections in the ejected energy for an L=0 model of the electron-impact ionization of hydrogen", M. S. Pindzola and F. Robicheaux, Phys. Rev. A **55**, 4617 (1997).

[46] "Time-dependent electron-impact scattering from He^+ using variable lattice spacings", M. C. Witthoeft, M. S. Pindzola, and J. Colgan, Phys. Rev. A **67**, 032713 (2003).

[47] "Multiphoton ionization of hydrogen in parallel microwave and static fields: quantal and classical simulations", F. Robicheaux, E. Oks, A.L. Parker, and T. Uzer, J. Phys. B **35**, 4613 (2002).

[48] "Coulomb Born approximation for electron scattering from neutral atoms: application to electron impact ionization of helium in coplanar symmetric geometry", J. Botero and J. H. Macek, J. Phys. B **24**, L405 (1991).

[49] "T-matrix calculations for the electron-impact ionization of hydrogen in the Temkin-Poet model", M. S. Pindzola, D. Mitnik, and F. Robicheaux, Phys. Rev. A **62**, 062718 (2000).

[50] "Nonadiabatic Theory of Electron-Hydrogen Scattering", A. Temkin, Phys. Rev. **126**, 130 (1962).

[51] "The exact solution for a simplified model of electron scattering by hydrogen atoms", R. Poet, J. Phys. B **11**, 3081 (1978).

[52] "Unambiguous ionization amplitudes for electron-hydrogen scattering", P. L. Bartlett, I. Bray, S. Jones, A. T. Stelbovics, A. S. Kadyrov, K. Bartschat, G. L. Ver Steeg, M. P. Scott and P. G. Burke, Phys. Rev. A **68**, 020702(R) (2003).

[53] "Optical-potential approach to the electron-atom impact-ionization-threshold problem", A. Temkin and Y. Hahn, Phys. Rev. A **9**, 708 (1974).

[54] "Efficient solution of three-body quantum collision problems: Application to the Temkin-Poet model", S. Jones and A. T. Stelbovics, Phys. Rev. A **66**, 032717 (2002).

[55] "High-$|m|$ Rydberg states in strong magnetic fields", J. R. Guest and G. Raithel, Phys. Rev. A **68**, 052502 (2003).

[56] "Decay rates of high-$|m|$ Rydberg states in strong magnetic fields", J. R. Guest, J. -H. Choi, G. Raithel, Phys. Rev. A **68**, 022509 (2003).

[57] "Quantal and classical radiative cascade in Rydberg plasmas", M. R. Flannery and D. Vrinceanu, Phys. Rev. A **68**, 030502(R) (2003).

[58] "Radiative cascade of highly excited hydrogen atoms in strong magnetic fields", T. Topçu and F. Robicheaux, Phys. Rev. A **73**, 043405 (2006).

[59] When $2n^2 \ll r_f$, the $\epsilon_{n\ell} = -1/(2n^2)$ are the usual field free energy levels. In the opposite limit, the $\epsilon_{n\ell}$ rapidly increase to be greater than zero and have the form $C_\ell + \pi^2(n - D_\ell)^2/(2r_f^2)$ where C_ℓ and D_ℓ are constants that depend on ℓ and r_f.

[60] "The quadratic Zeeman effect in hydrogen Rydberg series: application of Sturmian functions", C. W. Clark and K. T. Taylor, J. Phys. B **15**, 1175 (1982).

[61] L. D. Landau and E. M. Lifshitz, *Quantum Mechanics* (3rd edition, Pergamon Press, Noida, 1998).

[62] R. D. Cowan, *The Theory of Atomic Structure and Spectra* (3rd edition,University of California Press, Los Angeles, 1981).

[63] J. D. Jackson, *Classical Electrodynamics* (3rd edition, John Wiley & Sons Inc., 1998).

[64] ”Charged anisotropic harmonic oscillator and the hydrogen atom in crossed fields ”, O. Dippel, P. Schmelcher, and L.S. Cederbaum, Phys. Rev. A **49**, 4415 (1994).

[65] R. Blümel and W. P. Reinhardt, *Chaos in Atomic Physics* (Cambridge University Press, Cambridge, 1997).

[66] ”Bound-state eigenfunctions of classically chaotic hamiltonians: Scars of periodic orbits”, E. J. Heller, Phys. Rev. Lett. **53**, 1515 (1984).

[67] ”Effect of closed classical orbits on quantum spectra: Ionization of atoms in a magnetic field. I. Physical picture and calculations”, M. L. Du and J. B. Delos, Phys. Rev. A **38**, 1896 (1988).

[68] ”Recurrence spectroscopy: Observation and interpretation of large-scale structure in the absorption spectra of atoms in magnetic fields ”, J. Main, G. Wiebusch, K. Welge, J. Shaw, and J. B. Delos, Phys. Rev. A **49**, 847 (1994).

[69] ”Absorption and recurrence spectra of hydrogen in crossed electric and magnetic fields”, S. Freund, R. Ubert, E. Flöthmann, K. Welge, D. M. Wang, and J. B. Delos, Phys. Rev. A **65**, 053408 (2002).

[70] ”Random-matrix physics: spectrum and strength fluctuations”, T. A. Brody, J. Flores, J. B. French, P. A. Mello, A. Pandey, and S. S. M. Wong, Rev. Mod. Phys. **53**, 385 (1981).

[71] ”Quantum Chaology, Not Quantum Chaos”, M. Berry, Physica Scripta **40**, 335 (1989).

[72] ”Classical irregular scattering and its quantum mechanical implications”, R. Blümel and U. Smilansky, Phys. Rev. Lett. **60**, 477 (1988).

[73] T. Ericson, Phys. Rev. Lett. **5**, 430 (1960).

[74] P. von Brentano, J. Ernst, O. Hausser, T. Mayer-Kuckuk, A. Richter, and W. von Witsch, Phys. Rev. Lett. **9**, 48 (1964).

[75] ”Chaotic ionization of highly excited hydrogen atoms: Comparison of classical and quantum theory with experiment”, R. V. Jensen, S. M. Susskind, and M. M. Sanders, Physics Rep. **201**, 1 (1991).

[76] ”Chaos-induced pulse trains in the ionization of hydrogen”, K. A. Mitchell, J. P. Handley, B. Tighe, A. Flower, and J. B. Delos, Phys. Rev. Lett. **92**, 073001 (2004).

[77] "Analysis of chaos-induced pulse trains in the ionization of hydrogen", K. A. Mitchell, J. P. Handley, B. Tighe, A. Flower, and J. B. Delos, Phys. Rev. A **70**, 043407 (2004).

[78] "Chaotic ionization of a highly excited hydrogen atom in parallel electric and magnetic fields", Türker Topçu and F. Robicheaux, J. Phys. B **40**, 1925 (2007).

[79] E. Merzbacher, *Quantum Mechanics* (3rd edition, John Wiley and Sons, New York, 1998).

[80] " Electron-impact ionization of highly excited hydrogenlike ions in a collinear s-wave model", T. Topçu, M. S. Pindzola, C. Ballance, D. C. Griffin, and F. Robicheaux, Phys. Rev. A **74**, 062708 (2006).

[81] W. H. Press, B. P. Flannery, S. A. Teukolsky, and W. T. Vetterling *Numerical Recepies in C* (Cambridge Univeristy Press, New York, 1988).

[82] H. A. Bethe and E. E. Salpeter, *Quantum Mechanics of One- and Two-Electron Systems* (Springer Verlag, Germany, 1957).

[83] "Calculated electron dynamics in an electric field", F. Robicheaux and J. Shaw, Phys. Rev. A **56**, 278 (1997).

[84] "Spectral Properties of Nonhydrogenic Atoms in Weak External Fields", T. Jonckheere, B. Gremaud, and D. Delande, Phys. Rev. Lett. **81**, 2442 (1998).

[85] "Regularity and Irregularity in Spectra of the Magnetized Hydrogen Atom", D. Wintgen and H. Friedrich, Phys. Rev. Lett. **57**, 571 (1986).

[86] "Correspondence of unstable periodic orbits and quasi-Landau modulations", D. Wintgen and H. Friedrich, Phys. Rev. A **36**, 131 (1987).

[87] "Quantum Poincaré Recurrences for a Hydrogen Atom in a Microwave Field", G. Benenti, G. Casati, G. Maspero, and D. L. Shepelyansky, Phys. Rev. Lett. **84**, 4088 (2000).

[88] T. F. Gallagher, *Rydberg Atoms* (Cambridge Monographs, New York, 1994).

[89] "Diamagnetism of the Hydrogen Atom in the Quasi-Landau Regime", A. Holle, G. Wiebusch, J. Main, B. Hager, H. Rottke, and K. H. Welge, Phys. Rev. Lett. **56**, 2594 (1986).

[90] "Diamagnetic structure of Rb in intense magnetic fields", N. P. Economou, R. R. Freeman, and P. F. Liao, Phys. Rev. A **18**, 2506 (1978).

[91] ”Landau condensation of the quasi-hydrogenic spectrum of caesium”, J. C. Gay, D. Delande, and F. Biraben, J. Phys. B **13**, L729 (1980).